
Atomistic Modelling of Aggregate Chlorophyll Systems

By

OLIVER J. H. FEIGHAN



School of Chemistry
UNIVERSITY OF BRISTOL

A dissertation submitted to the University of Bristol in accordance with the requirements of the degree of DOCTOR OF PHILOSOPHY in the Faculty of Science.

JANUARY, 2022

Word count: 0

ABSTRACT

Here goes the abstract

DEDICATION AND ACKNOWLEDGEMENTS

Here goes the dedication.

AUTHOR'S DECLARATION

I declare that the work in this dissertation was carried out in accordance with the requirements of the University's Regulations and Code of Practice for Research Degree Programmes and that it has not been submitted for any other academic award. Except where indicated by specific reference in the text, the work is the candidate's own work. Work done in collaboration with, or with the assistance of, others, is indicated as such. Any views expressed in the dissertation are those of the author.

SIGNED: DATE:

TABLE OF CONTENTS

	Page
List of Tables	xi
List of Figures	xiii
1 Introduction	1
1.1 Quantum Exploits in Light Harvesting Systems	1
1.1.1 Electronic Energy Transfer	1
1.1.2 Coherence	1
1.2 Light-Matter Response	1
1.3 Electronic Structure for Large Systems	1
1.4 The Aim	1
2 Mean-Field excited states	3
2.1 Theory	4
2.1.1 Δ -SCF	4
2.1.2 Eigenvalue Difference	5
2.1.3 Transition Density and Dipole Moments	6
2.1.4 Semi-empirical extensions	7
2.2 Benchmarking	9
2.2.1 Reference Data and test set	9
2.2.2 Small Systems	9
2.2.3 Non-orthogonality	13
2.2.4 LHII Chlorophyll	15
2.2.5 xTB methods	18
2.3 Conclusions	24
3 Chlorophyll specific methods	27
3.1 Theory	27
3.1.1 Full solutions TD-DFT equation	27
3.1.2 Approximations to Solutions	28

TABLE OF CONTENTS

3.1.3	Integrals approximations	29
3.1.4	Q_y Transition	31
3.1.5	Changes to xTB parameters	35
3.1.6	Transition and Excited State Density from the Ground State	35
3.2	Parameterization	37
3.2.1	Objective Function	37
3.2.2	Minimisation Algorithms	38
3.2.3	Reference Data	41
3.2.4	Results	46
3.3	Cross-validation	50
3.3.1	Vibrational Mode Coupling	50
3.3.2	Absorption Spectra	58
3.4	Conclusions	59
4	Beyond Monomer Chlorophyll	63
4.1	Theory	63
4.1.1	Exciton States	63
4.1.2	Embedding	65
4.2	Truncated Chlorophylls	65
4.2.1	Rotation	65
4.3	LHII Pairs	74
4.3.1	Assignment of States	74
4.3.2	Comparison	74
4.4	Conclusions	86
5	Atomistic Modelling of Light Harvesting Complexes	87
5.1	LHII	95
5.1.1	Spectral Density Method	95
5.1.2	Molecular Dynamics Method	95
5.2	Approximating Spectral Densities	95
5.2.1	Hessians	95
5.2.2	Huang Rhys Factors	95
5.2.3	Chlorophyll distances	95
5.3	Environmental Effects	95
5.3.1	Screening	95
5.3.2	Embedding	95
5.4	Sites, states and couplings	95
5.4.1	Sites	95
5.4.2	Exciton states	95

TABLE OF CONTENTS

5.4.3	Coupling	95
5.5	Excitation Energies	95
6	Discussion	97
6.1	Transition Property Approximations	97
6.2	Further Investigations into LHII	97
6.3	Coherence	97
A	Appendix A	99
A.1	Electronic Structure Codes	99
A.2	Computational Hardware	99
	Bibliography	101

LIST OF TABLES

TABLE	Page
2.1 Mean and standard deviations of the errors, in eV, against SCS-CC2 reference data. The <code>xtb4stda</code> entry represents the eigenvalue difference method that uses the eigenvalues output from this program.	23
3.1 ref data vals	44
3.2 optimized parameters from SLSQP procedure.	46

LIST OF FIGURES

FIGURE	Page
2.1 Transition energies ΔE from TD-DFT (black) and Δ -SCF (red) plotted against EOM-CCSD energies, with the line $y = x$ (dashed) for reference. The ethene dimer outlier has been circled.	11
2.2 Transition dipole magnitudes from TD-DFT (black) and Δ -SCF (red) plotted against EOM-CCSD transition dipole magnitudes, with the line $y = x$ (dashed) for reference.	12
2.3 The absolute value of the error in transition dipole magnitude between Δ -SCF and EOM-CCSD, plotted against the Δ -SCF overlap of the ground and excited state. All systems were translated by 100 Å in all cartesian axes. Transition dipole magnitudes calculated without any correction are shown in red, whilst those with the symmetric orthogonalisation correction are shown in black.	14
2.4 Transition energies from Δ -SCF for 26 chlorophyll geometries from the LHII protein of purple bacteria, plotted against energies from TD-DFT. The line of best fit ($R^2 = 0.87$) is shown as the dashed line. Both methods used a PBE0/Def2-SVP level of theory.	16
2.5 Transition dipole magnitudes from Δ -SCF for the same 26 chlorophyll geometries as 2.2.4, plotted against dipole magnitudes from TD-DFT. The line of best fit ($R^2 = 0.57$) is shown as the dashed line. Both methods used a PBE0/Def2-SVP level of theory.	17
2.6 A breakdown of the symmetry orbitals in STO-3G methane into the subspaces present in the T_d point group.	20
2.7 The distributions of errors compared to SCS-CC2 transition energies for the methods included in the Δ -xTB benchmarking.	22
3.1 Bacterial Chlorophyll a (BChla) with a model Q_y transition dipole.	32
3.2 The HOMO orbital of bacterial chlorophyll a from PBE0/Def2-SVP DFT.	33
3.3 The LUMO orbital of bacterial chlorophyll a from PBE0/Def2-SVP DFT.	34
3.4 Positions of the Nelder-Mead simplex vertices for the HimmelBlau function.	42
3.5 Positions of iterative solution vector \mathbf{x} from SLSQP for the HimmelBlau function.	43
3.6 caption	47
3.7 caption	48

LIST OF FIGURES

3.8	Normal modes of the nitrogen-magnesium centre of chlorophyll that have D_{4h} - D_{2h} (left) and D_{4h} - C_s (right) symmetry breaking components.	50
3.9	Change in the N_A - N_C displacements along the set of GFN1-xTB normal modes for a chlorophyll molecule truncated at the phytol tail.	52
3.10	Change in the N_A - Mg - N_C angle along the set of GFN1-xTB normal modes for a chlorophyll molecule truncated at the phytol tail. The small smaller variance than in figure 3.3.1 led to this metric to not be used in normal mode choices.	53
3.11	Transition energies and dipole magnitudes for the Q_y transition for geometries of truncated chlorophyll along normal modes, calculated with different response theories.	58
3.12	Chlorophyll in diethyl ether.	60
4.1	caption	68
4.2	caption	69
4.3	caption	70

INTRODUCTION

Naturally occurring light harvesting systems present an interesting scientific challenge. With near perfect efficiency, the energy from a photon will be taken and transferred to a reaction centre, leading to charge transfer processes that culminate in powering biological systems. Making models that can predict and explain these effects are key to making similarly efficient photovoltaic systems.

1.1 Quantum Exploits in Light Harvesting Systems

Begins a section.

1.1.1 Electronic Energy Transfer

Begins a subsection.

1.1.2 Coherence

1.2 Light-Matter Response

1.3 Electronic Structure for Large Systems

1.4 The Aim

MEAN-FIELD EXCITED STATES

Previous Published Work

Some of the work presented in this chapter forms part of a paper published with Dr Susannah Bourne-Worster, in March 2021[30]. The account given in this chapter includes research that was also reported in this publication, namely the parts of section 2.2 from 2.2.1 up to but excluding 2.2.5.

This chapter investigates the accuracy of Δ -SCF methods with both an ab initio DFT level of theory as well as with semi-empirical, tight-binding approximations. The reduced cost and moderate accuracy of these methods make them an ideal substitute for full TD-DFT or high-level methods when investigating large systems like chlorophyll. Transition properties were calculated for a range of molecules, as well as for a small set of chlorophyll geometries, using variety of different basis sets, density functionals, response methods and electronic structure methods. Most of the work was compared to either high-standard EOM-CCSD or SCS-CC2 reference, from which conclusions were made on the accuracy of each method. The non-orthogonality issue of the ground and excited states was also investigated for the mean-field Δ -SCF method. Assigning the symmetries of transitions was also investigated to improve the workflow of comparing Δ -SCF and TD-DFT results. It was found that while the DFT methods give reasonable results, the semi-empirical Δ -SCF methods are not as accurate.

Δ -SCF is a well-known method for calculating transition energies, as well as ionisation potentials, electron affinities and other properties. Although slightly less accurate than other high-level response theories, it is much more efficient, requiring only two SCF solutions for the two states of a transition. In the context of calculating large volumes of transition properties for the chlorophyll sites of LHII, this efficiency makes it a good candidate for investigation.

Previous work in the literature has discussed the benefits of the Δ -SCF method for large scale

systems. Notably

2.1 Theory

2.1.1 Δ -SCF

Δ -SCF predicts the transition energy ΔE of a system as the difference of the single point energy E_n of two states:

$$(2.1) \quad \Delta E = E_2 - E_1$$

It is usually assumed that the excited state solution will be in a similar location to the ground state in the MO coefficient space. The ground state MO coefficients are usually used for an initial guess for the excited state for this reason. In its simplest form, the Δ -SCF method calculates the ground state with normal DFT or other mean-field methods, and then calculates the excited state by rerunning the same method with the excited state occupation numbers. The two sets of MO coefficients give a full description of both the ground as excited state.

The issue with finding the excited state solution is that the variation principle and SCF iterative procedure will try to find the global minimum, which is the ground state. The excited state is a local minimum, and so often is less reliable to find as a solution, especially from the standard SAD initial guess. For this reason it is often found that converging to the Δ -SCF excited state will fail. Even when using the ground state as an initial guess with excited state occupations, normal SCF procedure may still collapse back to the ground state. Usually it is necessary to include additional changes to the SCF procedure, such as Fock damping, alternative DIIS methods and sometimes intermediate initial guess steps.

Initially, the excited state was calculated by relaxing the orbitals which contain the excited electron and hole in the ground state space, so that the excited state and ground state are orthogonal [17]. However, it was argued that this procedure would exacerbate the likelihood of collapsing to the ground state, and that the excited state was not a proper SCF solution [9]. Alternatively, an SCF like method was proposed, where instead of populating orbitals according to the Aufbau principle, orbitals which most resemble the previous iteration's orbitals should be occupied. This is known as the maximum overlap method (MOM). In the maximum overlap method, each iteration in an SCF procedure produces new molecular orbital coefficients by solving the Roothaan-Hall equations [26], generally given as an eigenvalue problem:

$$(2.2) \quad \mathbf{FC}^n = \mathbf{SC}^n \epsilon$$

where \mathbf{C}^n are the n^{th} orbital coefficient solutions, \mathbf{S} is the overlap of orbitals, and ϵ are the orbital energies. The Fock matrix \mathbf{F} is calculated from the previous set of orbital coefficients,

$$(2.3) \quad \mathbf{F} = f(\mathbf{C}^{n-1})$$

. The amount of similarity of orbitals can be estimated from their overlap,

$$(2.4) \quad \mathbf{O} = (\mathbf{C}^{\text{old}})^{\dagger} \mathbf{S} \mathbf{C}^{\text{new}}$$

and for a single orbital can be evaluated as a projection,

$$(2.5) \quad p_j = \sum_i^n O_{ij} = \sum_v^N \left[\sum_{\mu}^N \left(\sum_i^n C_{i\mu}^{\text{old}} \right) S_{\mu v} \right] C_{vj}^{\text{new}}$$

where μ, v are orbital indices. the set of orbitals with the highest projection p_j are then populated with electrons. This method can be used for any excited state, with the caveat that the orbital solution will most likely be in the same region as the ground state solution. For a small number of low lying states, this is generally true, and so Δ -SCF can be used to calculate a small spectrum of excited states [9].

Δ -SCF has been shown to be cheap alternative to TD-DFT and other higher level methods [4, 8, 21], without considerable losses of accuracy in certain cases, especially for HOMO-LUMO transitions [20]. Additionally, as the excited state is given as solutions to SCF equations, the gradient of this solution can be given by normal mean-field theory. These gradients would be much cheaper than TD-DFT or coupled cluster methods, which is advantageous for simulating dynamics [8].

2.1.2 Eigenvalue Difference

Another approximation to full response theory is the eigenvalue difference method. Here there is assumed to be no response of the orbital energies and shapes when interacting with light. This would be recovered from the complete Cassida equation if the coupling elements in the \mathbf{A} and \mathbf{B} matrices were set to zero. Within this approximation, the transition energy is just the difference between the ground state energy of the orbital an electron has been excited to (ϵ_e) and the orbital has been excited from (ϵ_g),

$$(2.6) \quad \Delta E = \epsilon_e - \epsilon_g$$

. Additionally, transition properties can be calculated by constructing transition density matrices from the ground state orbitals such that needing only a single SCF optimization is required. Generally, eigenvalue difference methods are not seen as accurate response methods, but can offer a quick and easy initial value [10].

2.1.3 Transition Density and Dipole Moments

Δ -SCF transition properties, such as the transition dipole moment, can be calculated from the SCF solutions for the ground and excited states. The reduced one-particle transition density matrix \mathbf{D}^{21} can be written as

$$(2.7) \quad \mathbf{D}^{21} = |\Psi_1\rangle\langle\Psi_2|$$

where $|\Psi_n\rangle$ is the Slater determinant of state n , constructed from the set of spin orbitals $\{\phi_j^{(n)}\}$. Expressed in terms of the molecular orbitals coefficients $\mathbf{C}^{(n)}$, the transition density matrix is

$$(2.8) \quad \mathbf{D}^{21} = \mathbf{C}^{(2)} \text{adj}(\mathbf{S}^{21}) \mathbf{C}^{(1)\dagger}$$

where \mathbf{S}^{21} is an overlap matrix with elements

$$(2.9) \quad S_{jk}^{21} = \langle\phi_j^2|\phi_k^1\rangle$$

. The dependence on the adjunct of the overlap can be understood using Löwdin's normal rules for non-orthogonal determinants [22]. In the same way, the transition dipole moment is given by

$$(2.10) \quad \langle\Psi_2|\hat{\mu}|\Psi_1\rangle = \sum_{jk} \mu_{jk}^{21} \text{adj}(\mathbf{S}^{21})_{jk}$$

where $\hat{\mu}$ is the one-electron transition dipole operator, and μ_{jk} is the element of this operator corresponding to orbital indices j, k . The determinant of \mathbf{S}^{21} can be defined as the inner product of the two states involved in the transition

$$(2.11) \quad |\mathbf{S}^{21}| = \langle\Psi_2|\Psi_1\rangle$$

The general definition of the transition dipole

$$(2.12) \quad \mu^{1\rightarrow 2} = \langle\Psi_2|\hat{\mu}|\Psi_1\rangle$$

can be expressed with this transition density matrix as:

$$(2.13) \quad \begin{aligned} \langle\Psi_2|\hat{\mu}|\Psi_1\rangle &= \text{tr}(\hat{\mu}|\Psi_1\rangle\langle\Psi_2|) \\ &= \text{tr}(\hat{\mu}\mathbf{D}^{21}) \end{aligned}$$

2.1.4 Semi-empirical extensions

A main investigation of this chapter is whether the range of DFT methods that could be used for Δ -SCF and eigenvalue difference methods could be extended by using tight-binding methods to predict transition properties. This mainly focused on the recently published GFN-xTB method, parameterized by the Grimme group [14]. This method has been parameterized for geometries, frequencies and non-covalent interactions, and uses an extended version of Hückel theory. The name GFN-xTB is an acronym for "Geometries, Frequencies, Non-Covalent - eXtended Tight Binding". This method was chosen as a similar method has already been published that calculates transition properties, the precursor to the GFN-xTB methods. This is the sTDA-xTB method. Additionally it was convenient the GFN-xTB method was already implemented in the QCORE package. This significantly reduced the amount of effort required for this project, with other users and developers who could help with implementation of this new method.

2.1.4.1 sTDA-xTB

sTDA-xTB ("simplified Tann-Danoff Approximation - eXtended Tight Binding") is another method in the family of xTB methods developed by the Grimme group, and is parameterised for transition properties [13]. The accuracy in calculating transition energies with this method is very good, with the error compared to high-level method, such as SCS-CC2, being around 0.3 - 0.5 eV.

Similar to other xTB methods, the sTDA-xTB method is a tight-binding method that uses empirically fitted parameters and a minimal basis set. It was trained on a test set of highly accurate coupled cluster and density functional theory excitation energies, as well as atomic partial charges for inter-electronic interactions.

Unlike other xTB methods, coefficients in the basis set for sTDA-xTB are dependent on the D3 coordination number. This makes basis functions far more flexible, which would usually be achieved with fixed basis functions by using diffuse or other additional orbitals in the basis set. Additionally, it uses two sets of parameterized basis sets - a smaller valence basis set (VBS) and an extended basis set (XBS). Whilst this reduces the cost of having larger basis sets, it makes calculating the gradient of transition properties much more difficult. This motivates the work on designing an alternative method with more tractable gradients, instead of using this already established method.

The two basis sets are used to construct formally similar Fock matrix elements, although in practice they use different global parameters. The core Hamiltonian is similar to other DFTB methods that use a self-consistent charge (SCC) method, as opposed to an SCF method, to obtain molecular orbital coefficients. It is given by,

$$(2.14) \quad \langle \psi_\mu | H^{\text{EHT, sTDA-xTB}} | \psi_\mu \rangle = \frac{1}{2} \left(k_\mu^l k_\nu^{l'} \right) \frac{1}{2} \left(h_\mu^l h_\nu^{l'} \right) S_{\mu\nu} - k_T \langle \psi_\mu | \hat{T} | \psi_\nu \rangle$$

where μ, ν, l, l' are orbital and shell indices, k_μ^l are shell-wise Hückel parameters, h are effective atomic-orbital energy levels, $S_{\mu\nu}$ is the overlap of orbitals μ and ν , k_T is a global constant and \hat{T} is the kinetic energy operator. The charges used in the inter-electronic repulsion function are given by charge model 5 (CM5) [23] charges for the XBS Fock matrix. These are calculated using Mulliken charges obtained from diagonalising the Fock matrix with the VBS. The charges for the initial VBS Fock matrix are based on Gasteiger charges [7], modified by the parameterised electronegativities of atoms in the system.

The whole process for determining molecular orbitals can be summarized as:

1. Calculate modified Gasteiger charges for the first initial guess
2. Diagonalise Fock matrix in the VBS to get the first set of Mulliken charges
3. Compute CM5 charges
4. Diagonalise Fock matrix in the VBS again for final set of Mulliken charges.
5. Recalculate CM5 charges with this final set, and diagonalize the Fock matrix in the XBS.

The molecular orbital coefficients from this are then fed to the response theory.

The response theory for this method is based on previous work in the Grimme group on the simplified Tamm-Danoff Approximation [11]. There are several approximations made between full linear response theory and the sTDA method. First is the Tamm-Danoff approximation, where the **B** matrix is ignored. The second approximation is to use monopole approximations with Mataga-Nishimoto-Ohno-Klopman (MNOK) operators instead of explicit 2 electron integral as well as neglecting the density functional term.

Transition charges are used to calculate these MNOK integrals. The charge q_{nm}^A centred on atom A associated with the transition from $n \rightarrow m$, are computed using a Löwdin population analysis:

$$(2.15) \quad q_{nm}^A = \sum_{\mu \in A} C'_{\mu n} C'_{\mu m}$$

where the transformed coefficients $C'_{\mu n}$ are given by orthogonalising the original MO coefficients **C**:

$$(2.16) \quad \mathbf{C}' = \mathbf{S}^{\frac{1}{2}} \mathbf{C}$$

and μ is an index that runs over the atomic orbitals (AO). The MO coefficients are the solution of diagonalising the Fock matrix, similar to equation 2.2.

Approximations to full 2 electron integrals are given by charge-charge interaction damped by the MNOK[24][25][19] functions. For exchange and coloumb type integrals, difference exponents

are used, along with an additional free parameter to recover the amount of Fock exchange mixing in the original matrix element equation. These will be discussed in more detail in the next chapter, as they are a crucial part of designing a new response method for chlorophyll systems.

Third is the truncation of single particle excited space that is used to construct the \mathbf{A} matrix. This reduces the number of elements that need to be calculated, and so reduces the time taken for diagonalisation, whilst also capturing a broad enough spectrum of excitation energies. The sTDA-xTB has many of the same goals as this project, except in one respect, which is the gradient theory. As the sTDA-xTB method still requires constructing and diagonalizing the \mathbf{A} matrix, albeit with a tight-binding method for molecular orbital coefficients, the gradient of the transition properties would still be difficult to calculate.

2.2 Benchmarking

Full scale chlorophyll molecules are too large to be able to calculate a high-level benchmark. A test set of small molecules, which would cover the same range of elements as found in organic chromophores and biological molecules, was then chosen as it would be able to benchmark both the Δ -SCF methods as well as TD-DFT. With an accurate idea of how reliable TD-DFT is, it would be possible to then compare Δ -SCF to TD-DFT for chlorophyll systems, as both methods have usable scaling to calculate transition properties for larger systems,

The test set chosen was previously used by the Grimme group to parameterise and test the sTDA-xTB method [14], and was constructed with the same goals as this work.

2.2.1 Reference Data and test set

The test set consisted of 109 small molecules. Each system was closed-shell, contained 12 atoms or less, and contained on H, C, N, O and F atoms. The size and specificity of this test set was chosen to minimise any other factors that could cause errors in analysing the results, whilst still covering all relevant elements and chemical environments for organic and biological chromophores.

Reference data was calculated as the three lowest energy singlet excited states, using EOM-CCSD with an aug-cc-pVTZ basis set. These results were generated using the Gaussian 16 program [6].

2.2.2 Small Systems

Transition properties for this test set were calculated using TD-DFT and Δ -SCF , both using a CAM-B3LYP functional and aug-cc-pVTZ basis set. The transitions were assigned to the EOM-CCSD results by comparing transition dipoles, energies and the character of the MOs involved in the transitions. Where the symmetries could be assigned, these were also used, but this was not the case for all systems as many were unsuccessful in labelling symmetry or defaulted to a

non-Abelain group. Symmetry labelling was also only available for TD-DFT calculations, as these were performed with Gaussian 16. Δ -SCF calculations were done with the QCORE program.

The Δ -SCF singlet transition is not a correct representation of a true singlet excitation, which is a superposition of both spin-conserving $\alpha \rightarrow a, \alpha$ and spin-flipping $\alpha \rightarrow a, \beta$ excitations. The spin-purification formula:

$$(2.17) \quad \Delta E_S = 2\Delta E^{i,\alpha \rightarrow a,\alpha} - \Delta E^{i,\alpha \rightarrow a,\beta}$$

was used to correct for the true singlet excitation energy ΔE_S [32].

The results of comparing transition energies and transition dipole magnitudes are shown in figures 2.1 and 2.2.

Overall, the excitation energies calculated with Δ -SCF are as accurate at predicting EOM-CCSD energies as TD-DFT. The mean error is 0.35 eV, with a standard deviation of 0.25 eV. This is a marginal improvement on the TD-DFT results, which has a mean and standard deviation of 0.41 eV and 0.27 eV respectively. Transition dipoles were similarly accurate to the reference data, although Δ -SCF performs slightly worse in this respect. The mean and standard deviation in the absolute value of transition dipole moment, $|\mu|$, was 0.07 a.u. and 0.08 a.u. respectively. For TD-DFT, the mean and standard deviation were 0.03 a.u. and 0.06 a.u. (the atomic unit here being equal to ea_0). The outlier circled in figure 2.1 is an ethene dimer system, and shows the inability of Δ -SCF to capture a mixed excited state. The two LUMO orbitals in this dimer system are in-phase and out-of-phase combinations of the π -antibonding orbitals, which are very close in energy. The HOMO orbitals are the same on both ethene molecules, being the π -bonding orbitals, which are degenerate in energy. The first excited state is predicted by TD-DFT and EOM-CCSD to be a mix of these two close HOMO-LUMO transitions. However Δ -SCF cannot include this mixed behaviour. Δ -SCF predicts two transitions of 7 eV and 10 eV, whilst TD-DFT and EOM-CCSD predict 7.5 eV. The outlier in figure 2.2 is due to Δ -SCF finding a different but still valid description of the transition dipole. This point corresponds to a stretched benzene system, where the HOMO-1, HOMO, LUMO and LUMO+1 orbitals are all degenerate. The Δ -SCF transition dipole magnitude agrees with the value of an equally mixed HOMO - LUMO+1 and HOMO-1 - LUMO transition, which given the degeneracy is an equally valid description of the transition.

In summary, Δ -SCF can be seen to accurately predict transition properties to a EOM-CCSD level of accuracy with as much success as TD-DFT, except in cases of mixed transitions. It might then be expected a tight-binding method, with good electronic structure treatment, could also be accurate whilst drastically reducing the cost of calculation.

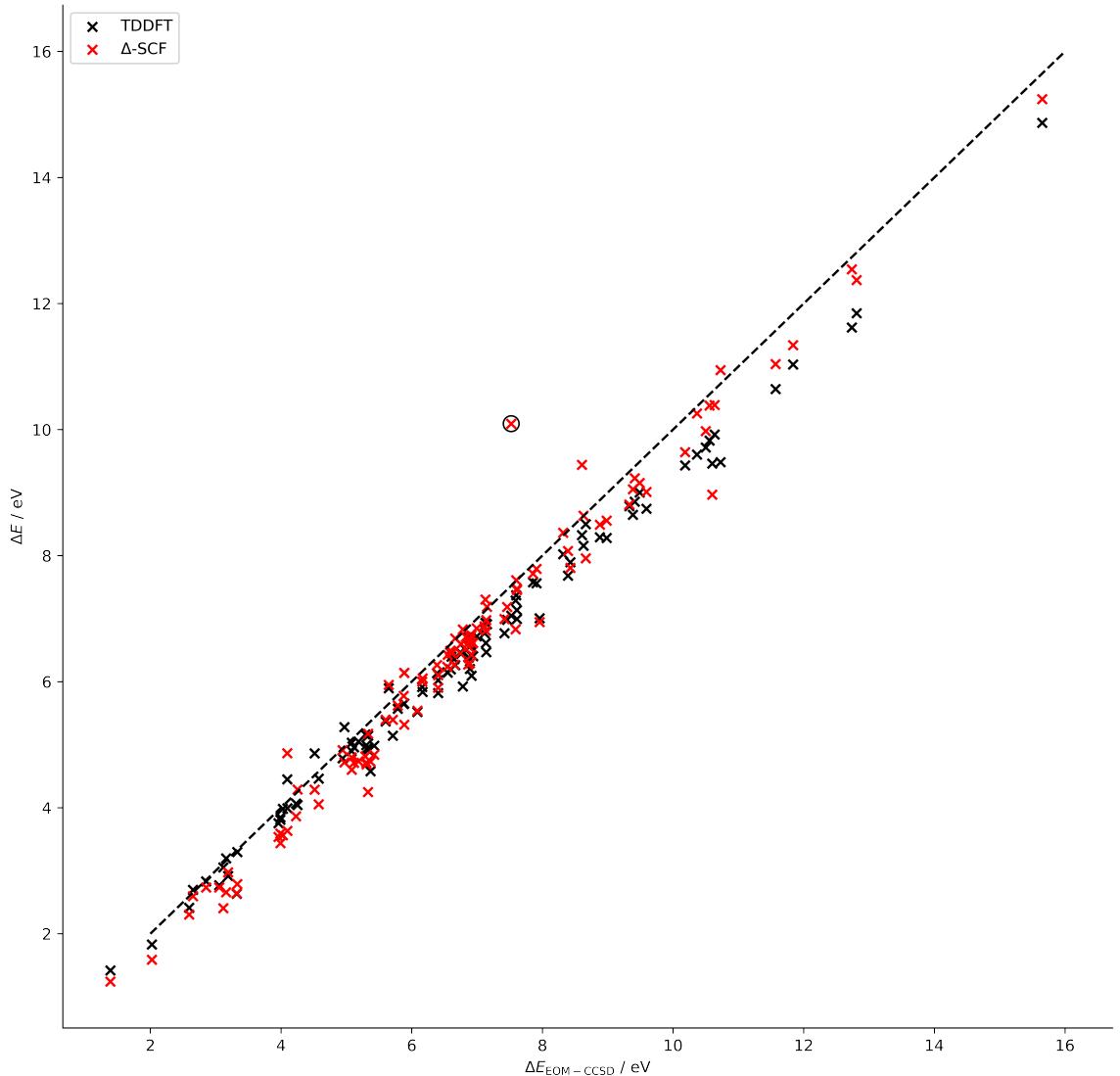


Figure 2.1: Transition energies ΔE from TD-DFT (black) and Δ -SCF (red) plotted against EOM-CCSD energies, with the line $y = x$ (dashed) for reference. The ethene dimer outlier has been circled.

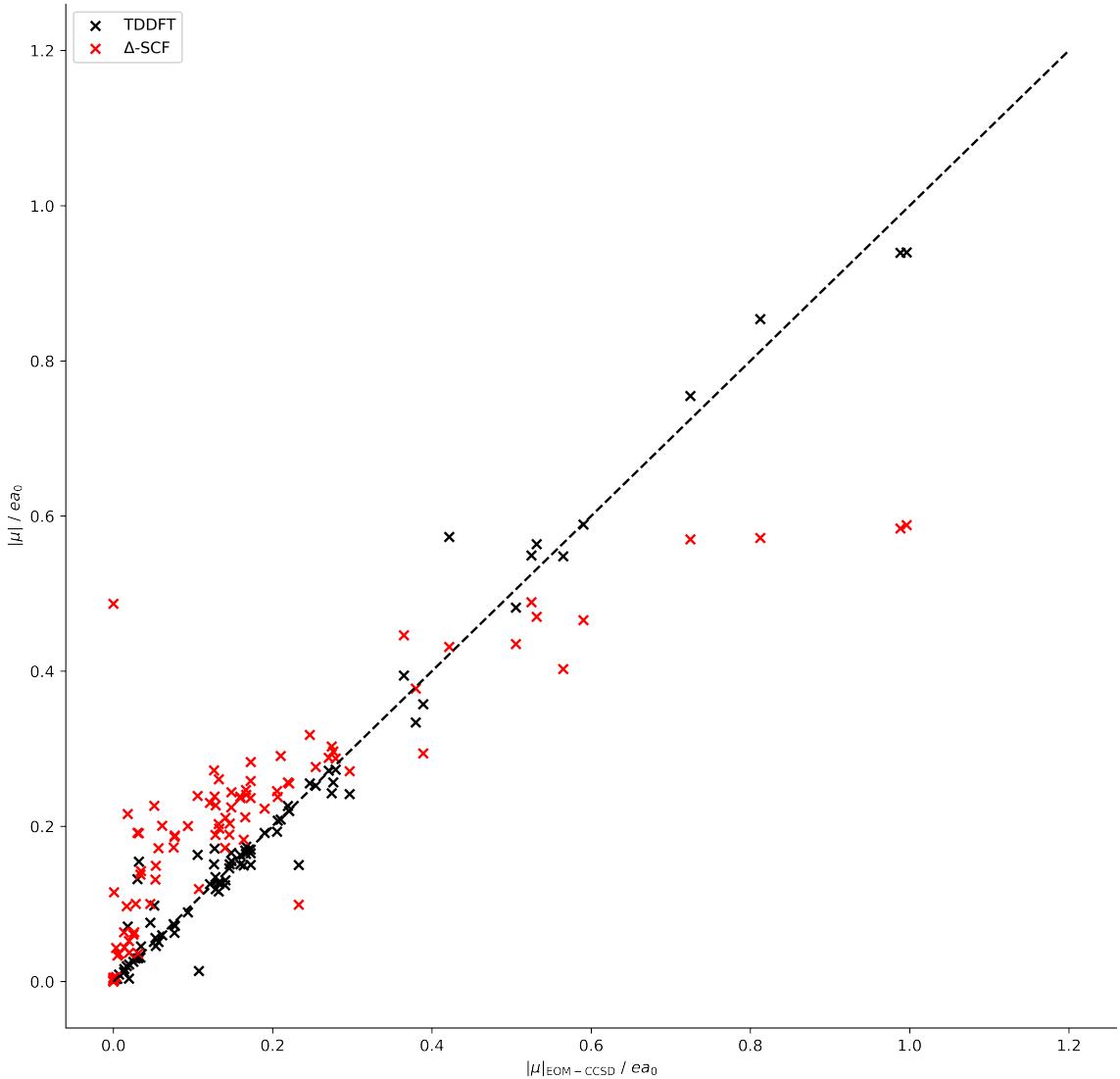


Figure 2.2: Transition dipole magnitudes from TD-DFT (black) and Δ -SCF (red) plotted against EOM-CCSD transition dipole magnitudes, with the line $y = x$ (dashed) for reference.

2.2.3 Non-orthogonality

There is another caveat with Δ -SCF. The ground and excited states, solutions to two separate SCF cycles, will not be truly orthogonal. The Slater determinants $|\Psi_n\rangle$, are constructed from a set of mutually orthogonal orbitals $\{|\phi_j^{(n)}\rangle\}$, such that orbitals will be orthogonal within the same state. However there is no orthogonality constraint on sets of orbitals derived from independent SCF cycles so it is possible for the overall states Ψ_1 and Ψ_2 to overlap such that the inner product,

$$(2.18) \quad S_{jk}^{21} = \langle \phi_j^{(2)} | \phi_k^{(1)} \rangle$$

will be non-zero. Similarly, there will be a non-zero transition charge,

$$(2.19) \quad q^{21} = \langle \Psi^2 | \Psi^2 \rangle$$

, which breaks the origin-independence property of the transition dipole moment. In this way, any transition dipoles that do not have their centre at the origin will have a systematic error based on this overlap and the distance from the origin. For vertical transitions, this transition charge should be zero, and so all transition dipole moments calculated with non-orthogonal Δ -SCF would always have this error.

In order to fix this issue, the standard transformation to symmetrically orthogonalise the two states was applied, which also would preserve as much character of the original states as possible. The transformation is given by

$$(2.20) \quad |\Psi_{\tilde{\nu}}\rangle = \sum_{\nu} |\Psi_{\nu}\rangle \left[\mathbf{S}^{-\frac{1}{2}} \right]_{\nu\tilde{\nu}}$$

where \mathbf{S} here is a block matrix

$$(2.21) \quad \mathbf{S} = \begin{pmatrix} 1 & S \\ S & 1 \end{pmatrix}$$

with S being the overlap value of the two states $\langle \Psi_2 | \Psi_1 \rangle$.

It was found that using this method for correcting the non-zero overlap of states, the origin-independence of the transition dipole moment was recovered (see figure 2.2.3). The transition dipole for each molecule in the test set systems was calculated for molecules translated by 100 Å in each of the x , y and z axes. This would induce an error for the non-orthogonalised states, which has been corrected for in the calculations with the symmetric orthogonalisation. It should be noted that whilst this effect is dependent on how large the overlap may be, and it could be argued that with a small overlap this effect may not be large, having any large translation of the molecule (on the order of hundreds of angstroms) can lead to nonphysical transition dipole

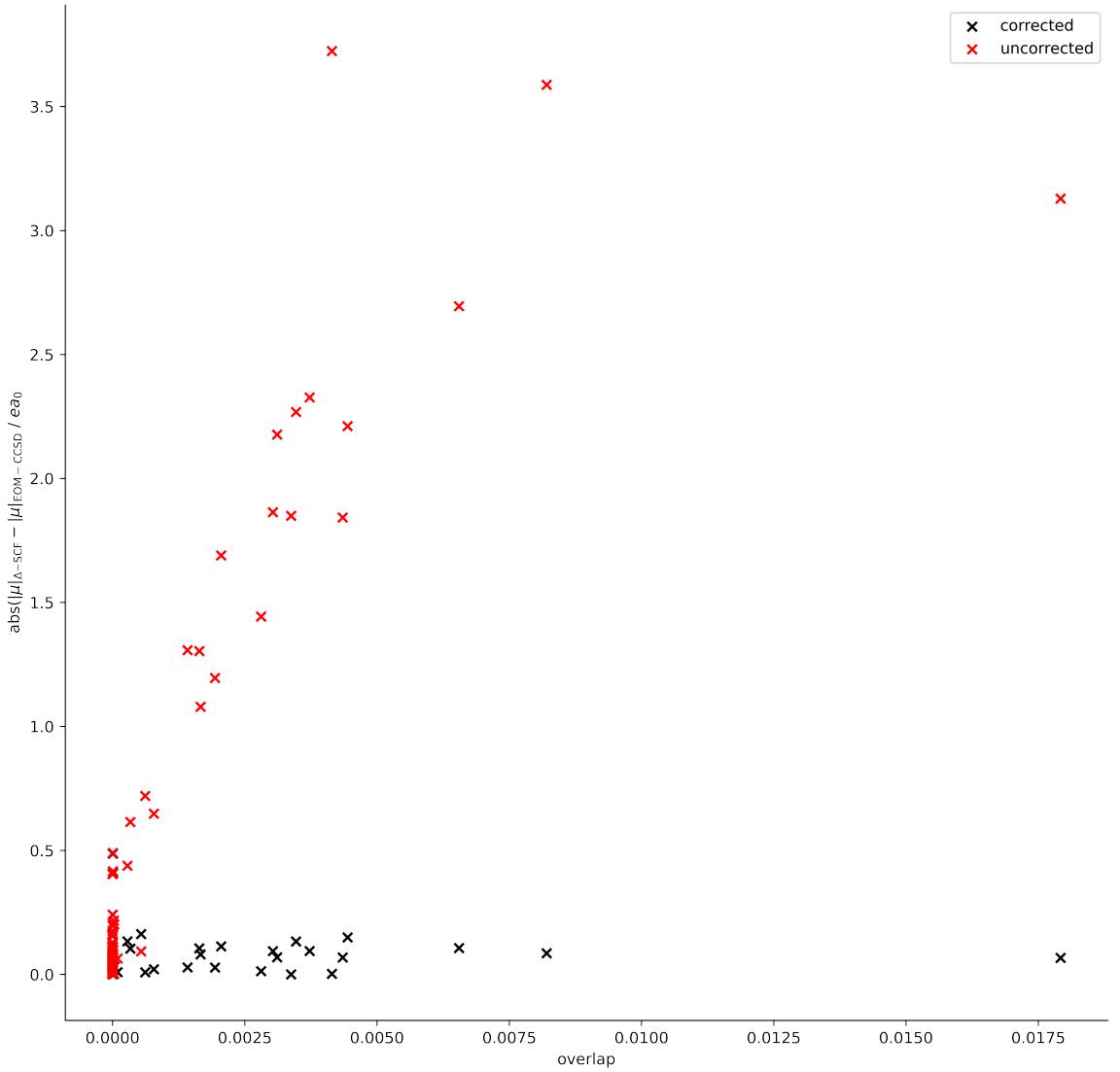


Figure 2.3: The absolute value of the error in transition dipole magnitude between Δ -SCF and EOM-CCSD, plotted against the Δ -SCF overlap of the ground and excited state. All systems were translated by 100 Å in all cartesian axes. Transition dipole magnitudes calculated without any correction are shown in red, whilst those with the symmetric orthogonalisation correction are shown in black.

magnitudes. In a large protein system, where chromophores can easily be 100 Å from the origin of the overall system, this would obviously present a much larger problem than for a vacuum-phase small molecule.

2.2.4 LHII Chlorophyll

Having demonstrated that TD-DFT is a good proxy for high-level methods, it is possible then to benchmark Δ -SCF for use in simulating a whole LHII system by looking at a set of chlorophyll geometries. This also has the additional benefit of testing Δ -SCF against more complex cases.

The PBE0 functional with Def2-SVP basis set [2, 27] was used to calculate both TD-DFT and Δ -SCF properties. This has been used previously for BChla structures, and has been shown to be a good balance between accuracy and cost [29].

The high degree of correlation between Δ -SCF and the TD-DFT results demonstrates it can detect changes in transition energies due to variation in geometries with an accuracy greater than the noise of random error from Δ -SCF. However the error in transition dipole magnitudes is larger than that of the small test set. This error is about 0.42 a.u. larger, but without EOM-CCSD or another high-level method, it's unclear whether this error might be from TD-DFT or Δ -SCF. Additionally, there is a clear correlation between the transition dipole magnitudes from TD-DFT and Δ -SCF, and so whilst quantitative statements cannot be made, qualitative assessments could be made from Δ -SCF data. For example, whilst the exact value of a transition dipole moment at a given geometry along a normal mode may not be accurate, the change in transition dipole moment from several geometries along the normal mode would be similar in variation to TD-DFT calculated properties.

An important point to take note of is that the excited state was not possible to calculate for all 27 chlorophyll geometries. One geometry repeatedly collapsed back down to the ground state. Methods such as increasing the amount of mixing of current and previous Fock matrices in Fock damping, using intermediate initial guesses like half-electron promotions, and alternative DIIS procedures, had little effect on improving this. Other methods could have been tried, such as the initial maximum overlap method (iMOM), where the projection in the MOM procedure is based on one static set of orbitals, such as the initial ground state, rather than the previous SCF cycle, but implementing and testing these is outside the scope of this work.

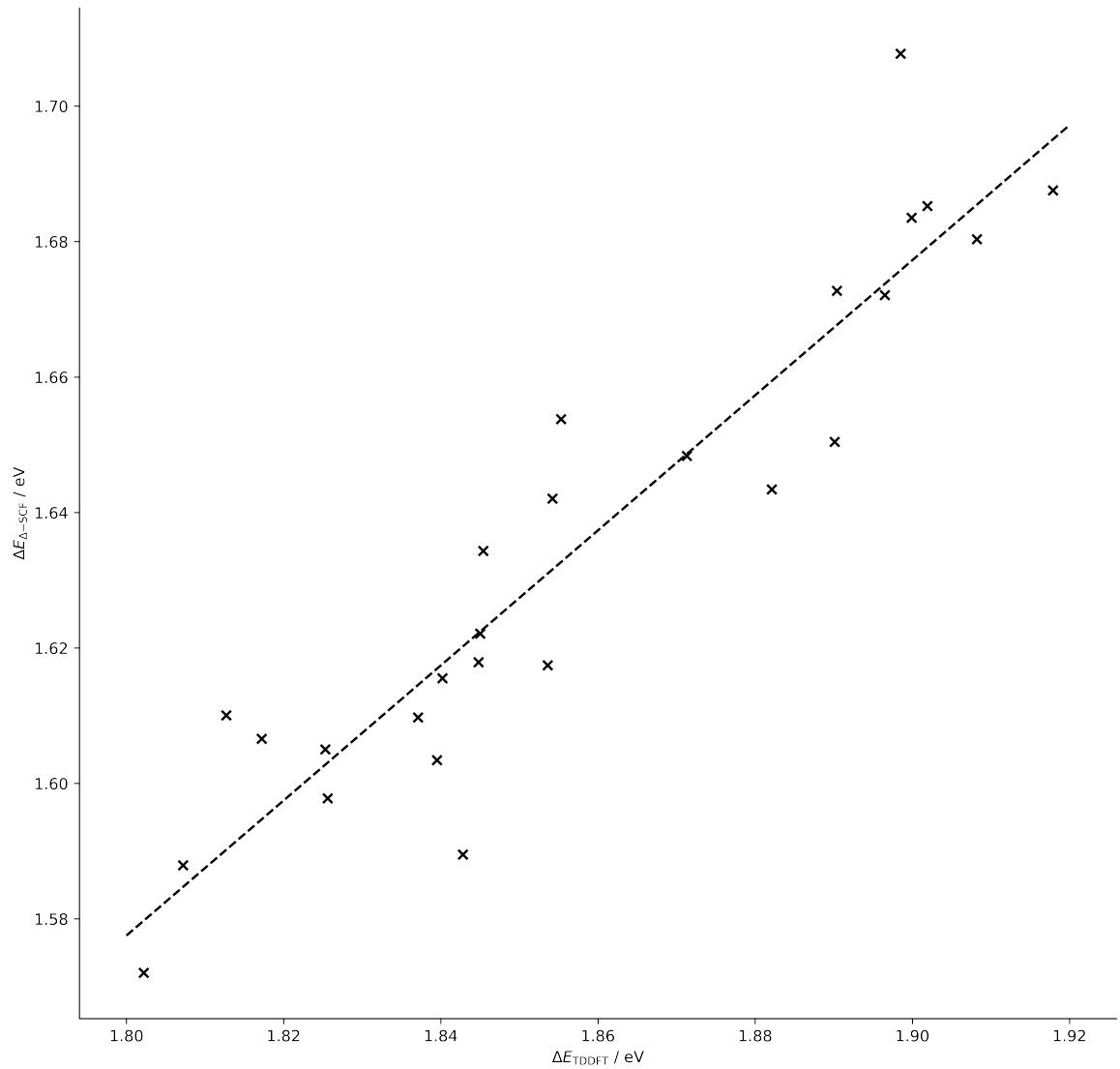


Figure 2.4: Transition energies from Δ -SCF for 26 chlorophyll geometries from the LHII protein of purple bacteria, plotted against energies from TD-DFT. The line of best fit ($R^2 = 0.87$) is shown as the dashed line. Both methods used a PBE0/Def2-SVP level of theory.

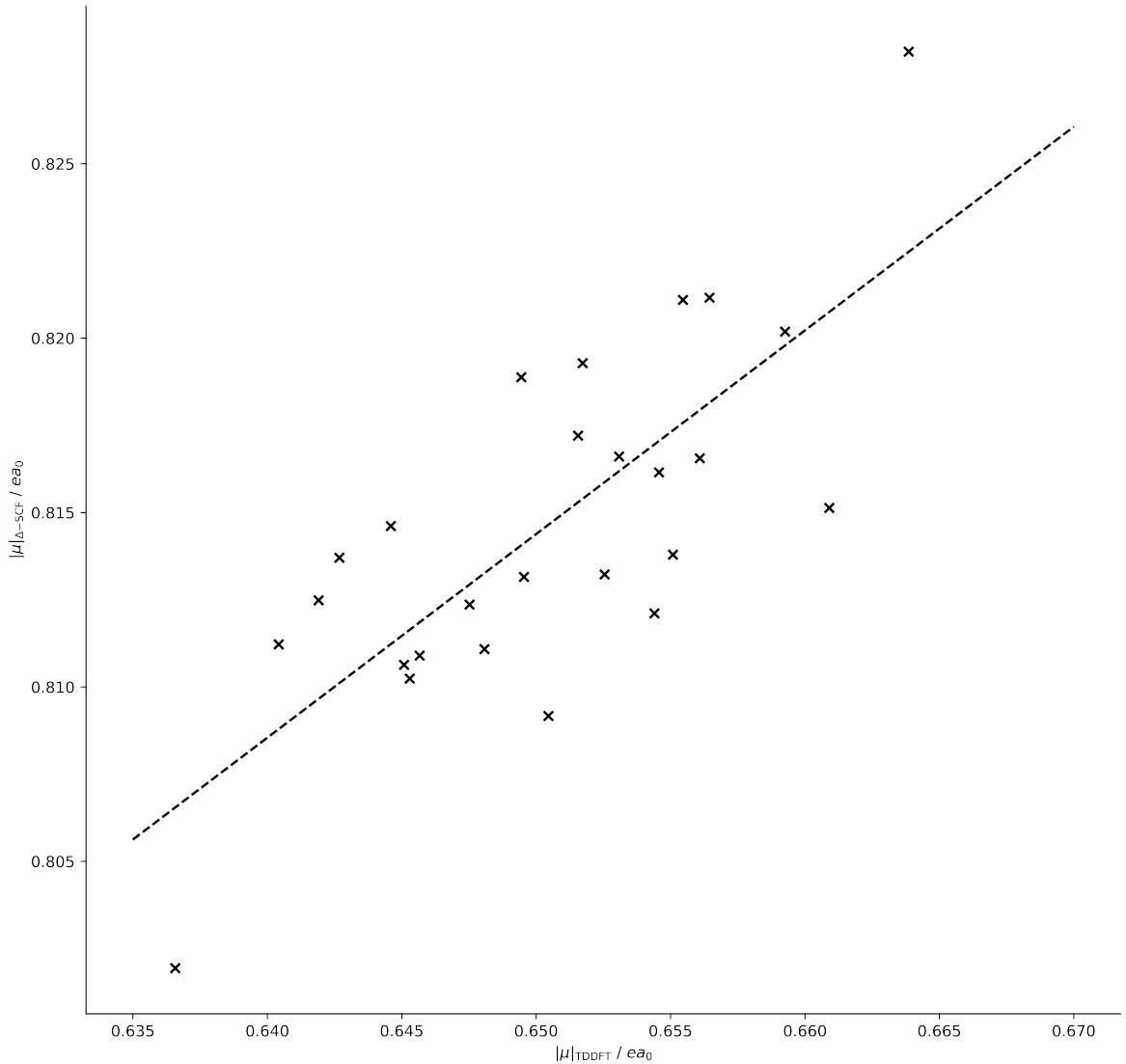


Figure 2.5: Transition dipole magnitudes from Δ -SCF for the same 26 chlorophyll geometries as 2.2.4, plotted against dipole magnitudes from TD-DFT. The line of best fit ($R^2 = 0.57$) is shown as the dashed line. Both methods used a PBE0/Def2-SVP level of theory.

2.2.5 xTB methods

Δ -xTB was tested on the same small molecule benchmark set. Its performance was compared to other low-cost methods, with a range of approximations for calculating transition properties, including the aforementioned sTDA-xTB method. To include this in the comparison, it was necessary to use spin-component-scaled second order coupled-cluster (SCS-CC2) [15, 16] reference data produced by Grimme et al. [12]. Concurrent to this work, the GFN0-xTB method was also implemented in QCORE. This method is similar to the GFN1-xTB method, but excludes any charge dependent terms in its Fock matrix so is not self-consistent. This method therefore only uses a single diagonalisation, with orbital solutions being the same for both ground and excited state. A transition energy from Δ -SCF with this method would functionally be the same as an eigenvalue difference, and this was included in the benchmarking to test whether it would be a possibility for predicting transition properties. Also included in this benchmarking are the eigenvalue differences from sTDA-xTB, given by the `xtb4stda` program [13], to observe how much the sTDA procedure can improve transition properties. `xtb4stda` is the first of two programs that runs a version of xTB, providing molecular orbital coefficients and energies for the sTDA program to then use to calculate the transition properties.

The full list of methods included in the comparison is:

- High level TD-DFT, with a range separated functional CAM-B3LYP and a aug-cc-pVTZ basis set.
- Lower level TD-DFT, with a PBE0 functional and smaller Def2-SVP basis set.
- Δ -SCF with CAM-B3LYP/aug-cc-pVTZ.
- Δ -SCF with PBE0/Def2-SVP.
- linear response with GFN1-xTB and GFN0-xTB.
- Δ -SCF with GFN1-xTB and GFN0-xTB, named Δ -xTB .
- Full sTDA-xTB.
- sTDA-xTB eigenvalue difference.

A source of error that hasn't been discussed in much detail so far is the assignment of transitions between different methods. A known problem of Δ -SCF methods is that the excited state SCF cycle may not converge to the correct state, or it might collapse back to the ground state. This could be seen in the symmetry of the excitation if Δ -SCF has converged to a different transition than TD-DFT and CC2 it would predict a different symmetry of transition. The benchmarking discussed above used symmetry labels to assign TD-DFT transitions to EOM-CCSD, but as noted earlier this was not always possible, and assigning symmetry labels to Δ -SCF

was not possible. Instead, transition dipole orientations and plots of MOs were used as a proxy. This proved harder in the Δ -xTB case for two reasons. Firstly, the valence basis set for the Δ -xTB calculations are very different to those used in DFT. Second, this information was not available for the CC2 data, although the symmetry labels were. Additionally, inspecting the symmetry is very time-consuming and can not be automated. Every new method that was added to the benchmarking had to have every molecule individually inspected to make sure the symmetry of each transition was correct. Assigning symmetry to Δ -SCF results was investigated, but was not a straightforward implementation, as discussed in the following section.

2.2.5.1 Post-SCF Assignment of Symmetry

Symmetry is a common thread in many parts of electronic structure theory. It appears in normal mode analysis, wave-function analysis and assignment of electronic transitions. For this project, assigning symmetry to the transitions for Δ -SCF would require assigning symmetry to the MOs and overall wave-function of a molecule. Broadly speaking, most electronic structure codes have two choices in assigning symmetry to orbitals - either all of the SCF code will treat symmetry from the outset, or nothing is assigned in the SCF code and assignment will happen post-SCF. Both these approaches have benefits and drawbacks. The first method allows the symmetry to be given at any point in the SCF procedure, and allows the Hamiltonian to be organized into a block diagonal matrix. This can be useful when solving for a large basis set or large system as the matrix diagonalisation can be partitioned and parallelised over several cores or nodes on a cluster computer. However, this works best if the system is highly symmetric, which is often not the case when treating unoptimized systems, such as those from a molecular dynamics simulation, and is definitely not the case when looking at biological systems. The second approach, assigning symmetry after the SCF cycles, doesn't fix these drawbacks, but it does allow for codes which originally didn't have symmetry assignment to be extended without rewriting SCF code. The obvious drawback of doing assignment post-SCF is that symmetry can't be utilized during the SCF procedure. The second approach was opted for, as this was the easiest to implement in QCORE. The open source library libmsym [1] was used for point group assignment routines and finding the symmetry adapted linear combination of atomic orbitals. The steps for assigning orbital symmetry is as follows:

1. Determine the point group of the molecule, from the atomic positions
2. Set up the atomic orbitals in the libmsym representation.
3. Get the symmetry adapted linear combinations (SALCs) of atomic orbitals for each subspace.
These subspaces are the groups of symmetries that can be found in the point group of the molecule.
4. The SALCs can then be used to construct the transformation matrix T .

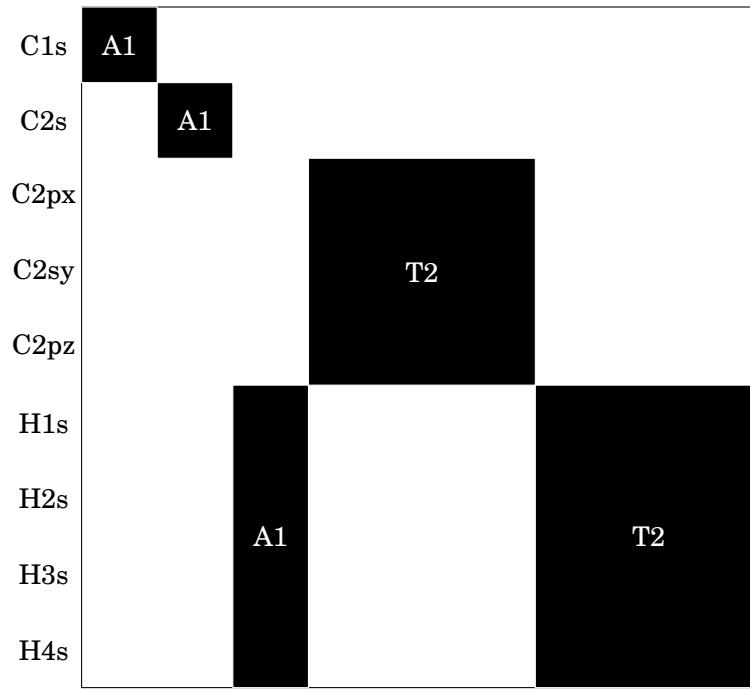


Figure 2.6: A breakdown of the symmetry orbitals in STO-3G methane into the subspaces present in the T_d point group.

5. Assign the one electron molecular orbital (MO) for these subspace characters with the symmetry adapted linear combinations.
6. Multiply the one electron MO symmetries together to find the symmetry of the overall wavefunction.

This procedure was implemented and tested on methane with a minimal STO-3G basis set. It was found that this could accurately assign the MOs and overall wavefunction of methane the ground state.

To assign a label to each molecular orbital, the character of each orbital in all subspaces was looked at. This required transforming the molecular orbital coefficients \mathbf{C} into each subspace A by using the transformation matrix \mathbf{T} , defined by

$$(2.22) \quad \tilde{\mathbf{C}}_A = \mathbf{T}_A^T \mathbf{S} \mathbf{C}$$

, and then summing the coefficients to obtain the character

$$(2.23) \quad P_A = \sum_v |\tilde{\mathbf{C}}_{A,\mu\nu}|$$

, where μ, ν are indices for the atomic and molecular orbitals respectively. The molecular orbital with character equal to 1 in a subspace would then have that symmetry label, and would be a well defined assignment. However, in practice this was not always clear cut and so the highest subspace character was taken as the assignment.

The MOs for an optimised methane geometry with an STO-3G basis set was correctly assigned - two occupied orbitals and one unoccupied orbital of A1 symmetry, and three occupied and unoccupied orbitals of T2 symmetry. The overall wavefunction symmetry can then be expressed as the product of all MO symmetries, reduced with the reduction formula

$$(2.24) \quad n = \frac{1}{h} \sum_R \xi_r(R) \xi_i(R)$$

, where ξ_r, ξ_i are the reducible and irreducible representations respectively, h is the order of the group and R is the subspace. This correctly produced the overall symmetries of ground state systems for methane, as well as water.

However the assignment of MOs did not work well for excited states, due to the character from the subspace projection being unclear for many MOs. Furthermore, for non-abelian groups, where there are some degenerate E and T subspaces, this assignment procedure did not work. This is a similar problem to the assignment of symmetry for the TD-DFT and EOM-CCSD transitions in the earlier benchmarking. Often the reduction of ground state wavefunctions gave non-physical answers.

Extending the symmetry analysis to non-abelian point groups was beyond the scope of this work. Although it would be a useful feature for testing the benchmarking sets, chlorophyll molecules would be far from symmetric and so this type of assignment could not have been expected to have worked. In summary, transitions could not be confidently assigned for Δ -SCF with this method.

2.2.5.2 Δ -xTB Benchmarking Results

After considering this leading error, the assignment of symmetry was based on the previously used inspection of transition dipole orientations and transition density plots.

The distributions of absolute errors

$$(2.25) \quad \epsilon = \Delta E_{\text{method}} - \Delta E_{\text{SCS-CC2}}$$

for each of the benchmarking methods, as well as a generated distribution of sTDA-xTB results, are shown in fig-2.7. The means and standard deviations are reported in table 2.1.

Overall, both Δ -xTB methods are inaccurate - far too inaccurate to be used as a viable method for transition properties of chlorophyll, or any other system. The mean error GFN1- Δ -xTB was -0.12 eV, and has a significant standard deviation of 2.11 eV. GFN0- Δ -xTB had a larger mean error

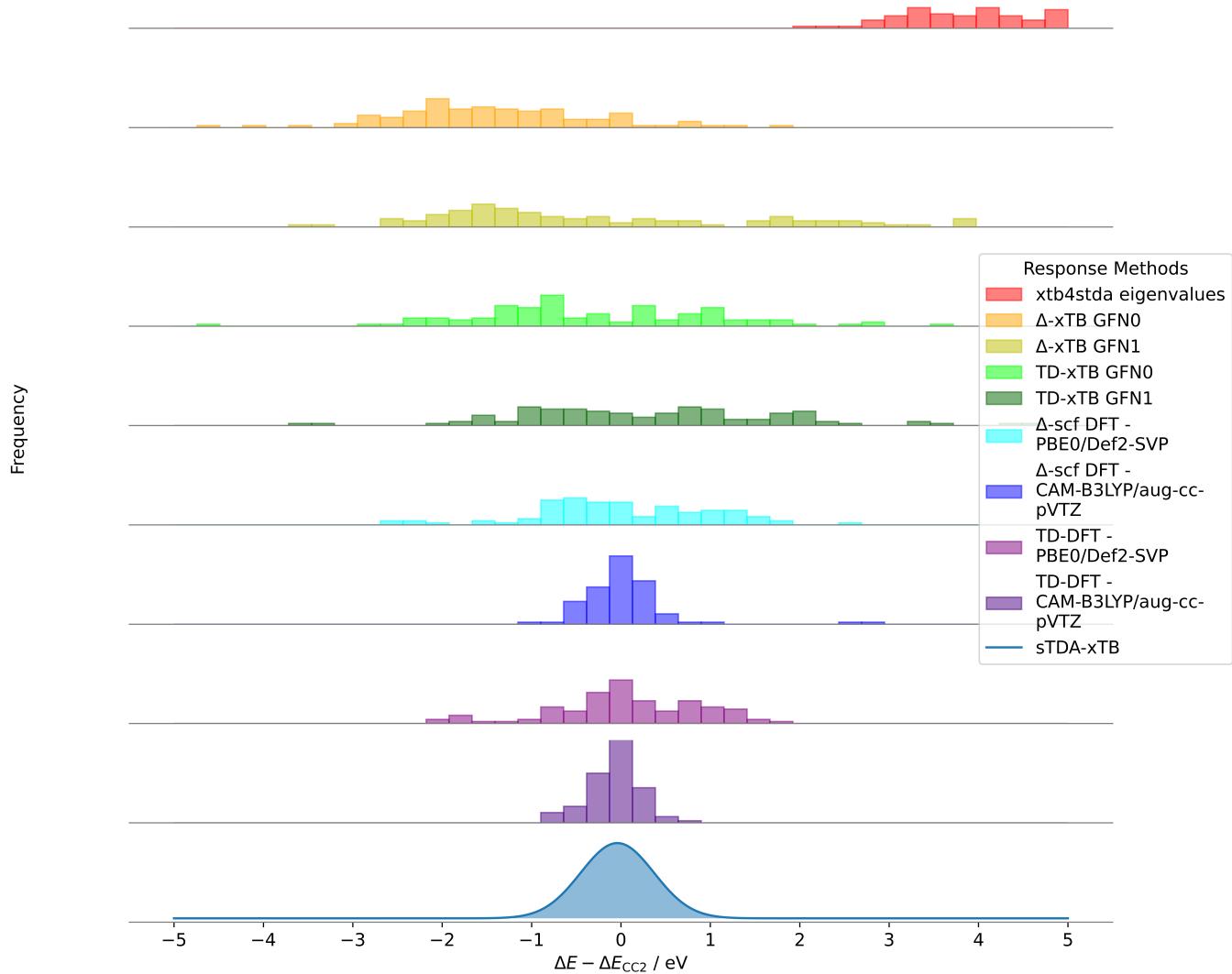


Figure 2.7: The distributions of errors compared to SCS-CC2 transition energies for the methods included in the Δ -xTB benchmarking.

Method	Mean / eV	Standard Deviation / eV
TD-DFT CAM-B3LYP/aug-cc-pVTZ	-0.18	0.34
TD-DFT PBE0/Def2-SVP	-0.06	0.79
Δ -SCF CAM-B3LYP/aug-cc-pVTZ	-0.14	0.28
Δ -SCF PBE0/Def2-SVP	-0.62	0.50
TD-GFN1-xTB	0.27	1.47
TD-GFN0-xTB	-0.41	1.32
Δ -SCF GFN1-xTB	-0.12	2.11
Δ -SCF GFN0-xTB	-1.50	1.08
xtb4stda	4.39	1.26

Table 2.1: Mean and standard deviations of the errors, in eV, against SCS-CC2 reference data. The `xtb4stda` entry represents the eigenvalue difference method that uses the eigenvalues output from this program.

of -1.50 eV, and whilst a slightly smaller standard deviation of 1.08 eV, this is still well beyond a usable accuracy.

The standard deviation should be well inside the value of the transition energy (1.8 eV for Q_y), so a 1 eV accuracy is used as the first test of usable accuracy. Next, in order to be accurate enough to predict variations that cannot be attributed to random noise, the standard deviation must be within the range of excitation energies for LHII chlorophylls, which from 2.2.4 can be seen to be around 0.2 eV. Any more than this and it's uncertain whether the difference between two excitation energies for different chlorophyll geometries are due to geometry reasons or due to random noise.

The DFT methods, both the linear response and the Δ -SCF methods, are still shown to be accurate at predicting excitation energies, with means and standard deviations within ranges previously reported in the above sections.

From these results, it's argued that decreasing the level of theory for the electronic structure dramatically decreases the accuracy of transition properties. The highest level electronic structure method has the best accuracy. CAM-B3LYP/aug-cc-pVTZ TD-DFT and Δ -SCF have mean errors of -0.18 eV and -0.14 eV and standard deviations of 0.34 and 0.28 eV respectively. Both methods are well within the accuracy needed to predict geometry-based variations. The outliers in the Δ -SCF results are known mixed transitions, as discussed earlier with the ethene dimer system. The lower level PBE0/Def2-SVP methods have a marked decrease in accuracy. On going from higher-level DFT to lower level, the standard deviation approximately doubles for both TD-DFT (0.34 eV to 0.79 eV) and Δ -SCF (0.28 eV to 0.50 eV). Again, the PBE0/Def2-SVP TD-DFT and Δ -SCF are comparable, with standard deviations of 0.79 eV and 0.59 eV, although the mean for Δ -SCF has a significant shift of -0.62 eV. However it's clear that the greater effect on accuracy is due to the change in response method rather than level of theory of the DFT calculation. Whilst the same conclusion is not as clear for the semi-empirical methods, the large standard deviations

of all the GFN based methods fail the first test of accuracy, and so can be immediately disqualified. They are all too inaccurate to justify a more detailed analysis. Comparing the DFT and GFN based methods, we can see the same trend that lowering the level of theory gives worse transition properties.

Overall, the most inaccurate method is the eigenvalue difference methods based orbital energies (eigenvalues of the Hamiltonian diagonalisation) from the `xtb4stda` method. The means and standard deviation was 4.39 eV and 1.26 eV respectively, a huge difference to the reported values (-0.04 eV and 0.41 eV respectively)[13]. However it does show that the full sTDA-xTB method can be as accurate as TD-DFT with a range-based density functional and triple zeta basis sets, and so arguably the sTDA method, and not the underlying xTB method, makes up a large part of the accuracy for predicting transition properties. Hence a similar response theory, based on a different xTB theory, could perform equally well if the xTB theory really does not factor into obtaining decent accuracy. This is investigated in the next chapter.

The result that GFN-xTB based methods are not accurate is not unexpected. As opposed other DFT method, which use *ab initio* or first principle parameters, the xTB methods were fit to target properties, and so could not be expected to be suitable for other properties outside the training data [3]. Whilst GFN-xTB is better for number and specificity of parameters than many other methods because of this "top-down" parameterisation approach, these parameters only extend the accuracy of predicted properties to different chemical systems (due to a lack of pair-wise parameters), and not to different properties altogether.

2.3 Conclusions

The transition properties of a test set of small molecules has been benchmarked with multiple Δ -SCF , TD-DFT and high-level methods. It has been shown that DFT based Δ -SCF and TD-DFT methods can reproduce the same transition energies and transition dipole magnitudes as EOM-CCSD to within reasonable levels of accuracy. For the set of small molecules, transition energies were predicted with a mean of less than 0.5 eV, and 0.07 a.u. for transition dipole magnitudes. Additionally, the issue of breaking the origin independence property of transition dipoles has been shown to be fixed by using a symmetric orthogonalisation of the two originally non-orthogonal states.

For a small set of BChla geometries, it was found that the same level of accuracy for transition energy could be found between Δ -SCF and TD-DFT, where EOM-CCSD was too expensive to calculate. The error was well within the range of TD-DFT energy variation, shown in the high correlation coefficient, and so Δ -SCF could be reasonably expected to give correct geometry-dependent transition energies. Whilst the accuracy is slightly reduced for transition dipole moments, the appreciable degree of correlation implies that qualitative statements would be valid.

With all of the above benchmarking, reliably obtaining and assigning transitions predicted from Δ -SCF has proved to be an unsolved issue. Either Δ -SCF is formally unable to predict the correct character of transitions, as showcased in the ethene dimer mixed transition outlier, or it is unreliable in finding excited state solutions. This is best shown in the exclusion of a geometry of chlorophyll that could not be made to converge to the correct excited state, as well as the necessary use of Fock damping, altered DIIS procedures and intermediate initial guesses to investigate whether the convergence could be fixed.

To solve the inability of currently implemented Δ -SCF to assign symmetry labels, a post-SCF method of assigning MO and full wavefunction symmetry was investigated, but ultimately proved beyond the scope of this project. Whilst able to assign labels for small, trivial systems of STO-3G water and methane, non-trivial excited states and more complex systems did not work. Whilst there is more work that could be done in this area, it was decided that this should be moved to potential further work on Δ -SCF methods.

Additionally, whilst DFT based Δ -SCF methods are shown to be accurate, GFN-xTB based methods were found to be inaccurate, to the point where it cannot be claimed to be a useful proxy to higher level methods. Due to the similarity in results for linear response and Δ -SCF methods over a range of electronic structure methods, from high level DFT to lower level GFN-xTB methods, this drop in accuracy is attributed to the different electronic structure theory used, rather than the response methods. This implies that altering the electronic structure method could lead to great improvements in the accuracy of a new response method.

The aim of this chapter was to determine whether Δ -SCF methods, which have a simple gradient theory and are less costly than TD-DFT, could provide a sufficiently accurate description of transition properties for use in an ab initio exciton framework. It's been shown that this is true with the condition that the underlying theory is sufficiently high. The issue of non-orthogonality has shown to have a solution that does not decrease the speed or accuracy of this method, and whilst the problem of symmetry assignment is still unsolved, this is not as much of an issue when only the Q_y transition of chlorophyll, which is well defined by its transition dipole, is needed.

However, the fact that higher level DFT is required for accurate transition properties is an issue for simulating a large volume of chlorophyll structures. The efficiency of these calculations is too low for an exciton framework, which would require in the region of 1e5 to 1e6 calculations for a full time series of LHII. Semi-empirical Δ -SCF methods, which would be efficient enough and have tractable gradients, prove inaccurate in their current form. However, it is demonstrated that a correct electronic structure and "top-down" parameterisation could make an accurate semi-empirical method. This is investigated in the following chapter.

CHLOROPHYLL SPECIFIC METHODS

This chapter reports the work done on designing and parameterising a novel method for response properties. The framework and theory for the method is outlined in section 3.1. Parameterisation details are given in section 3.2, including the reference data that compromised the training data, the objective function used and the algorithms that were used for optimisation. The accuracy of this new method is showcased in the final section 3.3.

3.1 Theory

This section covers the approximations to full linear response theory that leads to the novel chl-xTB method. Starting from the eigenvalue equation, that is derived more fully in the theory chapter but recapped here, a few key approximations lead to a framework that has tractable gradients and is less expensive than full linear response. This fulfills the requirements set out in the introduction of having an efficient and simple, but accurate, method of getting transition properties for LHII chlorophylls.

3.1.1 Full solutions TD-DFT equation

In linear-response TD-DFT, excitation energies and characters are the solutions of the non-Hermitian eigenvalue equation

$$(3.1) \quad \begin{pmatrix} \mathbf{A} & \mathbf{B} \\ \mathbf{B}^* & \mathbf{A}^* \end{pmatrix} \begin{pmatrix} \mathbf{X} \\ \mathbf{Y} \end{pmatrix} = \omega \begin{pmatrix} 1 & 0 \\ 0 & -1 \end{pmatrix} \begin{pmatrix} \mathbf{X} \\ \mathbf{Y} \end{pmatrix}$$

where \mathbf{A} , \mathbf{B} are matrices whose elements describe the perturbation of the electron density, the \mathbf{X} , \mathbf{Y} solutions are the coefficients of excitations, similar to CIS, and eigenvalues ω are the excitation energies.

The elements of \mathbf{A} and \mathbf{B} correspond to descriptions of the virtual-occupied and occupied-virtual contributions respectively, and in TD-DFT, with a global hybrid density functional, are given by

$$(3.2) \quad A_{ia,jb} = \delta_{ij}\delta_{ab}(\epsilon_a - \epsilon_i) + 2(ia|jb) - a_x(ij|ab) + (1 - a_x)(ia|f_{XC}|jb)$$

$$(3.3) \quad B_{ia,jb} = 2(ia|bj) - a_x(ib|aj) + (1 - a_x)(ia|f_{XC}|bj)$$

where indices a, b and i, j refer to virtual and occupied orbitals respectively, ϵ_i is the orbital energy of orbital i , a_x is the value of non-local Fock exchange in the XC functional f_{XC} . δ_{ij} is the Kronecker delta function. The intergrals (here in Mulliken notation) can be seen to be of Coloumb type for the \mathbf{A} matrix and exchange for the \mathbf{B} matrix. The leading term in the \mathbf{A} matrix is the orbital energy difference, which is contributes to the diagonal elements only due to the Kronecker deltas.

3.1.2 Approximations to Solutions

There are three approximations made in the chl-xTB method. First is the Tamm-Danoff approximation (TDA), which eliminates three blocks of the full linear response matrix. Second is a diagonal dominant approximation to eigenvalue solutions, where diagonal elements of a matrix are taken as an approximation to true eigenvalues. The third is a monopole approximation to two electron integrals which employs MNOK operators to accurately capture Coulomb and exchange functions. All these approximations reduce the amount of expensive electron integrals required to construct the full eigenvalue equation, whilst still capturing the important aspects of the electron density response.

3.1.2.1 Tamm-Danoff approximation and Diagonal Dominant A matrices

One of the earliest approximations applied to full linear response was the Tamm-Danoff approximation, where only virtual-occupied contributions are calculated. This sets all of the elements of \mathbf{B} matrix to zero, and reduces the full eigenvalue equation to

$$(3.4) \quad \mathbf{AX} = \omega\mathbf{X}$$

where the definitions of elements are the same as above, but it should be noted that the solutions \mathbf{X} will be not be same. This is formally the same as a CIS problem, and has been reported as a way to get back to CIS from full TD-DFT.

As an eigenvalue problem, solving for ω requires constructing and diagonalising the full \mathbf{A} and then diagonalising. The XC functional is dependent on ω values and so several iterations of this diagonalisation are needed to find stable, self-consistent solutions.

If the matrix is diagonal dominant, the diagonal elements of the \mathbf{A} matrix can be used as an approximation to the eigenvalue solutions. This would be in the limit where the coupling elements (the off-diagonal elements) tend to zero, which would be the case for an excitation that is mostly made up of a single transition. Excitation energies would be given by

$$(3.5) \quad \omega_{ia} \approx A_{ia,ia} = (\epsilon_a - \epsilon_i) + 2(i|ia) - a_x(ii|aa) + (1 - a_x)(ia|f_{XC}|ia)$$

. If the integrals are assumed to be small compared to the first term orbital energy difference, then the orbital energy difference can be taken as an approximation to the full excitation energy, recovering the eigenvalue difference method from the previous chapter.

By removing the eigenvalue problem, the gradients of the excitation energies are more tractable. However the integral terms still require an iterative, self-consistent treatment. This can be simplified by using an approximation to these integrals that uses point charge interactions.

It should be noted that further cost is removed by not needing to calculate not only all of the off-diagonal elements but the diagonal elements for transitions that are not of interest. This however would only be in the case where transitions are not mixed. If transitions are mixed, then the coupling elements should be considered and approximating them to be zero would not be valid. This is considered in section 3.1.4.

3.1.3 Integrals approximations

The two electron integrals as written above are usually one of the most expensive part of an electronic structure calculation. These can be approximated with a monopole expansion, treating atomic sites as point charges, and using a charge-charge interaction for the energy.

Atom centered transition charges for transition $m \rightarrow n$ can be given in the Mulliken scheme by summing the reduced one-electron transition density \mathbf{D}^{mn} multiplied the orbital overlap \mathbf{S} for all orbitals p centred on atom A

$$(3.6) \quad q_A^{mn} = \sum_{p \in A} D_{pq}^{mn} S_{pq}$$

. Partial charges can be given as the difference between the electronic charge and the nuclear charge Z_A

$$(3.7) \quad q_A = Z_A - \sum_{p \in A} D_{pq} S_{pq}$$

where \mathbf{D} is the reduced one-electron density. This applies to any state, so can be used to calculate ground state and excited state partial charges.

MNOK operators can recover the important behavior of full electron integrals that is lost in classical charge-charge interaction, especially for the small distance limit. For both coloumb and exchange type integrals, this can be done with a short-range damped MNOK operators. The integral is approximated by

$$(3.8) \quad (pq|rs) \approx \frac{1}{2} \sum_{A}^N \sum_{B}^N q_A^{mm} q_B^{mn} \Gamma_{AB}$$

where N is the total number of atoms in the system and p, q, r, s are electron indices for both occupied and virtual orbitals. A and B are indices for the atoms. For Coloumb type integrals, the operator Γ_{AB} is given by

$$(3.9) \quad \Gamma_{AB}^J = \left(\frac{1}{(R_{AB})^{y_J} + (a_x \eta)^{-y_J}} \right)^{\frac{1}{y_J}}$$

where R_{AB} is the interatomic distance and η is the average of the chemical hardnesses. The chemical hardness of a given atom is defined as

$$(3.10) \quad \eta(A) = \frac{\delta^2 E(A)}{\delta^2 N^2}$$

but in practice is precomputed and used as a static parameter. y_J and a_x are global parameters, with the later used to recover the effects of Fock-exchange mixing in the short-distance limit. For exchange type, the operator is

$$(3.11) \quad \Gamma_{AB}^K = \left(\frac{1}{(R_{AB})^{y_K} + \eta^{-y_K}} \right)^{\frac{1}{y_K}}$$

where the y_K parameter replaces the y_J parameter in the Coloumb type operator.

As the a_x parameter can "mop up" many of the exchange effects, the density functional in equation 3.5 is also neglected to further reduce computational cost. The final form of the expression used to calculated excitation energies is then given by

$$(3.12) \quad \omega_{ia} = (\epsilon_a - \epsilon_i) + \sum_{A,B}^N \left(2q_{ia}^A \Gamma_{AB}^K q_{ia}^B - q^A \Gamma_{AB}^J q^B \right)$$

where the exchange term uses transition charges q_{ia} , and the Coloumb term uses partial charges from the ground state density.

It can be seen that the inclusion of MNOK operators introduces global parameters. These would require optimisation to a training set. Initially it was investigated whether parameterising to a training set with a broad range of systems and transitions would be possible. However it was found that parameter optimisation procedures, whilst improving upon the accuracy of the Δ -xTB methods of the previous chapter, could not break into the accuracy needed to investigate chlorophyll systems well enough (discussed in more detail in 3.2.3). This is due to many transitions not being single character which would be not be consistent with the diagonal dominant approximation. Additionally, the same issues as the previous chapter in assigning transition without symmetry made any autonomous optimisation workflow difficult.

However a method that works for a wide set of systems is not required for LHII, as only the Q_y transition is of interest for many models. Parameterising to a single, well-defined transition would be a much better approach for this investigation. By reducing the scope of systems, the specificity of parameters can dramatically increase. This reduces the need to include more parameters to improve accuracy, as well as decreasing the amount of training data needed. Looking at other transitions and systems then is outside the scope of this work, but could be a large area for further work for similar investigations. An outline of the Q_y transition, and its applicability to these approximations, is given below.

3.1.4 Q_y Transition

The Q_y transition is a good candidate to test approximations to full linear response theory. It is a well-defined transition which makes assignment easy, and has been thoroughly analysed in the literature. It is also the most important transition in light harvesting systems, so an accurate treatment is necessary.

The Q_y transition is the one of the two transitions that make up the Q band in the absorption spectra of chlorophyll, the other being the Q_x transition. It is well known that the Q_y transition is important for electronic energy transfer, and predicting both transition energies and transition dipole magnitudes and orientations is important to construct frameworks for this transfer. The Q_y transition is mostly HOMO-LUMO in character (96%), with a small amount of HOMO-1 - LUMO+1 (remaining 4%). The analogous transition in the unsubstituted tetraphorphyrin ring has the transition dipole along the molecular axis defined by the N atoms, however due to the asymmetry introduced by substitutions and geometry deformations, this is usually not the case for BChla with a deviation from this axis of around 12 °. The Q_y transition in chlorophyll has its dipole component lying along the N_A-N_C axis with Q_x lying orthogonal, along the N_B-N_D axis. Q_x has the reverse character to the Q_y transition, being mostly HOMO-1 - LUMO+1.

Plots of the electron density of the HOMO and LUMO show how this transition is delocalised over large sections of the porphyrin ring, with approximate C_2 symmetry along the molecular axes. Notable contributions can be seen in the functional groups, giving the modified transition behaviour seen in different versions of chlorophyll, as well as the appearance of some features in

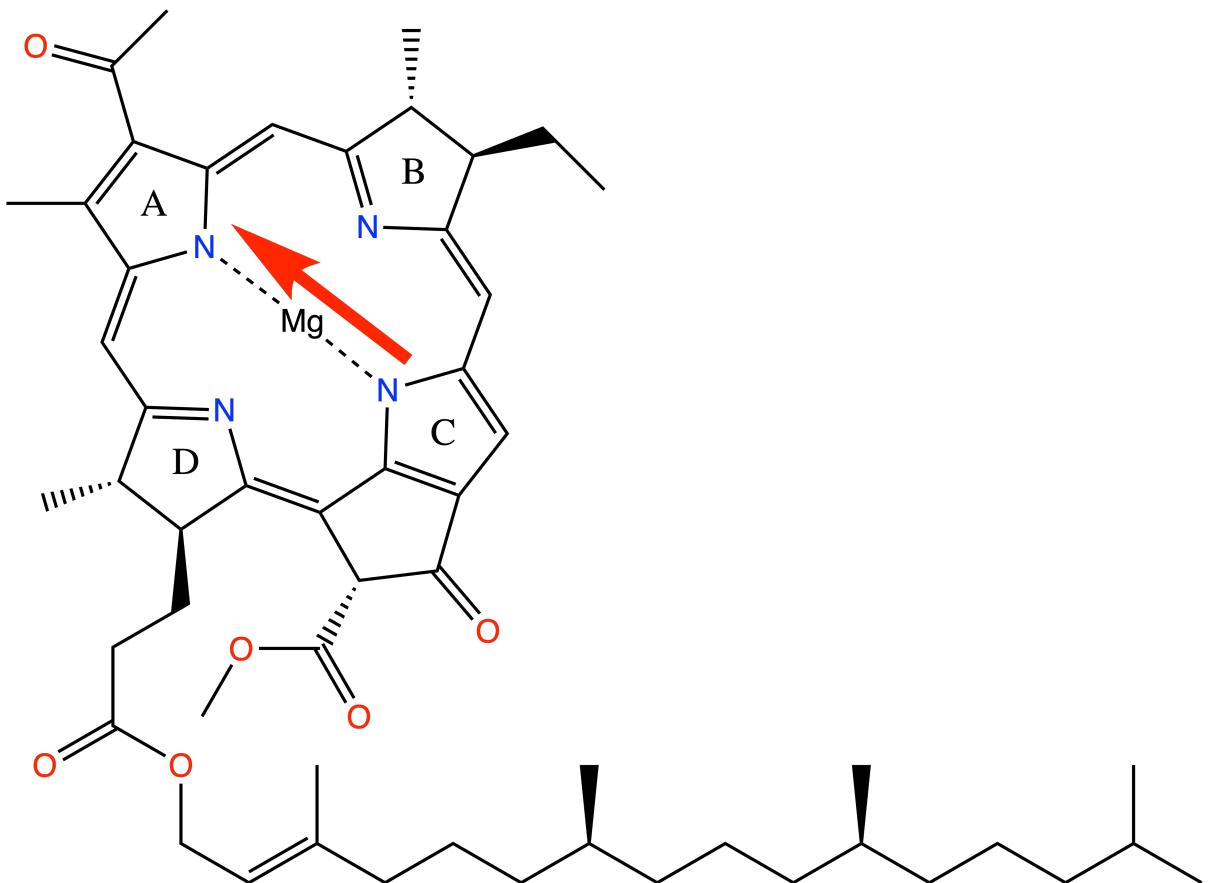


Figure 3.1: Bacterial Chlorophyll a (BChla) with a model Q_y transition dipole.

spectral density (discussed further in chapter 5).

It has recently also been shown that the high correlation between the eigenvalue difference of HOMO-LUMO orbitals and full TD-DFT excitation energies implies that the HOMO-1 - LUMO+1 transition can be excluded from the transition character. This is also supported by the results for the chlorophyll test set in the previous chapter, as Δ -SCF with its single transition treatment is able to capture Q_y transitions with good accuracy.

The high amount of single-transition character in the Q_y transition makes it ideal for the approximations to transition energies set out earlier. The lack of coupling elements that would appear in the **A** matrix justifies both the use of the diagonal dominant approximation and TDA. The almost exclusive centering of electron density on main group elements make the use of MNOK integrals also valid.

Additionally, the well-defined transition make assignment trivial, and the transition dipole orientation to the N_A-N_C axis has been used as a metric for the accuracy of transition dipole moments. As a single value, this is ideal for autonomous optimisation both for use in an objective function as well as for discarding outlier transitions.

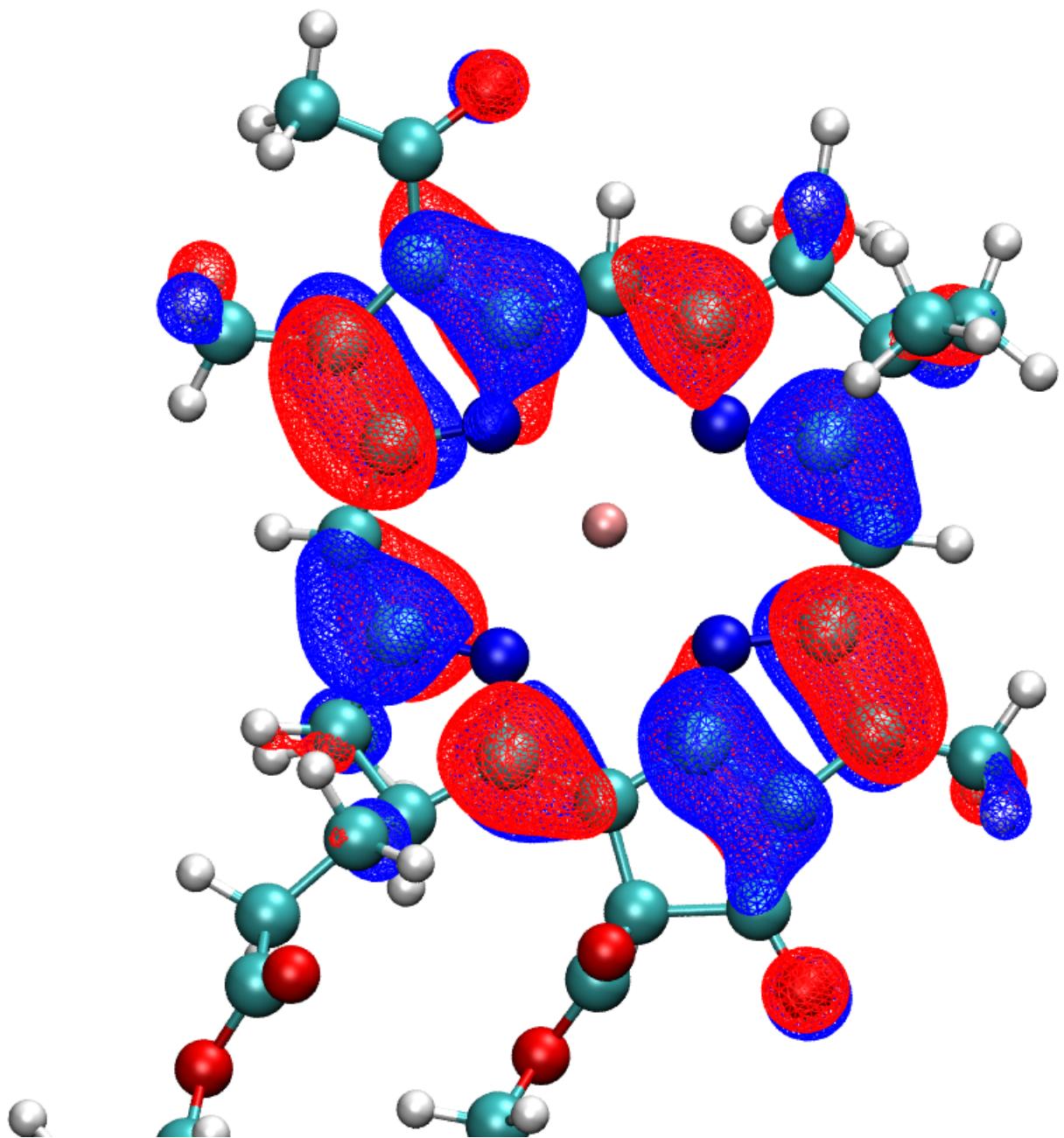


Figure 3.2: The HOMO orbital of bacterial chlorophyll a from PBE0/Def2-SVP DFT.

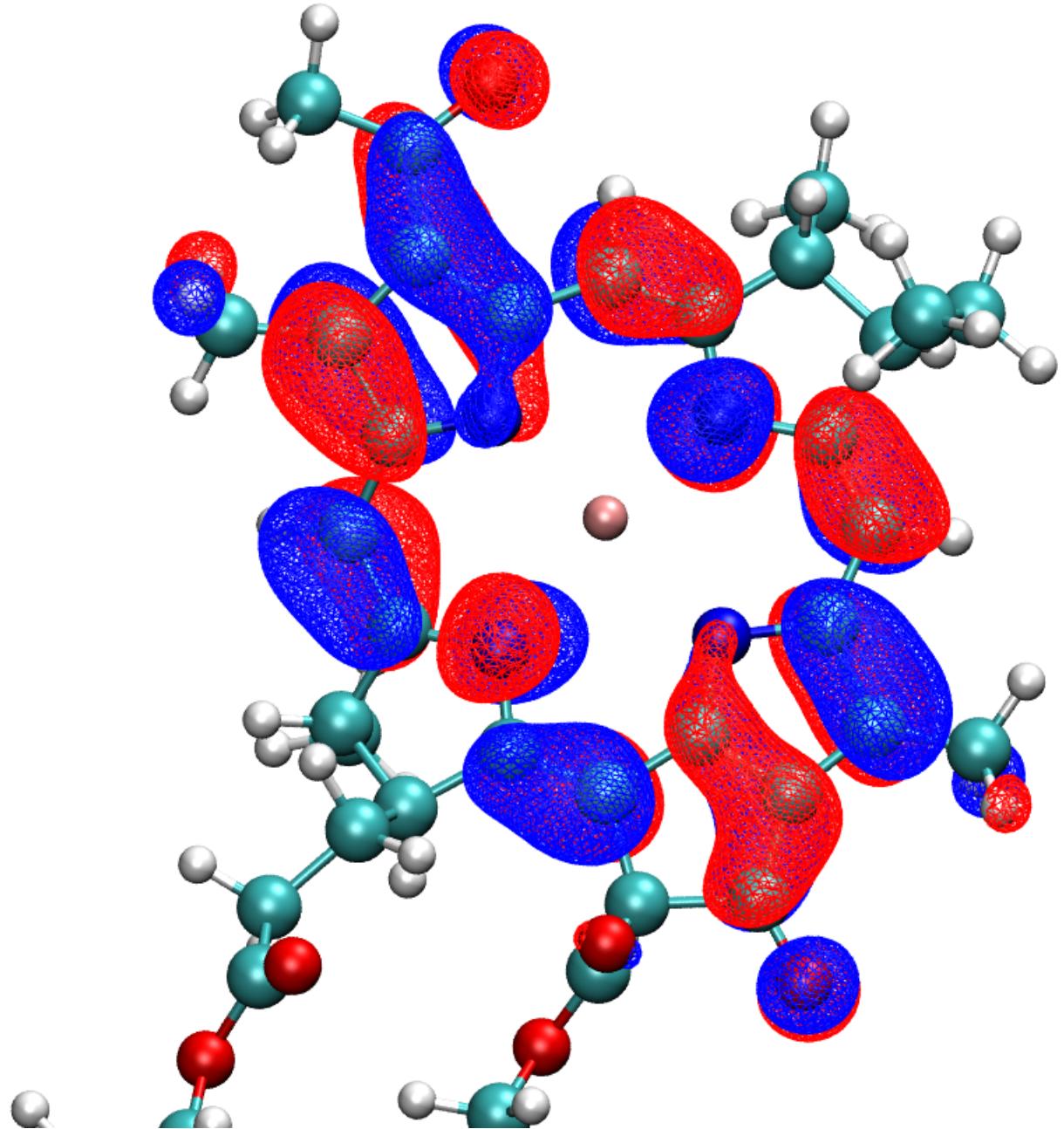


Figure 3.3: The LUMO orbital of bacterial chlorophyll a from PBE0/Def2-SVP DFT.

The Q_y transition was then used to benchmark the novel response approximations. The optimisation and construction of reference and training set data is discussed later in section 3.2.

3.1.5 Changes to xTB parameters

As found in the last chapter, the underlying electronic structure can have a huge effect on the accuracy of transition properties, in some cases more than a change in the response method. The xTB methods in particular, both linear response and Δ -xTB, were particularly ill-suited for transition properties. Whilst DFT methods could have been used as for Mulliken partial and transition charges, this would still not be efficient enough to calculate the large volume of geometries from LHII. A tight-binding, semi-empirical approach for the electron structure is still required. To improve the applicability of the xTB methods for transition properties, it was decided that some of the parameters would need to be altered. A top-down approach was used for these alterations, as it has been shown to work well for the GFN-xTB and sTDA-xTB methods.

As discussed in the theory chapter, the GFN1-xTB Fock matrix is made of both charge dependent and charge independent terms. The form of these terms, and definitions of parameters, is also given in the theory chapter. Only the charge dependent terms would have any effect on the partial and transition charges, thereby effecting the transition properties. The charge dependent terms are the first, second and third density fluctuation terms. The first order term is the leading term, and so parameters present in this term were chosen to be included in the optimisation procedure to prioritise parameters that would have the largest effect. Only some of these parameters are "free", whilst others are based on physical or *ab initio* values. These are the Hückel parameters k_l , where l is the angular momentum of the orbital, and the global scaling parameters. The global scaling parameters are used to adjust interactions for some pairs of elements where the global parameters led to incorrect bond lengths. It was found that for the Q_y transition, only Mg and N interactions had to be scaled.

An obvious drawback of altering these parameters to fit to transition properties is that they would lose their specificity to the GFN-xTB training set. However it is not in the scope of this work to find a semi-empirical method that would be able to calculate these properties for chlorophyll. chl-xTB is not used to calculate optimised geometries or hessians of chlorophyll as other methods could be expected to perform better. Also if this were the necessary, including more target properties in the parameter optimisation would decrease the accuracy to any one target, making the method worse overall. For example, the sTDA-xTB and GFN-xTB methods use different electronic structure parameters for this reason.

3.1.6 Transition and Excited State Density from the Ground State

Similar to Δ -SCF, the ground state orbital coefficients are taken to be a good approximation to the (Q_y) excited state coefficients. It was assumed then that the excited state could be calculated

without orbital relaxation, so that both the excited state and ground state could be constructed from the same set of molecular orbitals. The transition density is then calculated as

$$(3.13) \quad \mathbf{D}^{01} = |\Psi^0\rangle\langle\Psi^1|$$

with $|\Psi^0\rangle$, $|\Psi^1\rangle$ (the ground and excited state respectively) being constructed from the same set of molecular orbital coefficients \mathbf{C}^0 but with different sets of occupation numbers for the ground and excited state. The ground state and excited state density can be similarly calculated as

$$(3.14) \quad \mathbf{D}^0 = |\Psi^0\rangle\langle\Psi^0|$$

$$(3.15) \quad \mathbf{D}^1 = |\Psi^1\rangle\langle\Psi^1|$$

. These density matrices are used to calculate the partial and transition charges with the Mulliken scheme, which is in turn used to calculate the MNOK integrals. The transition and molecular dipoles can be calculated as the trace of the dipole operator with the density.

It should be noted the ground and excited states would be orthogonal in this scheme, as they share the same set of MO coefficients. Additionally, only one cycle of the SCC procedure would be necessary, which would eliminate the problem of convergence in the Δ -SCF excited state. It would also halve the computational time. Excited state properties, such as the molecular dipole and partial charges can also be calculated from the excited state density, which will be important for the exciton framework of the next chapter.

It was found, however, that transition dipoles calculated using this method were much larger than TD-DFT. This was also observed for the Δ -SCF and eigenvalue difference methods, implying that the inclusion of the HOMO-1-LUMO+1 transition is key to accurately describing the transition density. To recover this, an additional parameter was included to scale the transition density, which both yielded the correct transition dipole magnitudes as well as drastically increasing the accuracy of the method overall. This is discussed more in section 3.2.3.

3.2 Parameterization

An objective function and algorithm is required to find minima in the parameter space, where the minima correspond to an optimised set of parameters. Reference data is also required as a target. All of these elements are important for minimising the amount of error in the final method, as well as determining how well chl-xTB performs for different problems and other properties.

3.2.1 Objective Function

At first, it would be argued that the root mean squared error (RMSE) to the reference transition energy should be the value that should be minimised, giving the objective function as

$$(3.16) \quad f_{\text{RMSE}}(\mathbf{x}) = \sqrt{\frac{1}{N} \sum_i^N (\Delta E_i - \Delta E_{i,\text{ref.}})^2}$$

where \mathbf{x} is the set of parameters, ΔE_i , $\Delta E_{i,\text{ref.}}$ are the transition energies for system i from the chl-xTB method and reference method respectively, N is the number of systems used to calculate the objective function value (these can be different when looking at training and testing sets).

However just using the RMSE has two issues. First is that other transition properties are not included in the optimisation, so the transition dipoles would be expected to have a large error. This can be fixed by including a metric for the error in transition dipoles. The other issue is that a low RMSE does not guarantee a high correlation. A measure of the correlation can be given by the coefficient of determination

$$(3.17) \quad R^2 = 1 - \frac{\sum_i^N (\hat{y}_i - y_i)^2}{\sum_i^N (\hat{y}_i - \bar{y})^2}$$

where \hat{y} , y are the predicted and reference values, and \bar{y} is the average of the reference values. The correlation is a better metric for determining if chl-xTB has a small enough random error to predict transition properties, however it may not account for systematic errors. Both a low RMSE and high R^2 value are needed to optimise fully to the reference data, and the two metrics are not mutually inclusive.

By including both RMSE and R^2 values, for transition energies as well as dipole magnitudes, the full objective function used was

$$(3.18) \quad f_{\text{full}}(\mathbf{x}) = \lambda_1 \text{RMSE}(\Delta E) + \lambda_2 \text{RMSE}(|\mu|) + \lambda_3 (1 - R^2(\Delta E)) + \lambda_4 (1 - R^2(|\mu|))$$

where λ_n are weights necessary to keep all of the terms to a similar range. This provides stability to the optimisation procedure, such that no one term dominates the solution space.

3.2.2 Minimisation Algorithms

Finding the optimal parameters for the chl-xTB method is a nonlinear problem. The parameters so far stated can not be used to create a linear function that would reproduce the value of the objective function. Therefore it's necessary to use heuristics that can solve for these problems.

3.2.2.1 Nelder-Mead

The Nelder-Mead method, as implemented in SciPy, is a modified version of a simplex algorithm, that uses a n -dimensional shape to define a test region, and iteratively searches the n -dimension space by reflecting the vertices of the test region. The test region, or more specifically the shape described by its vertices, is the simplex. The simplex has $n + 1$ vertices - for example, a 2-dimensional problem would have a triangular simplex. The algorithm starts with an initial simplex guess. It is important that the initial guess covers enough area to avoid descending into any local minima, whilst not being too large as to not take into account finer details of the parameter space. The simplex is propagated by using a central value of the set of vertices, and using this to either expand, contract or shrink the simplex, or reflect one of the vertices. For example to find the parameters \mathbf{x} that correspond to a minimum of the function $f(\mathbf{x})$

$$(3.19) \quad \min_{\mathbf{x} \in \mathbb{R}^n} f(\mathbf{x})$$

with initial simplex vertices $\mathbf{x}_1, \dots, \mathbf{x}_{n+1}$, the first step is to order the function values of the vertices

$$(3.20) \quad f(\mathbf{x}_1) \leq f(\mathbf{x}_2) \leq \dots \leq f(\mathbf{x}_{n+1})$$

and calculate the centroid of the set of vertices, excluding the worst vertex \mathbf{x}_{n+1} . The next steps then propagate the simplex, first by testing whether a reflection point \mathbf{x}_r is better than the worst vertex used to calculate the centroid

$$(3.21) \quad \mathbf{x}_r = \mathbf{x}_0 + \alpha(\mathbf{x}_0 - \mathbf{x}_{n+1})$$

where \mathbf{x}_0 is the centroid point. There are then a set of three possibilities for the value of $f(\mathbf{x}_r)$. First is that it the best value found so far, and so the simplex should be expanded along the centroid-reflected vertex axis

$$(3.22) \quad \mathbf{x}_e = \mathbf{x}_0 + \gamma(\mathbf{x}_r - \mathbf{x}_0).$$

- . The corresponding vertex of the two function values $f(\mathbf{x}_r), f(\mathbf{x}_e)$ then replaces the "worst" vertex \mathbf{x}_{n+1} .

A second possibility is that the function value for the reflected vertex is better than the worst vertex used to calculate the centroid, but worse than the best value, $f(\mathbf{x}_1) \leq f(\mathbf{x}_r) \leq f(\mathbf{x}_n)$. In this case the \mathbf{x}_{n+1} vertex is replaced by the reflected vertex.

The last possibility is that the reflected vertex has a greater function value than any vertex used to calculate the centroid. In this case a new point (contraction), or set of points (shrink) are used to propagate the simplex. Depending on whether this function value is greater or less than the worst vertex in the simplex (\mathbf{x}_{n+1}), the contracted point is either inside or outside of the simplex

$$(3.23) \quad f(\mathbf{x}) = \begin{cases} \mathbf{x}_c = \mathbf{x}_0 + \rho(\mathbf{x}_r - \mathbf{x}_0) & \text{if } f(\mathbf{x}_r) < f(\mathbf{x}_{n+1}) \\ \mathbf{x}_c = \mathbf{x}_0 + \rho(\mathbf{x}_{n+1} - \mathbf{x}_0) & \text{otherwise } f(\mathbf{x}_r) \geq f(\mathbf{x}_{n+1}) \end{cases}$$

if the contracted point \mathbf{x}_c is give a smaller function value than the reflected point for the first case, or the worst point for the second case, it then replaces the worst simplex vertex.

The final possibility is that both the contracted point function value is greater than either the reflected point or the worst point. In this case, the entire simplex is shrunk around axes to the best vertex

$$(3.24) \quad \mathbf{x}_i = \mathbf{x}_1 + \sigma(\mathbf{x}_i - \mathbf{x}_1)$$

for $i \in \{1, \dots, n\}$.

Once either the worst vertex or all of the vertices are replaced, the new simplex is used as the start of a further iteration. Iterations are stopped once a termination criteria is met, such as a vertex function value being below a threshold.

Several versions of this method exist, that add additional constraints. This can include keeping the volume of the simplex constant, which can promote a steepest descent approach.

3.2.2.2 Sequential Least-Squares Quadratic Programming

The SLSQP (Sequential Least-Squares Quadratic Programming) method is fundamentally different to the previous Nelder-Mead method, and follows a quasi-Newton procedure with additional factors to treat constraints.

The general problem is similar to Nelder-Mead, namely to solve

$$(3.25) \quad \min_{\mathbf{x} \in \mathbb{R}^n} f(\mathbf{x})$$

however with an arbitrary amount of constraint functions c

$$(3.26) \quad c_i(\mathbf{x}) = 0$$

$$(3.27) \quad c_j(\mathbf{x}) \leq 0$$

where i, j are indices of the constraint functions. It is assumed that the space of f and c_n are one-to-one mappable on the space of x , and also is continuously differentiable. Starting from an initial value of \mathbf{x}_0 , a search direction d^k and step length α_k are used to propagate the set of parameters by

$$(3.28) \quad \mathbf{x}_{k+1} = \mathbf{x}_k + \alpha_k \mathbf{d}_k$$

. The search direction, analogous to the ratio of function value to gradient in the Newton-Raphson method, is calculated by solving the Lagrange function

$$(3.29) \quad \mathcal{L}(\mathbf{x}, \lambda) = f(\mathbf{x}) - \sum_n^m \lambda_n g_n(\mathbf{x})$$

with a quadratic approximation, that reduces the problem to a quadratic programming subproblem

$$(3.30) \quad \min_d f(\mathbf{x}_k) + \nabla f(\mathbf{x}_k)^T d + \frac{1}{2} d^T \nabla_{xx}^2 \mathcal{L}(\mathbf{x}_k, \lambda_k) d$$

where the last term is often short-handed as the **B** matrix. This is the sequential quadratic programming method. A linear least squares subproblem could be used instead of quadratic programming, which would give the subproblem as

$$(3.31) \quad \min_d \|(\mathbf{D}_k)^{\frac{1}{2}} (\mathbf{L}_k)^T d + (\mathbf{D}_k)^{-\frac{1}{2}} (\mathbf{L}_k)^{-1} \nabla f(\mathbf{x}_k)\|$$

where the matrices **L**, **D** are from a diagonal decomposition of **B**

$$(3.32) \quad \mathbf{L}_k \mathbf{D}_k (\mathbf{L}_k)^T = \mathbf{B}_k$$

. With the solutions for \mathbf{d}_k solved by these subproblems, the parameter vector \mathbf{x} can be propagated until similar termination criteria as the Nelder-Mead method.

A visualisation finding a parameter set \mathbf{x} corresponding to a local minimum of the Himmelblau function (a standard benchmark for optimisation algorithms) is shown in figures 3.4 and 3.5. The former shows the Nelder-Mead simplex vertices, with the latter showing iterations in the \mathbf{x} space. It can be seen that the Nelder-Mead algorithm evaluates more points and covers a broader space, whereas the SLSQP algorithm follows a more direct gradient descent.

Both these methods were used to find optimal chl-xTB parameters, and it was found that the SLSQP method performed best, both in terms of the number of iterations, stability, and in the

overall value of the objective function. This could be due to the addition of constraints, however it is hard to say as the wrapping of SciPy around the implementations of both methods make it a black-box that is hard to investigate further. The results of the optimisation is discussed in further detail in section 3.2.4.

3.2.3 Reference Data

The geometries for the training set used to optimise the chl-xTB method were taken from previously done molecular dynamics of the LHII protein [29]. The geometries of LHII were chosen from uncorrelated snapshots, although each of the 27 chlorophylls from each snapshot were included in the training data to account for the differences in binding pockets. The stochastic collection of LHII snapshots were chosen to cover a range of chlorophyll conformations to reduce the amount of artificial bias towards any particular geometries.

Training the chl-xTB parameters was done against PBE0 data. This data was chosen for the best accuracy-cost ratio, as well as having been previously used to investigate exciton properties for the LHII system [29]. Additionally, from the outset it was unknown how much training data would be necessary, and so keeping potential future costs of expanding the training data down was another factor in choosing this functional.

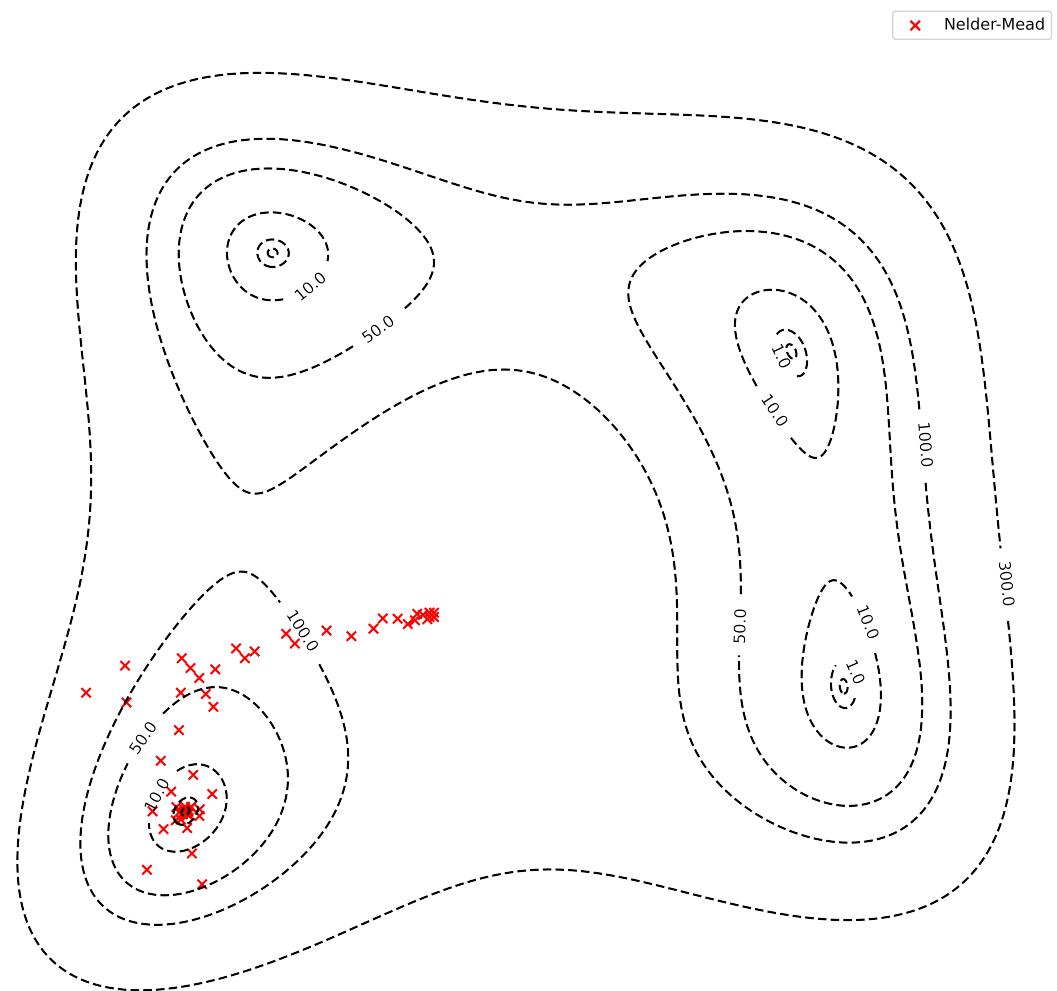


Figure 3.4: Positions of the Nelder-Mead simplex vertices for the HimmelBlau function.

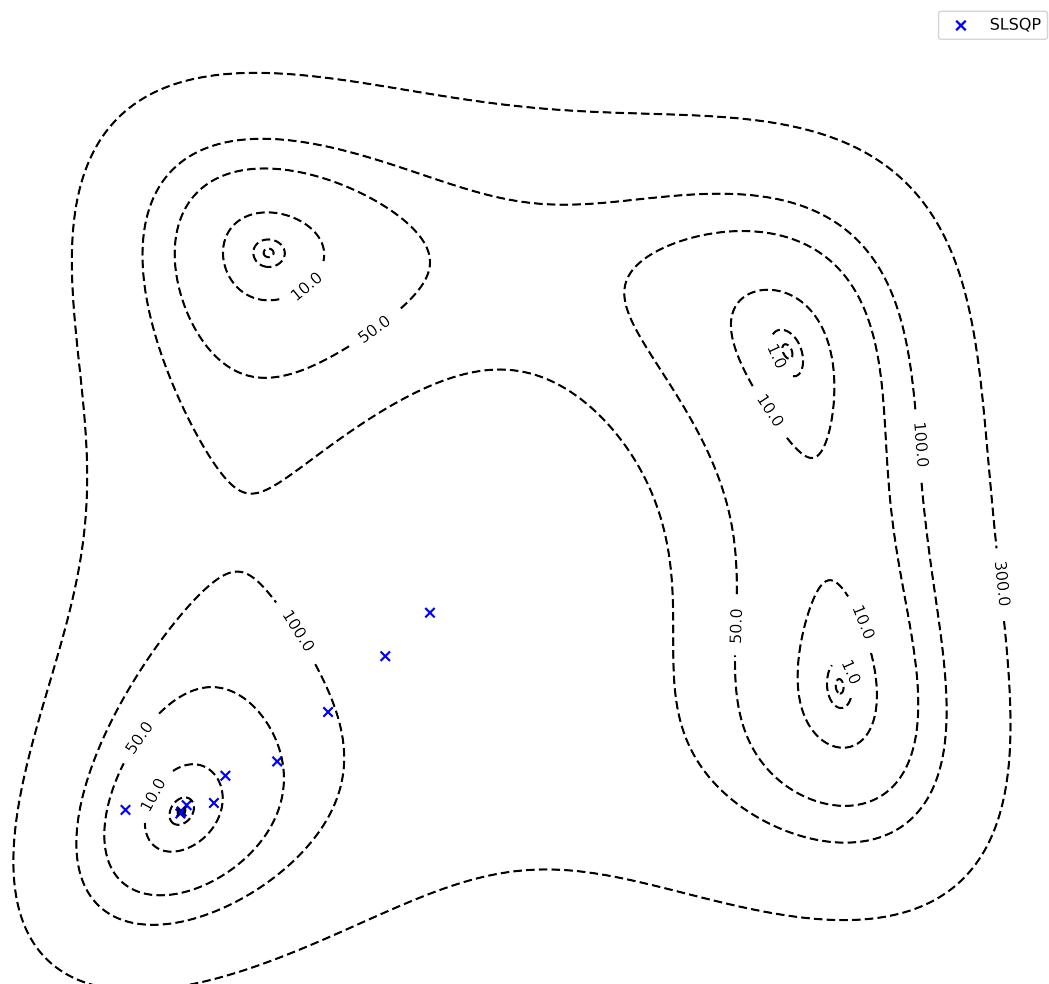


Figure 3.5: Positions of iterative solution vector \mathbf{x} from SLSQP for the HimmelBlau function.

	RMSE(ΔE)	$R^2(\Delta E)$	RMSE(μ)	$R^2(\mu)$
CAM-B3LYP	0.147	0.795	0.172	0.919
ω -B97XD	0.200	0.650	0.214	0.876
BLYP	0.053	0.871	0.384	0.129
Δ -SCF	0.225	0.847	1.455	0.566
$\Delta\epsilon$	0.218	0.875	1.511	0.500
ZINDO	0.596	0.339	1.526	0.396

Table 3.1: ref data vals

Transition properties were calculated with a range of methods, covering levels of theory that would be comparable to the chl-xTB formalism. These included an eigenvalue difference approach, Δ -SCF, and TD-DFT with different levels of theory. This was done so that the performance of any parameterisation results could be benchmarked to an expected accuracy.

The errors and correlations of the reference data are shown in table 3.1. The methods included in the benchmarking were Δ -SCF, TD-DFT and eigenvalue difference all using the PBE0 functional and Def2-SVP basis set. Also included are CAM-B3LYP and BLYP functionals with Def2-SVP basis sets, as a higher and lower level reference respectively. The basis set was not changed as it has been found that the basis set has less importance on the accuracy than the functional [29].

There is a large variation in correlation and RMSE values for the reference methods to PBE0. This variation sets a reasonable expectation of how well a new method might perform. The BLYP functional performs best with an RMSE of 0.053 eV, and is most correlated (of the TD-DFT methods) with an R^2 value of 0.871. Second best is CAM-B3LYP, with an RMSE of 0.147 eV. ω -B97XD performs relatively well, with an RMSE value of 0.200 eV, but has the lowest R^2 value of 0.650. This illustrates how a low RMSE and high correlation are not mutually inclusive, and so must both be present in the objective function. The variance in these different TD-DFT methods, all of which have been used in studies on chlorophyll, show how it is difficult to assign a true value to transition energy for a set of geometries. Therefore as long as the accuracy of chl-xTB is within the range of methods shown here, it would also be valid.

The single transition methods also perform well, corroborating the earlier statement that only treating a HOMO-LUMO transition can give accurate results. The Δ -SCF and eigenvalue difference methods have slightly higher RMSE values, both around 0.22 eV. However the correlation is much higher at 0.847 and 0.875 a.u. respectively. Hence, due to the dominance of HOMO-LUMO transition character, treating the transition as mixed is not necessary in order to achieve accuracy for transition energies. The story for transition dipoles, however, is different.

The agreement of transition dipole magnitudes is much lower than excitation energies. The RMSE of Δ -SCF and eigenvalue difference methods is significantly higher (1.455 a.u. and 1.511 a.u. respectively) than the TD-DFT methods (0.172 a.u., 0.214 a.u. and 0.384 a.u. for CAM-B3LYP, ω -B97XD and BLYP respectively). The average magnitude of PBE0 transition dipoles is 2.751 a.u.,

with the average for Δ -SCF and eigenvalue difference being 4.287 a.u. and 4.342 a.u. respectively. This disparity is attributed to the lack of inclusion of Q_x transition character. As this dipole component of this transition is orthogonal to Q_y , it may reduce the transition dipole magnitude similar to the effect seen in the outliers in the previous chapter.

Whilst there is a high degree of correlation between the higher level TD-DFT methods, with 0.919 and 0.876 for CAM-B3LYP and ω -B97XD respectively, the other methods have a much lower correlation to PBE0 transition dipoles. BLYP is the worst correlated, with a R^2 value of 0.129, which is fully uncorrelated. Δ -SCF and eigenvalue difference show a slight correlation at around 0.5.

Also included in the benchmarking was the semi-emperical method ZINDO. This had a poor accuracy across the board, with RMSE and R^2 values of 0.596 eV and 0.339 for transition energies, and 1.526 a.u. and 0.396 for transition dipoles. It was thought this might have good accuracy compared to TD-DFT and serve as a benchmark for how well a semi-emperical method might perform, but this turned out to not be the case.

Overall an RMSE to transition energies and dipoles of 0.15 eV and 0.2 a.u. is necessary to claim that transition properties can be calculated on a usable level of accuracy. Other cross-validations are necessary, and will be discussed in section 3.3, but for the optimisation this provides a benchmark to aim for. Whilst a high correlation of around 0.8 for both transition energies and transition dipoles is possible, it can be seen that the latter may not be possible for a single transition method.

3.2.3.1 Training and testing set

From the full set of PBE0 data, 100 random geometries were chosen for the training set and 507 geometries for the test set. The test set was used at the end of the optimisation procedure to validate how well the parameters perform on points outside of the training data. The sizes of each set was chosen to achieve a subset mean error (how far the mean of the subset is from the full set of data) below 0.15 eV for transition energies, whilst keeping a large number of geometries for the testing set, as these are mutually exclusive.

Hamiltonian			
k_s	1.462	1.850	
k_p	2.694	2.250	
Mg_p	0.902	-	
Mg_s	1.053	-	
N_p	1.044	-	
N_s	1.281	-	
$Mg_s\text{-}N_s$	1.468	-	
$Mg_s\text{-}N_p$	1.023	-	
$Mg_p\text{-}N_s$	1.067	-	
$Mg_p\text{-}N_p$	1.402	-	
Response			
y_K	2.147	2.000	
y_J	4.012	4.000	
a_x	0.067	0.500	
D_{scale}	0.636	-	

Table 3.2: optimized parameters from SLSQP procedure.

3.2.4 Results

Overall, the method performs extremely well considering the limitations as set out above. Transition energies and dipole magnitudes are calculated well within acceptable RMSE and correlation limits.

The final parameters for the chl-xTB method are given in table 3.2. The best performing set of parameters had an RMSE of excitation energy of 0.014 eV with an R^2 value of 0.88, and an RMSE of transition dipole magnitude of 0.057 a.u. with an R^2 value of 0.40. Repeated optimisation runs gave parameter and objective function minima to similar values, and the difference in these values can be attributed to the complex solution space. These values for RMSE are well within the values for TD-DFT with various functionals, and the R^2 of transition energy is equally good. While the correlation is low, it is near to the expected correlation from Δ -SCF and eigenvalue difference. It can also be seen in figure 3.2.4 that the variation in chl-xTB transition dipole magnitude is much smaller than Δ -SCF, eigenvalue difference and ZINDO, as well as being close to the mean from PBE0. This is a better behaviour, similar to the statiscal method used before [29], than the other methods with low correlations.

It was also found that lower minima of the objective function were found when using the SLSQP method for optimisation instead of the default Nelder-Mead method. Minima were found in a smaller number of iterations, reducing the overall CPU time required. This is in line with benchmarked SLSQP solutions in a non-linear multidimensional space. It was also investigated whether a reduction in the amount of parameters was possible, by only training the response parameters and not the Hamiltonian parameters, however this did not achieve the same levels of accuracy as using both sets of parameters.

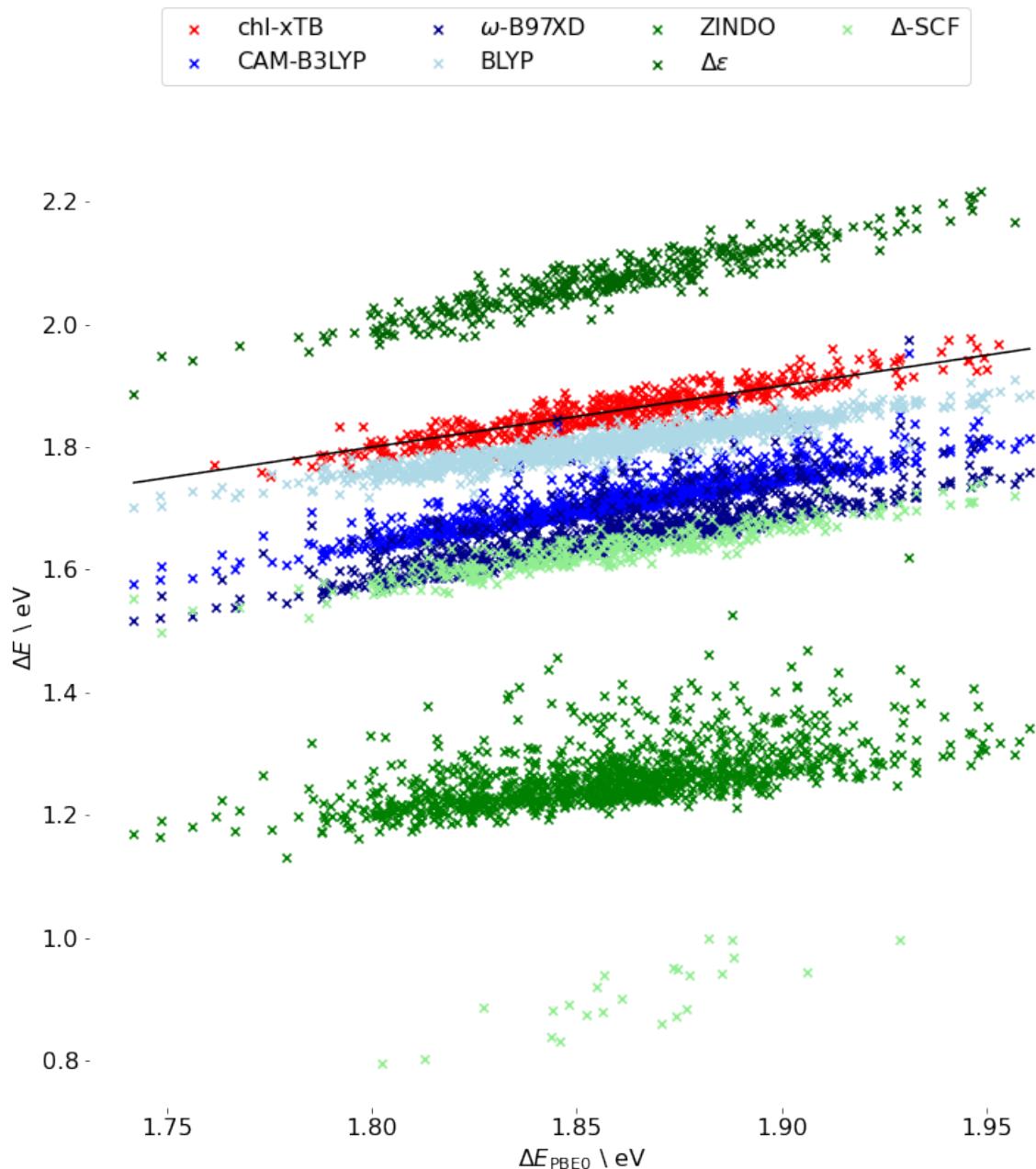


Figure 3.6: caption

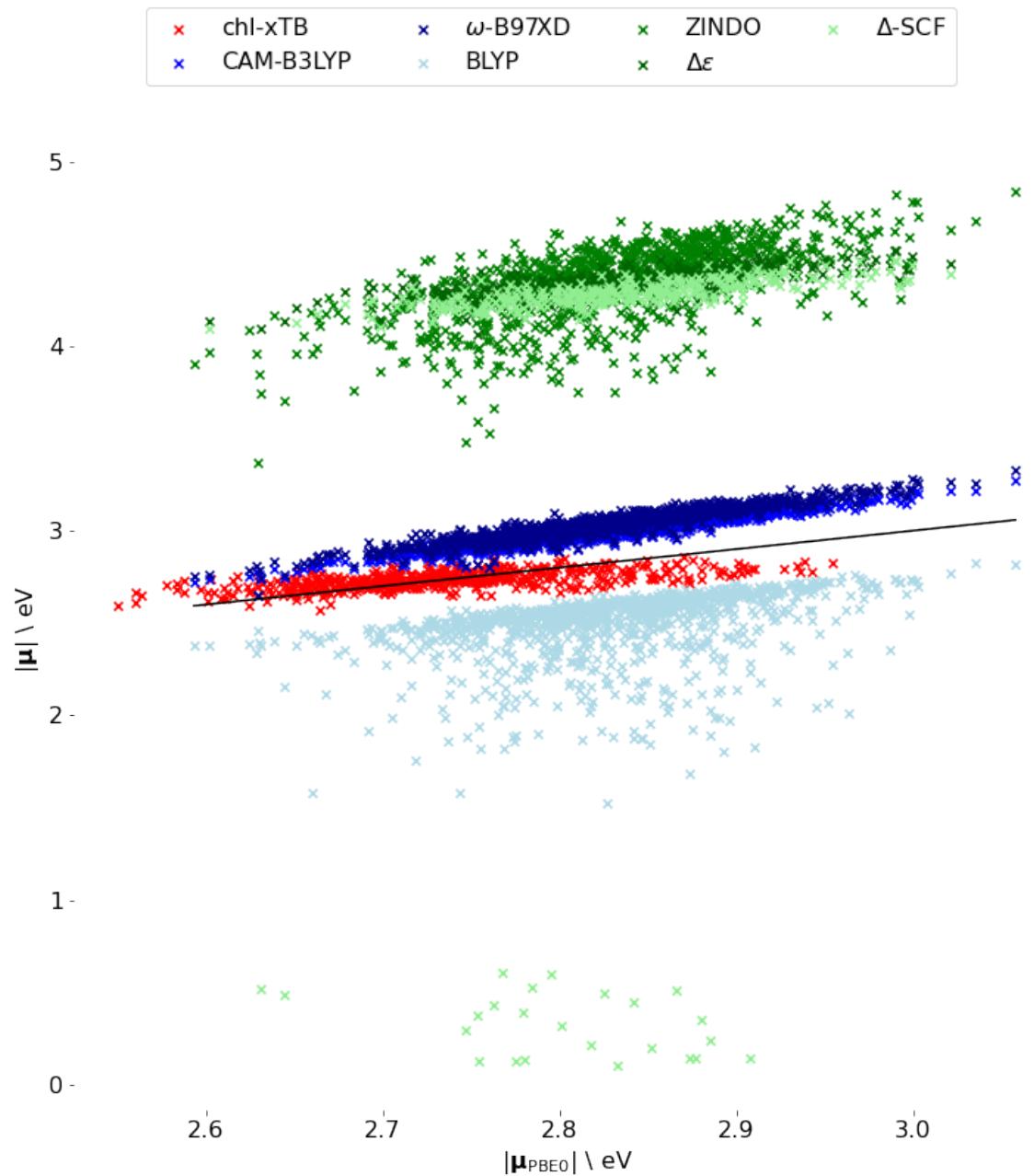


Figure 3.7: caption

The initial guess for parameters were the corresponding GFN1-xTB and sTDA-xTB parameters, or 1.0 for new parameters such as the Mg, N and transition density matrix scaling.

The optimised values do not differ much from the original GFN1-xTB and sTDA-xTB parameters (given for reference in table 3.2), with the exception of the a_x parameter. This parameter is far lower than the sTDA-xTB equivalent, which has a value of 0.500, but is in line with other methods that use similar MNOK approximations for coulomb-type integrals in response methods [5].

3.3 Cross-validation

3.3.1 Vibrational Mode Coupling

Whilst the stochastic selection of BChla geometries should represent a large section of the conformational space in LHII, it is not explicitly given that chl-xTB would perform equally well along important vibrational modes. Explicitly testing the values predicted by PBE0 and some of the reference methods as well as optimised chl-xTB would show how well the geometry dependence has been "learnt". These values would correspond to geometries that vary by a single normal mode displacement at a time to reduce error cancellation, as well as to show how well chl-xTB predicts to the coupling of vibrational modes and transition properties.

The geometries for this test were not taken to be BChla for two reasons. There are 140 atoms in BChla, giving the number of normal modes is 414, and with 10 coordinates being calculated along each normal mode this represents a large number of geometries that would require reference data with expensive functionals and basis sets. Additionally, the normal modes would need to be calculated from an optimised geometry. The phytol tail in BChla (and chlorophyll in general) make geometry optimisations difficult due to the large degrees of freedom in rotations along the carbon chain. Without an accurately optimised geometry for the normal mode hessian, the predicted displacement vectors for the normal modes would be useless.

Therefore the normal modes and transition properties were calculated for a truncated BChla with a hydrogen atom replacing the phytol tail, which made geometry optimisation possible, and also reduced the total number of vibrational modes.

Normal modes with the strongest coupling to the Q_y transition were chosen to most effectively scan the conformational space. These can be found by looking at modes which break the symmetry of the Q_y transition. In an ideal model, the magnesium and nitrogen centre have D_{4h} symmetry with the Q_y transition lying along the N_A, N_C axis. Vibrational modes with components along this axis will therefore couple to the transition. The movement of N_A, N_C atoms which induce $D_{4h}-D_{2h}$ and $D_{4h}-C_s$ symmetry breaking are shown in figure 3.8.

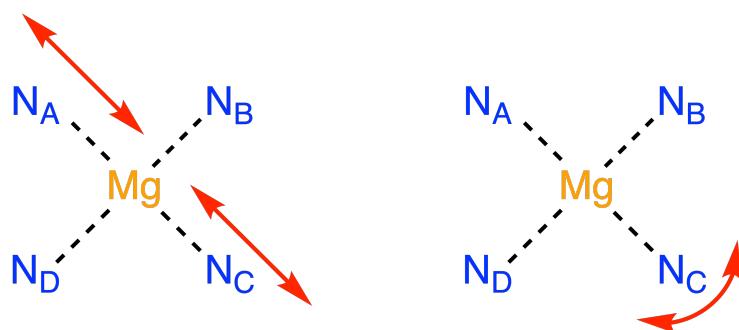


Figure 3.8: Normal modes of the nitrogen-magnesium centre of chlorophyll that have $D_{4h}-D_{2h}$ (left) and $D_{4h}-C_s$ (right) symmetry breaking components.

Normal modes that would also have this symmetry breaking component were indentified by how much the N_A - N_C displacement would change along each normal mode. A plot of these values, as well as the moving average, is shown in figure ???. A similar scan was made of the N_A - Mg - N_C angle, however less variance in this value was found and the peak positions did not match previously reported frequencies for strong coupling. Normal modes with the largest N_A - N_C were then chosen for the transition properties scan. It is interesting to note that the peaks in the moving average line approximate the peaks in the chlorophyll *a* absorption spectrum. The normal modes that were chosen had frequencies at 669.6, 701.7, 733.3, 745.5, 755.1, 1105.0, 1107.0, 1122.2, 1142.9, 1320.3, 1361.8 cm⁻¹, which roughly correspond to previously indentified normal modes with frequencies of 728 and 1156 cm⁻¹ [18].

For each selected normal mode, the geometry was propagated such that the sum of all atomic displacements from the optimised geometry was in units of 1 Å. This was done up to 3 Å as it was found for most normal modes the energy difference between the optimised geometry and 3 Å displaced geometry was greater than the thermal energy at 300 K. At each increment, the Q_y transntion energy and dipole was calculated using chl-xTB, as well as TD-DFT with a PBE0/Def2-SVP level of theory. Additionally, Δ -SCF and the eigenvalue difference method was used as a benchmark, along with CAM-B3LYP TD-DFT with the same basis set. A quadratic fit was also made for each of the methods and is shown in the plots. Some points for the Δ -SCF method are not shown as convergence for the excited state at these geometries were not possible for similar reasons discussed in the previous chapter.

It can be seen that chl-xTB predicts PBE0 transition energies with a high degree of accuracy. Transition dipole magnitudes are predicted with less good accuracy, but still capture the main behaviour of PBE0 results well. chl-xTB consistently predicts PBE0 energies to within the same level of accuracy as achieved in the parameterisation test set. From the quadratic fits it can be seen that the gradients, turning points and curvature is well alligned between PBE0 and chl-xTB, especially compared to Δ -SCF and eigenvalue difference. It is also clear how important the transition density scaling factor is in achieving accuracy for the transtion dipole magnitudes, with Δ -SCF and eigenvalue difference being well above where PBE0 and CAM-B3LYP values sit.

It is argued that variations in chl-xTB transition properties, in addition to correctly correlated with geometry variations, are also correctly correlated to the coupling between normal modes and the Q_y transition. This is an important consideration for the later chapter on spectral density, where the assignment of spectral features are based on comparison to vibrational modes.

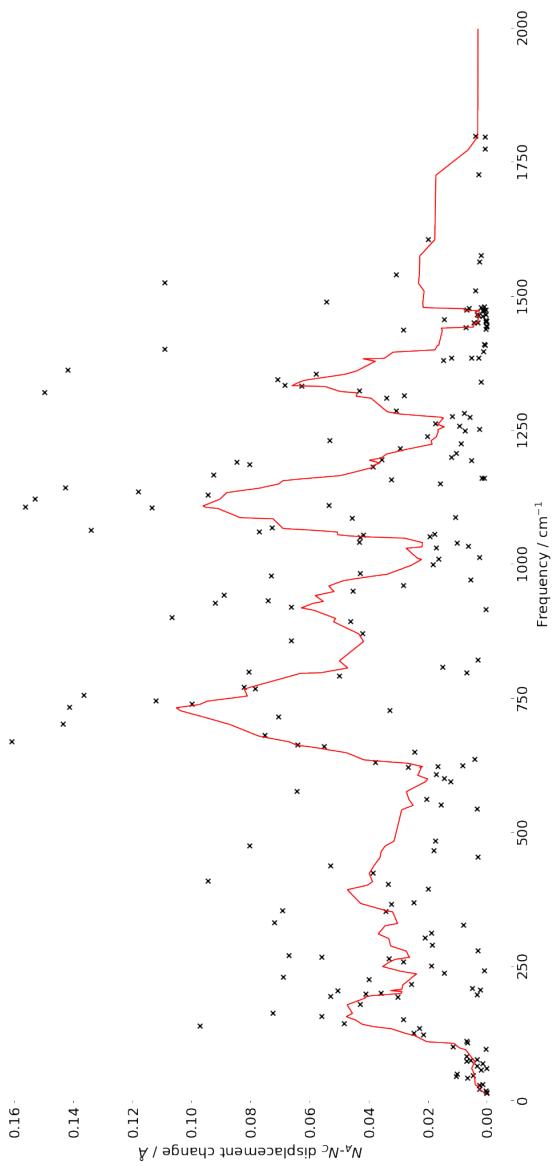


Figure 3.9: Change in the N_A - N_C displacements along the set of GFN1-xTB normal modes for a chlorophyll molecule truncated at the phytol tail.

3.3. CROSS-VALIDATION

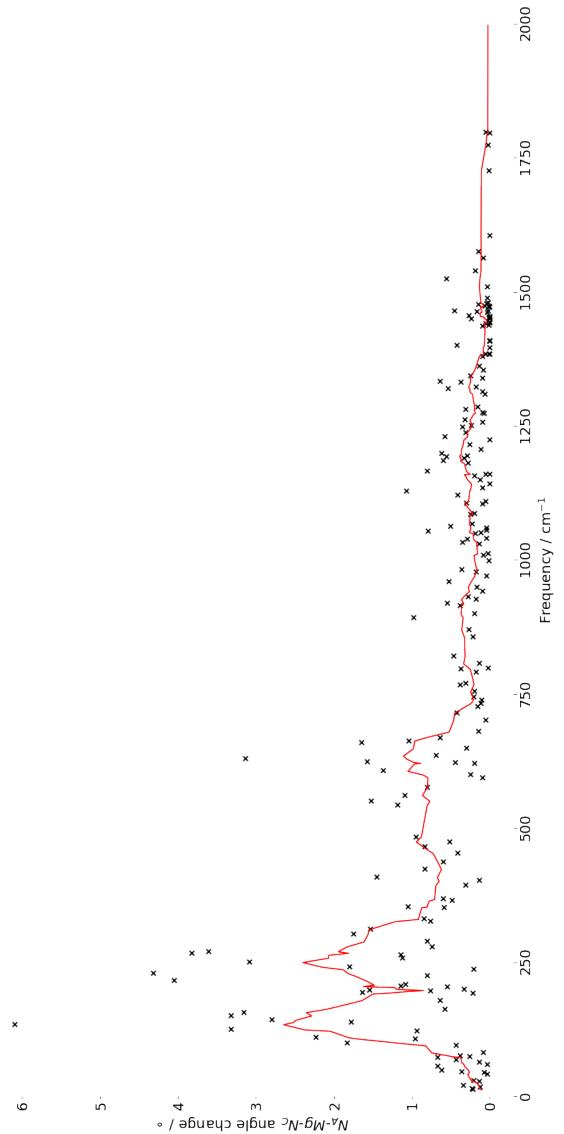
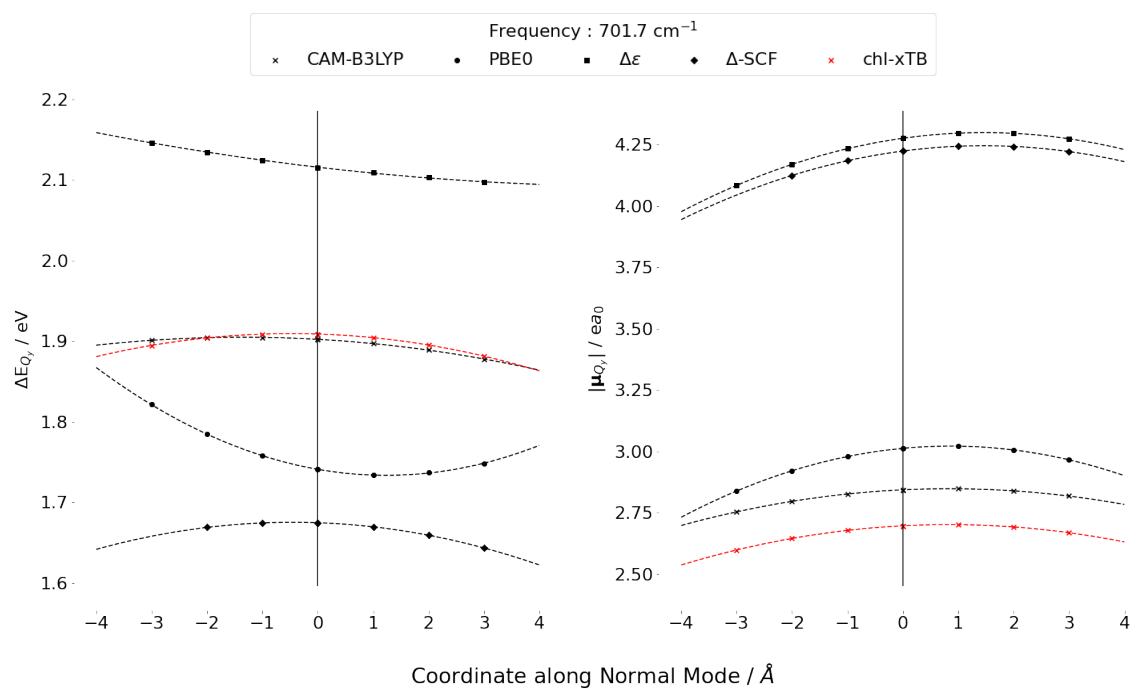
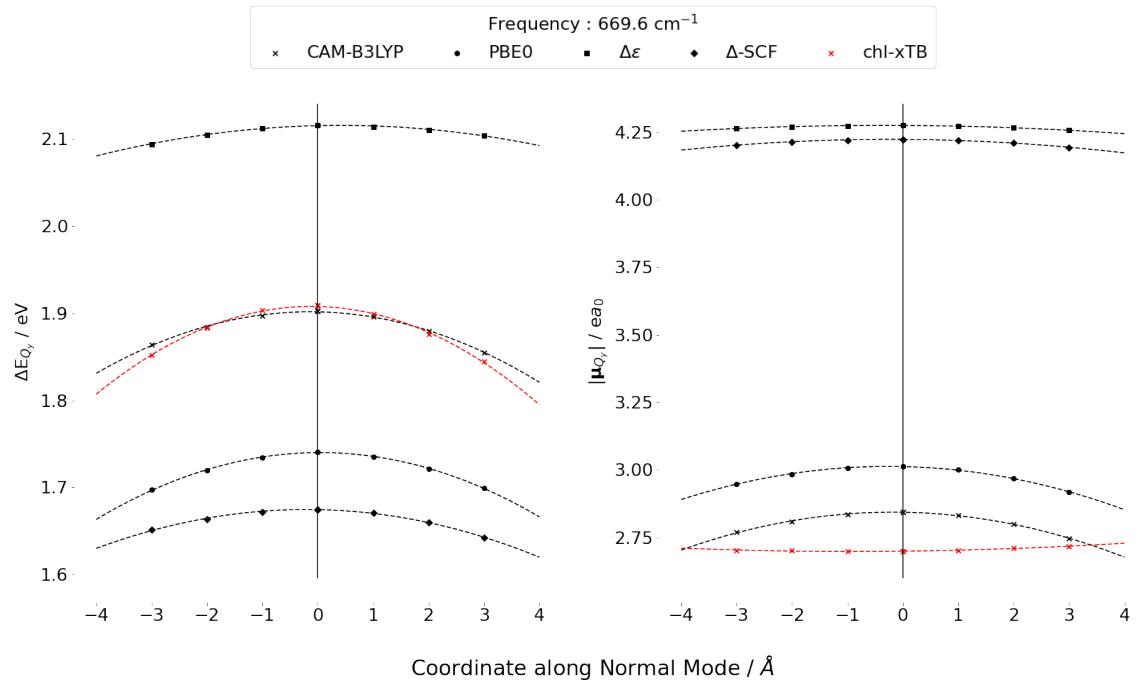
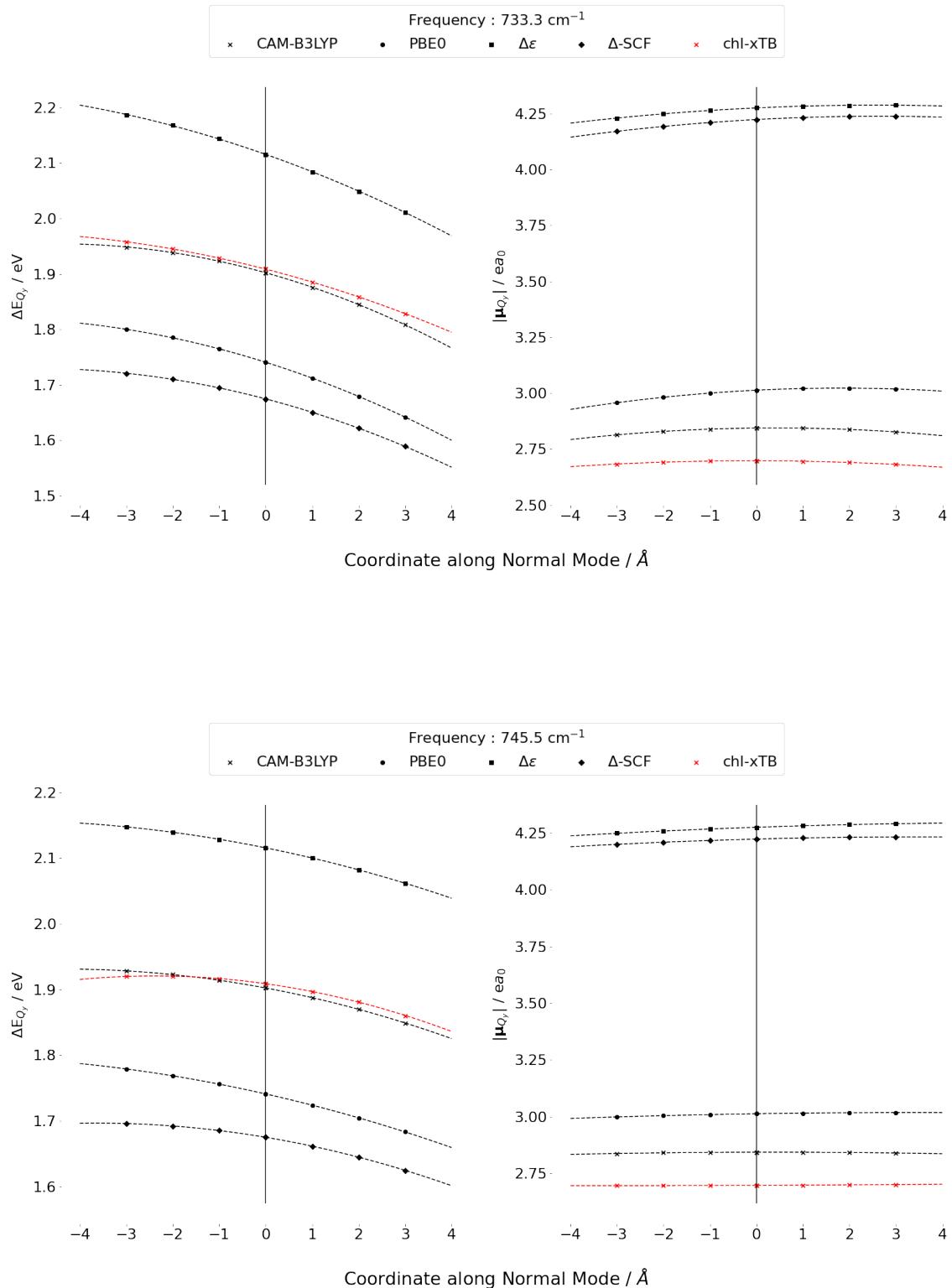
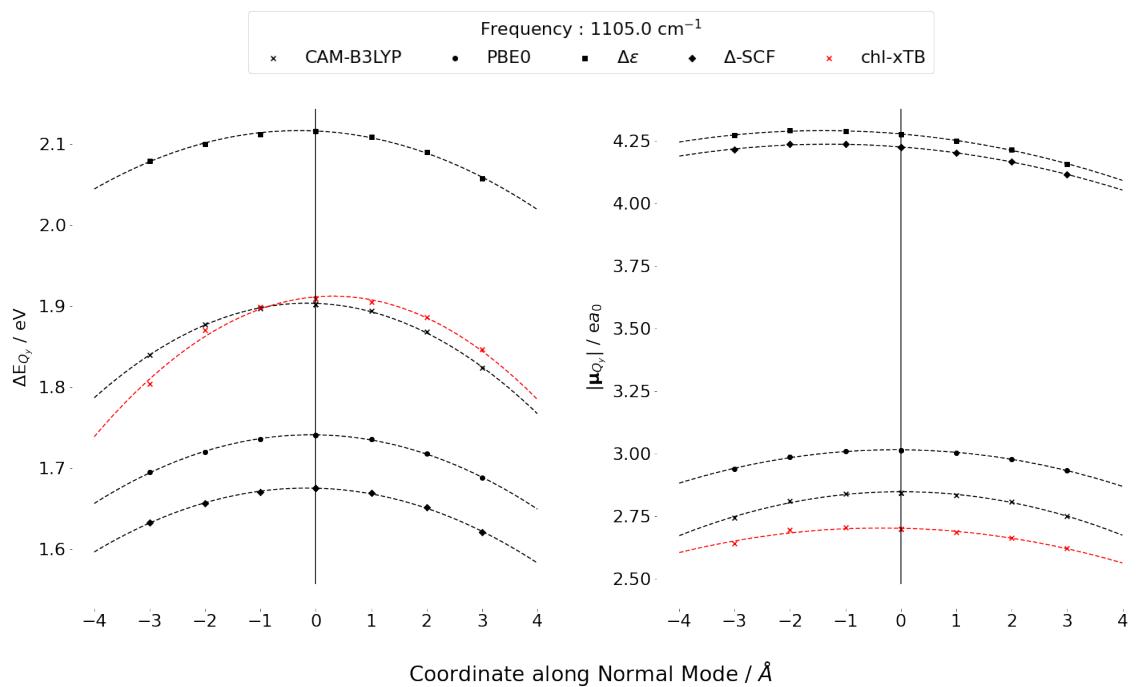
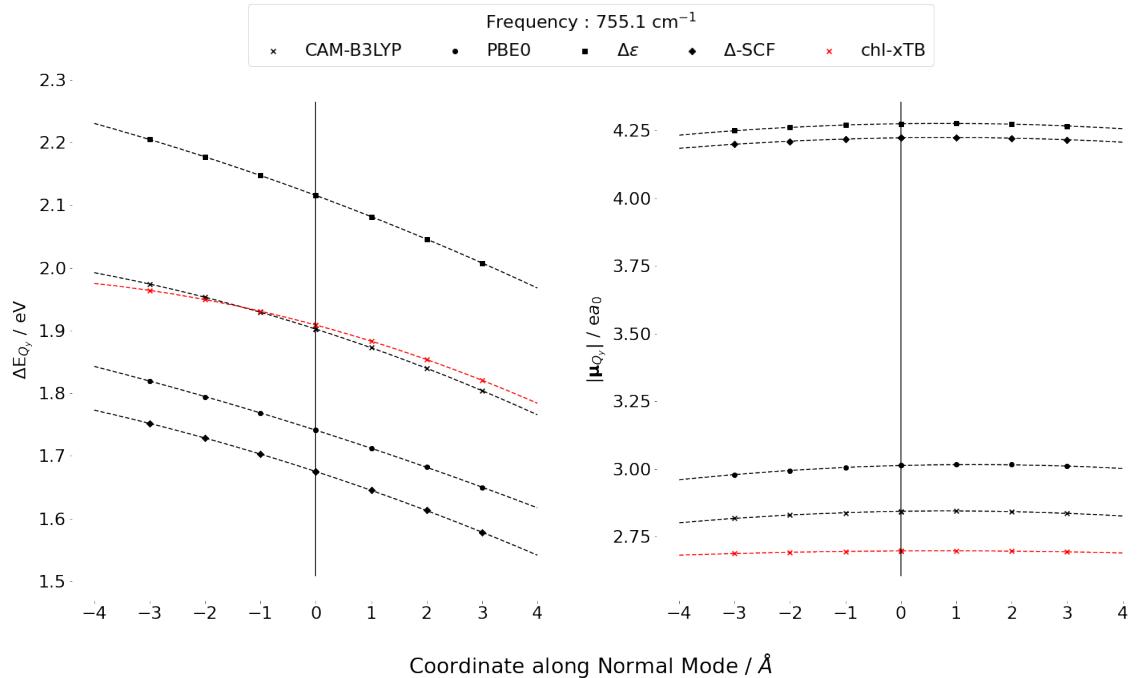


Figure 3.10: Change in the N_A -Mg- N_C angle along the set of GFN1-xTB normal modes for a chlorophyll molecule truncated at the phytol tail. The small smaller variance than in figure 3.3.1 led to this metric to not be used in normal mode choices.

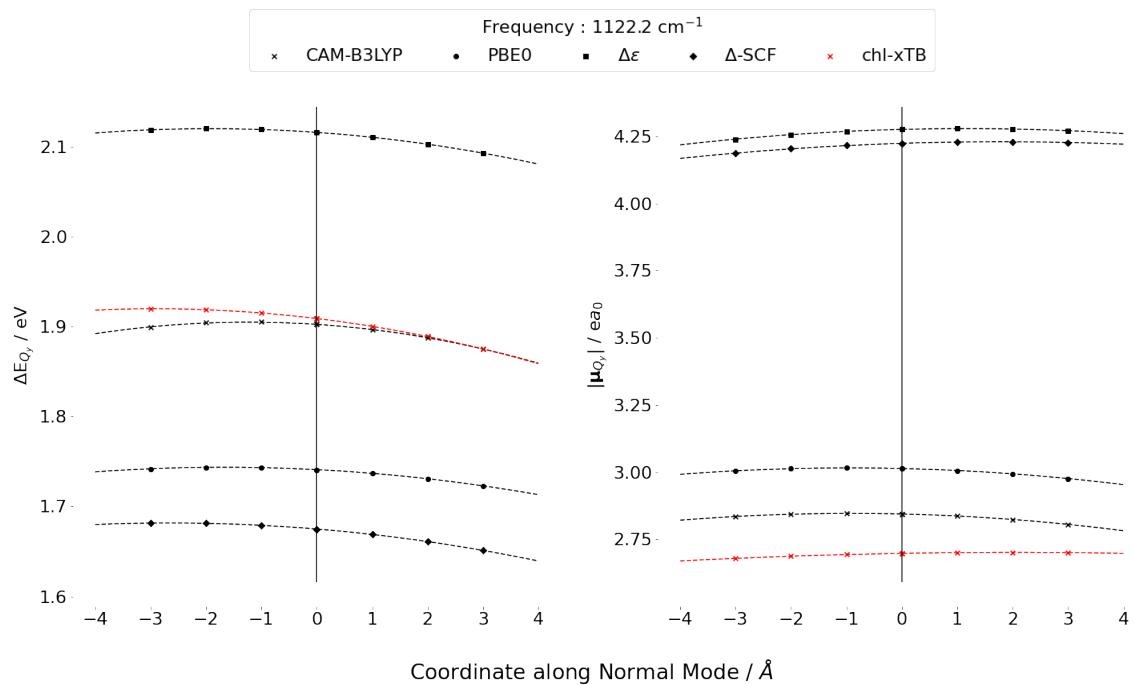
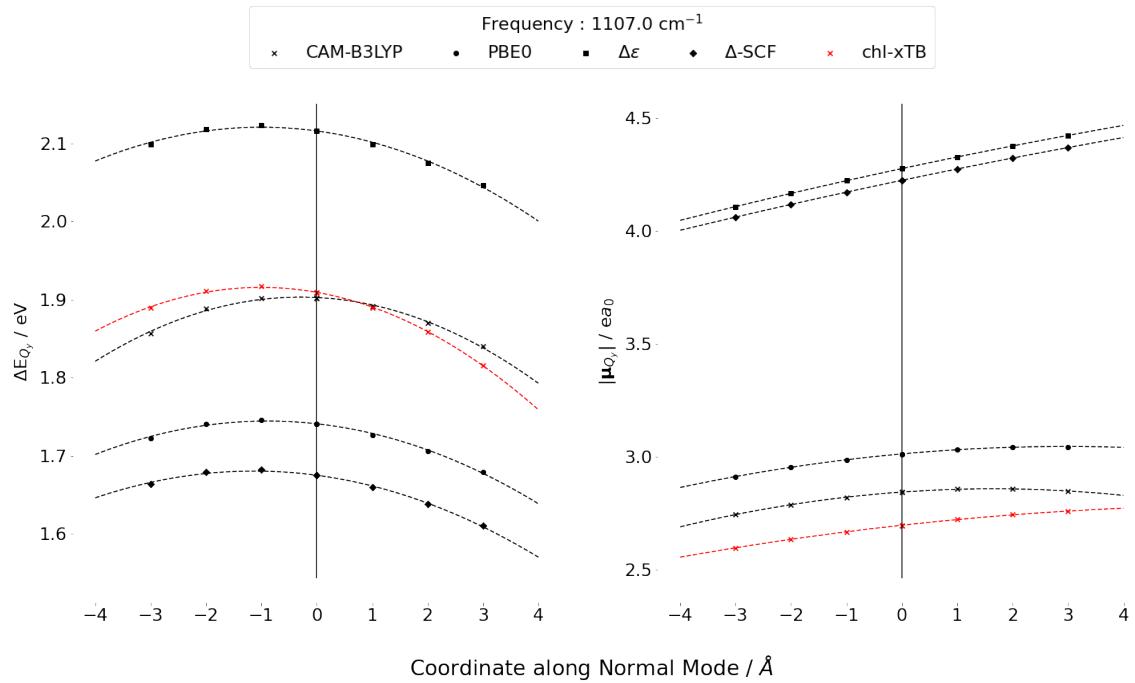


3.3. CROSS-VALIDATION





3.3. CROSS-VALIDATION



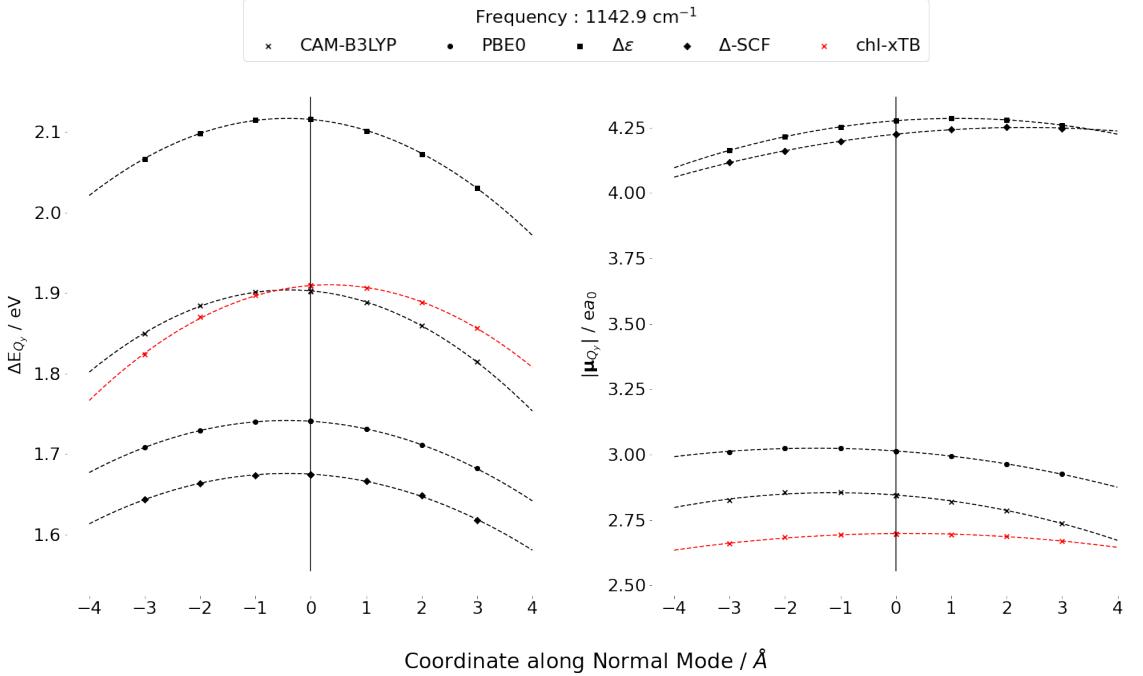


Figure 3.11: Transition energies and dipole magnitudes for the Q_y transition for geometries of truncated chlorophyll along normal modes, calculated with different response theories.

3.3.2 Absorption Spectra

So far all of the benchmark and tests on chl-xTB have been for gas phase systems and have no environmental effects. However in reality chlorophyll molecules would be embedded in many different environments, for example the LHII protein. Although the training set took structures that have been perturbed by the LHII protein, it is important to test the behaviour of properties predicted by chl-xTB when explicitly embedded. The obvious case for this would be predicting an absorption spectra for chlorophyll when embedded by an explicit solvent. Additionally, it should be tested whether the method could work for other chlorophyll systems other than Bchl_a. This would be important for future investigations into chlorophyll systems, but for the remaining work here it is not as important, and so isn't investigated fully.

The absorption spectra was calculated using frames from an MD trajectory of chlorophyll A in an explicit diethyl ether solvent. An explicit solvent was used to account for inhomogeneous broadening in the spectrum. The MD was performed with the OpenMM toolkit. Forcefield parameters for the chlorophyll were taken from a bespoke parameterisation for photosystem II [31], with the rest of the system using the OpenForceField. The structure for chlorophyll was taken from the same source as the bespoke forcefield, and packed with explicit solvent using the tools in the Mistral package. Equilibration and production steps were done with a Langevin integrator set to 300 K and a timestep of 0.5 femtoseconds. The system energy was minimised before running a

10ps equilibration. Frames were then taken from a 2ns simulation time, with structures taken every picosecond.

Transition properties for chlorophyll structures from every frame were calculated. This was done with the chl-xTB method, as well as PBE0 and CAM-B3LYP TD-DFT, both using the Def2-SVP basis set. For the TD-DFT methods, the lowest excited state, rather than always the Q_y state, was taken for each frame, so as to fully capture the Q band. Experimental data for the absorption spectra was also taken from Katz *et. al* [28]. Embedding effects were included in the chl-xTB Fock matrix with a particle mesh Ewald method. The real space term was calculated using QCORE, whereas the more complicated spline reciprocal space term was calculated with the HelpME library. The absorption spectrum for each method was calculated by a gaussian fit of a histogram of transition energies. The fit was normalised such that the area under all spectra matched that of the experimental spectrum. The absorption spectra, both with and without a single-parameter shift of excitation energies, can be seen in 3.12.

chl-xTB performs equally well as TD-DFT methods at simulating absorption spectra, although constrained by the limits of the method and the training data. It can be seen that the chl-xTB lineshape is similar in position and width to the PBE0 method. This is highly encouraging, as the functional groups on chlorophyll A can have a large effect on the Q_y transition, and so the good agreement here provides evidence that important chemical features are still captured in different systems. Although the chl-xTB lineshape is wider than the experimental spectrum, the CAM-B3LYP and PBE0 lines are also wider and so the chl-xTB is still within a reasonable expectation of accuracy. Also seen is the lack of other peaks from the Q band, which is present in the experimental spectrum. The CAM-B3LYP data shows one peak at 510 nm, with PBE0 having a very slight peak at around 380 nm. This is not present in the chl-xTB spectrum as other Q transitions are not calculated due to being outside of the training data. The embedded chl-xTB spectra is both red-shifted and broadened slightly, which is also observed in simulated spectra from other methods.

3.4 Conclusions

It has been shown that novel approximations to the full linear-response eigenvalue equation can give accurate predictions of transition properties from high-level methods. This has been shown by optimising a set of parameters for the response approximations, as well as for the underlying electronic structure.

Overall, chl-xTB performs as well as can be expected from the training data. Predictions of transition energies and transition dipoles are incredibly close to the PBE0 values, and well within the error between different high level DFT functionals. The variations of these transition properties can be attributed to geometry variations rather than random error.

From this it could be expected that improvements in the training data would yield better

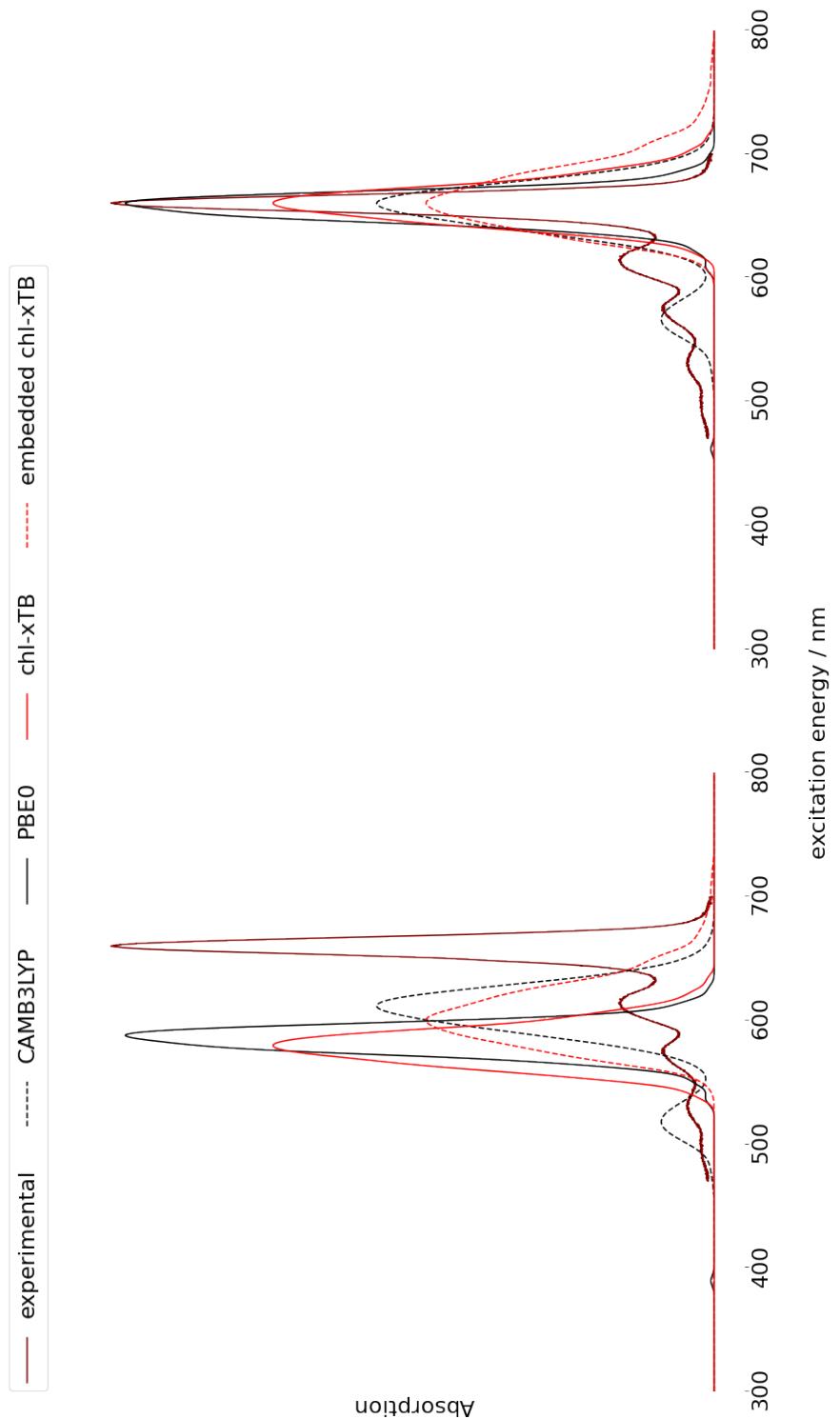


Figure 3.12: Chlorophyll in diethyl ether.

3.4. CONCLUSIONS

accuracy. This might be done by extending the training data in either the conformational space, or by investigating other systems.

This was taken into consideration when investigating this method, for example using CAM-B3LYP as training data instead of PBE0. This approach would have two drawbacks. First would be that PBE0 has already been established for investigating LHII properties, and so a clearer comparison of results for the exciton system would be possible. Second is that a feature of this method is the reduced amount of computational cost required. If the amount of CAM-B3LYP data that may have been necessary to obtain increased too much then it would no longer be efficient to parameterise compared to using a different, lower level method. For other systems smaller than chlorophyll, this might not be the case.

BEYOND MONOMER CHLOROPHYLL

This chapter investigates the applicability of chl-xTB for aggregate chlorophyll systems, beyond the monomers reported in the previous chapter. It is the properties of aggregate chlorophyll that make light harvesting systems so efficient. It is necessary to show that chl-xTB can be used to construct viable models for these systems.

4.1 Theory

4.1.1 Exciton States

As stated in the introduction, a large majority of models of light harvesting systems utilises a Frenkel Hamiltonian model of excitonic states, where the weak coupling between monomers mean that a description can be constructed from properties of the individual sites.

To recap the exciton theory from the introduction, the exciton states $|\Psi\rangle$ can be constructed as a Hartree product of the states of individual sites (also referred to as monomers or chromophores)

$$(4.1) \quad |\Psi\rangle = \Pi_m |\phi_m\rangle$$

where $|\phi_m\rangle$ is the monomer state on sites m . These monomer states form the basis function of the overall excitonic states. As the exciton is modelled to be localised to a specific site, an exciton state with an exciton at site i is given by

$$(4.2) \quad |\Psi\rangle^i = |\phi_i\rangle^* \Pi_{m \neq i} |\phi_m\rangle$$

where $|\phi_i\rangle^*$ is the excited state of monomer site i . States with more than one exciton are possible in this framework, however this is not necessary for light harvesting systems as stated in the

introduction. The Hamiltonian, including the "ground state" where there are no excitons in the system, is given in by

$$(4.3) \quad H = \begin{bmatrix} E_0 & V_{0,(1,1)} & \cdots & V_{0,(N,1)} \\ V_{0,(1,1)} & E_{(1,1)} & \cdots & V_{(1,1)(N,1)} \\ \vdots & \vdots & \ddots & \vdots \\ V_{0,(N,1)} & V_{(1,1)(N,1)} & \cdots & E_{(N,1)} \end{bmatrix}$$

where N is equal to the total number of individual sites. The diagonal terms E is the sum of the site energies and a point charge interaction

$$(4.4) \quad E_0 = \sum_m e_m + \sum_{m \neq n, A \in m, B \in n} \frac{q_m^A q_n^B}{r_{AB}}$$

where e_m is the energy of site m and q_m^A is the charge centered on atom A in site m . Hamiltonian elements corresponding to a single excitation are similarly given except with the excited state energy and charges

$$(4.5) \quad E_{(m,1)} = e_m + \delta e_m + \sum_{n \neq m} e_n + \sum_{n, A \in m, B \in n} \frac{q_m^{*A} q_n^B}{r_{AB}} + \sum_{n, p \neq m, A \in n, B \in p} \frac{q_n^A q_p^B}{r_{AB}}$$

where δe_m is the excitation energy of site m , and charges marked q^* are the excited state charges. The inter-site second term has been replaced here to explicitly show that there is both the interaction of excited state point charges with all other sites, as well as the ground-state ground-state interactions for all other non-excited chromophores.

The off diagonal elements are the coupling elements between all exciton states. For coupling to the ground state, these are given by

$$(4.6) \quad V_{0,(m,1)} = \sum_{n, A \in m, B \in n} \frac{q_m^{\text{tr},A} q_n^B}{r_{AB}}$$

where charges marked q^{tr} are transition charges. It can be seen that this coupling element includes an electrostatic interaction between all sites and the excited site. This is different to coupling elements between two single exciton states, given as

$$(4.7) \quad V_{(m,1),(n,1)} = \sum_{A \in m, B \in n} \frac{q_m^{\text{tr},A} q_n^{\text{tr},B}}{r_{AB}}$$

which just involve sites m, n which have local excitations.

This Hamiltonian for exciton states is slightly different those reported in the literature, as the ground state where no excitons are present is not usually included. However, if the local excitations are sufficiently different in energy and the coupling between ground and excited states is weak, then the eigensolution corresponding to the ground state would have mostly ground state character. The other excited state eigensolutions would have very little ground state character, and so the block matrix of just excited state contributions can be taken which would return the Hamiltonian used in many other studies. Calculating the ground state however is necessary if all the states for the exciton system are required, which is the case for the spectral density investigation of the next chapter.

4.1.2 Embedding

4.2 Truncated Chlorophylls

A series of chlorophyll dimers were used to calculate benchmarks for an exciton model based on chl-xTB calculations. The exciton predictions were compared to TD-DFT calculations on the full dimer system. In order to get usable scaling with the DFT methods, a truncated version of chlorophyll with the phytol tail removed was used. In the large separation limit the effects of TD-DFT and chl-xTB coupling should match, with a greater difference in the two methods being present as the chromophores get closer together.

For each dimer, TD-DFT data was calculated for the two monomers separately as well as for the full dimer system. The monomer data was then used to construct the Frenkel Hamiltonian as described above. The benchmarked data was first calculated with PBE0/Def2-SVP, however it was found that an exciton model constructed from monomer data did not well match its full dimer counterpart (see later section on dimer geometries from LHII). As a replacement, the CAM-B3LYP functional was used instead. The exciton model matched the full dimer calculation well.

4.2.1 Rotation

As stated in the introduction, many previous investigations treated inter-chromophores coupling with a point dipole interaction:

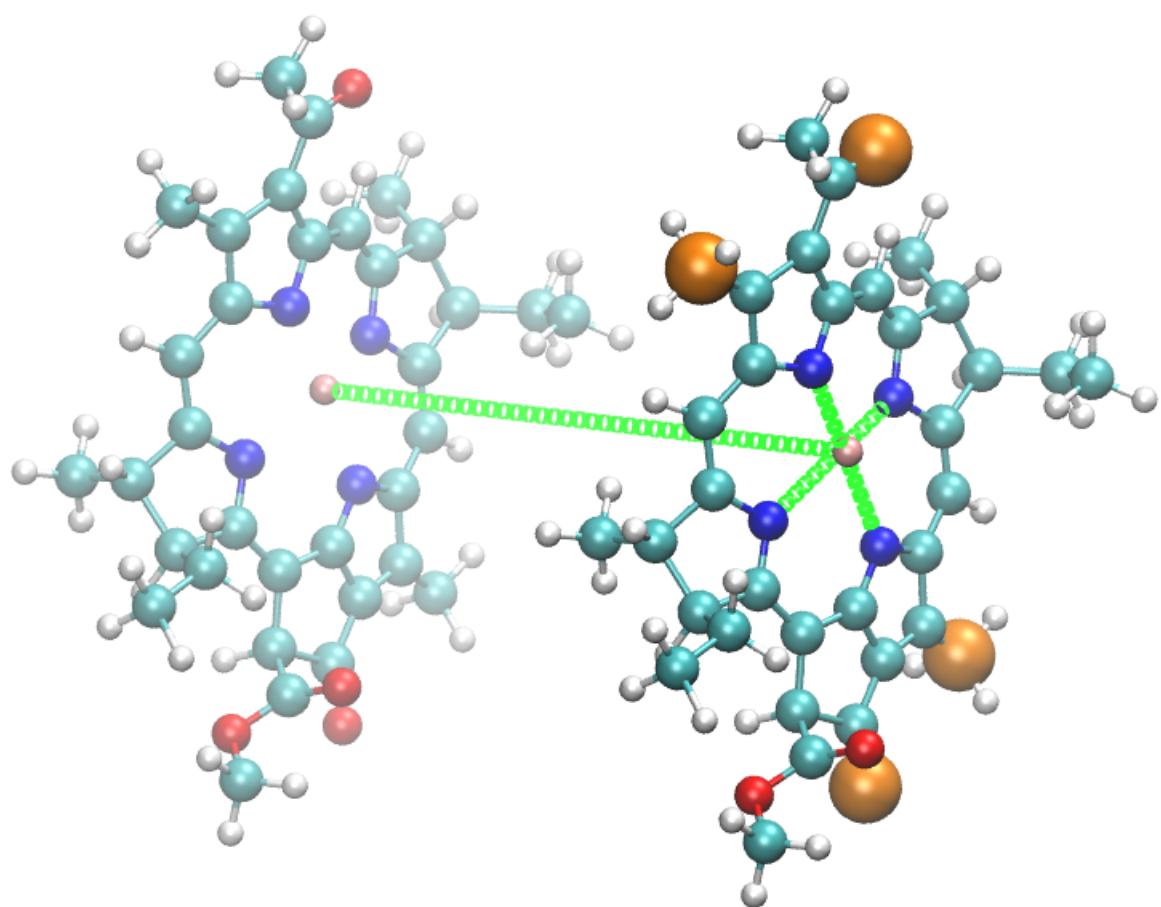
$$(4.8) \quad v_{mn} = \frac{\vec{\mu}_m \cdot \vec{\mu}_n}{r_{mn}}$$

where $\vec{\mu}_m$ is the dipole on site m and r_{mn} is the inter-chromophore distance. From this expression it can be seen that the two inter-chromophore coordinates are the angle and distance in a dimer pair. These two coordinates were scanned in order to get a full picture of how the excited states can be predicted by a chl-xTB exciton Hamiltonian. Due to the large number of calculations necessary, the phytol tails were again removed and replaced with a hydrogen atom. All dimers

were constructed from two truncated chlorophyll molecules with the porphyrin planes parallel and overlapping. The axis along the magnesium atoms was used to define a separation. As this axis is approximately the cross product of the Q_y and Q_x transition dipoles, this axis is labelled Q_z . At each separation, one of the dimers was rotated in increments of 2 degrees up to a full 360 degree rotation for all of the Q_y , Q_x , Q_z axes as an axis of rotation. For all axes, the magnesium atom was the centre of rotation. This could not be done for the Q_y and Q_x axis at a separation lower than 13 angstrom due to the size of the porphyrin ring.

In order to make assignment of exciton states easier, the geometries of the two truncated chlorophyll monomers were altered such that there would be a distinct gap in their transition energies. This gap was not wider than the variation in transition energies found in LHII monomers. More detail on assigning transition energies to the correct excited state is discussed below. The plot of the two excited state energies for both CAM-B3LYP dimer and chl-xTB exciton methods are shown in fig., where they have been aligned to their average values to remove the systematic shift.

It can be seen that the chl-xTB exciton model can reproduce high level TD-DFT dimer data with an excellent level of accuracy. The energies for both excited states agree across the entire range of angles, and much of the detailed variation in the CAM-B3LYP data is also found in the chl-xTB data.. The two areas where the agreement is worse is at 180 degrees and 270 degrees, where the coupling is strong and weak respectively. This is attributed to the proximity of functional groups that are found at the corners of the porphyrin ring, which are closest at these angles. As these groups get closer together, the difference between the TD-DFT and chl-xTB treatment would be expected to cause transition energies to grow more distinct. However it can be seen that even with these effects the difference is small. Additionally, the angle of chlorophyll pairs in LHII (for B850 a,b pairs) only varies around 0 by a few degrees, so these effects would not be so present.



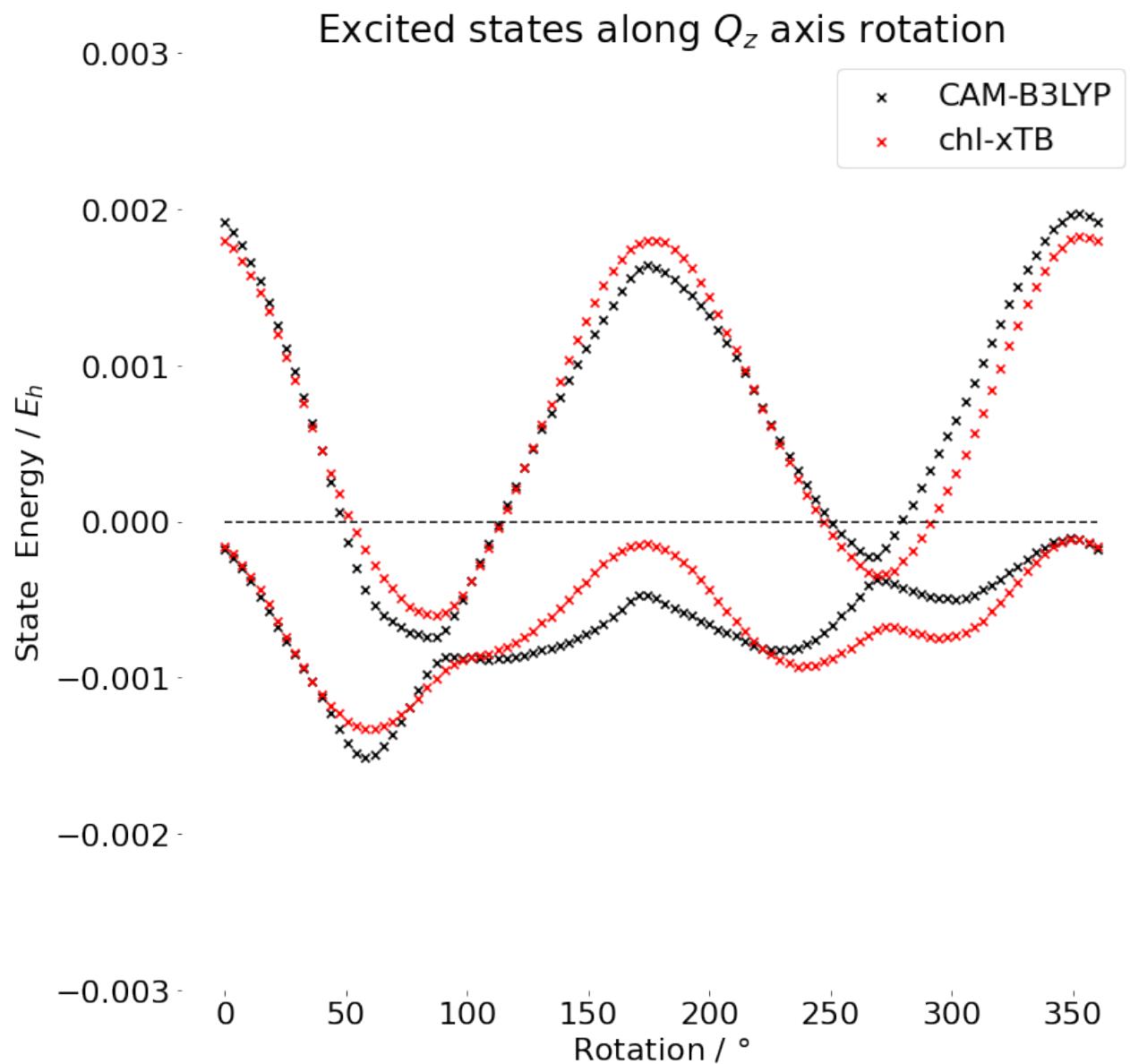


Figure 4.1: caption

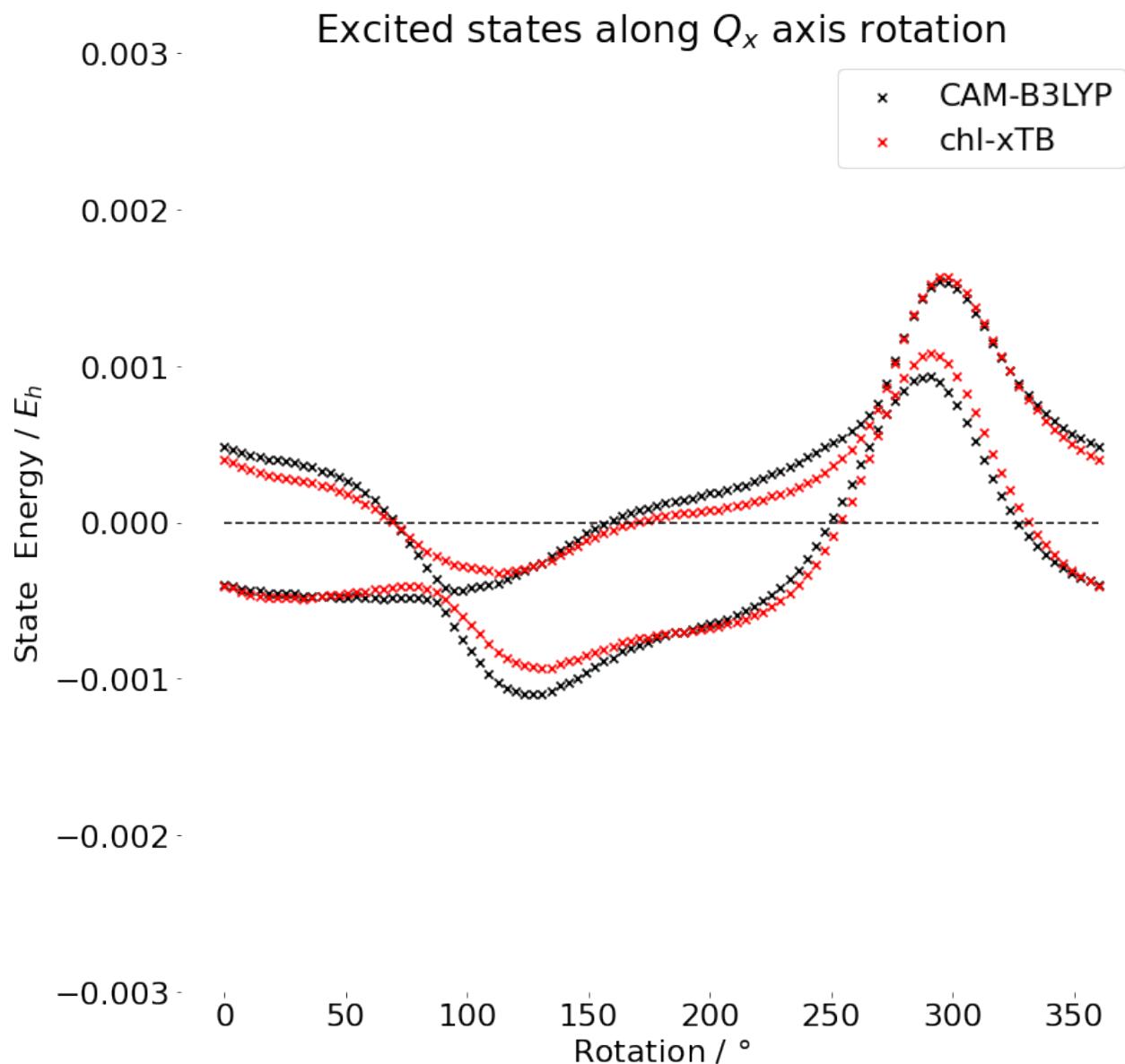


Figure 4.2: caption

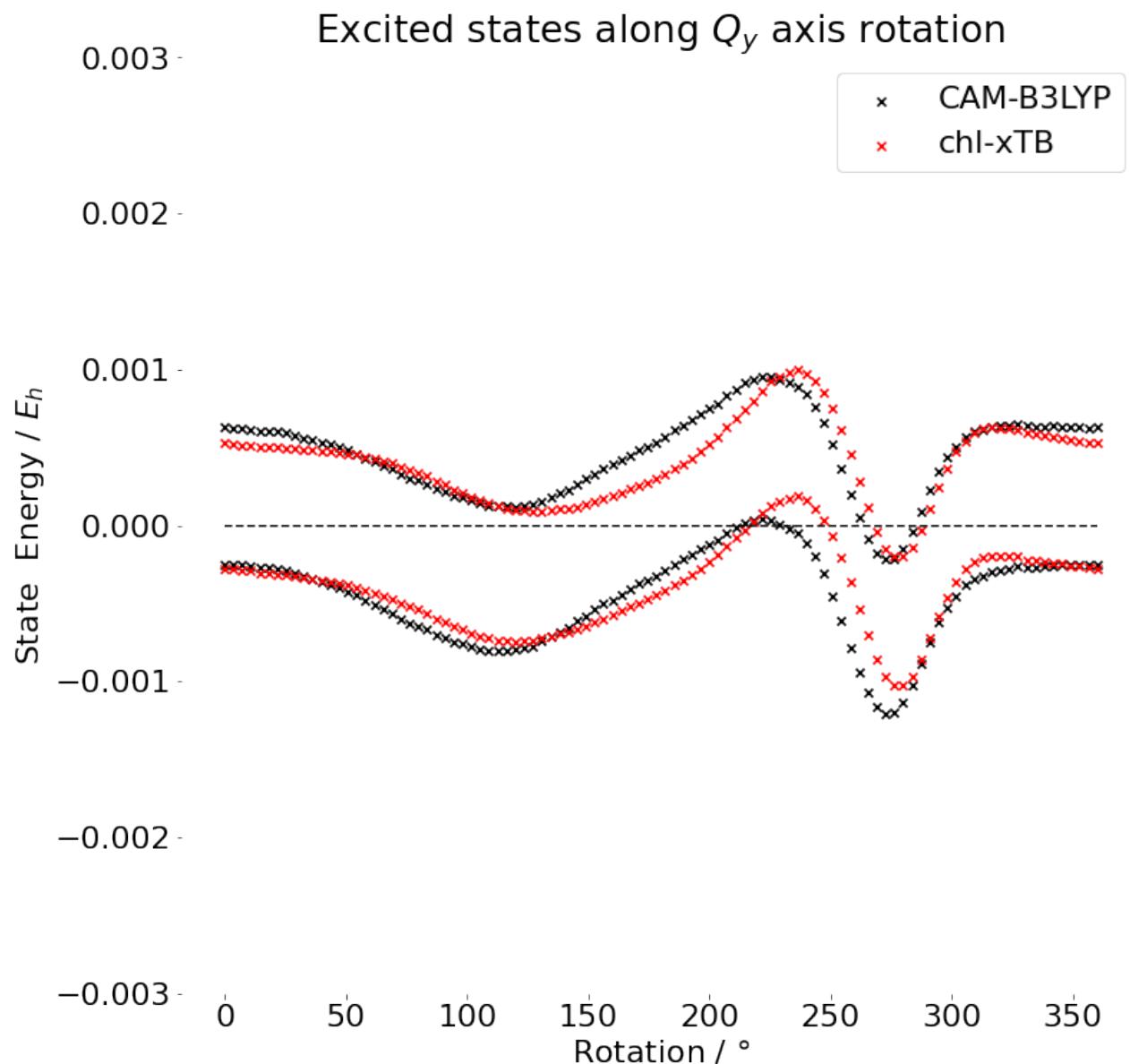
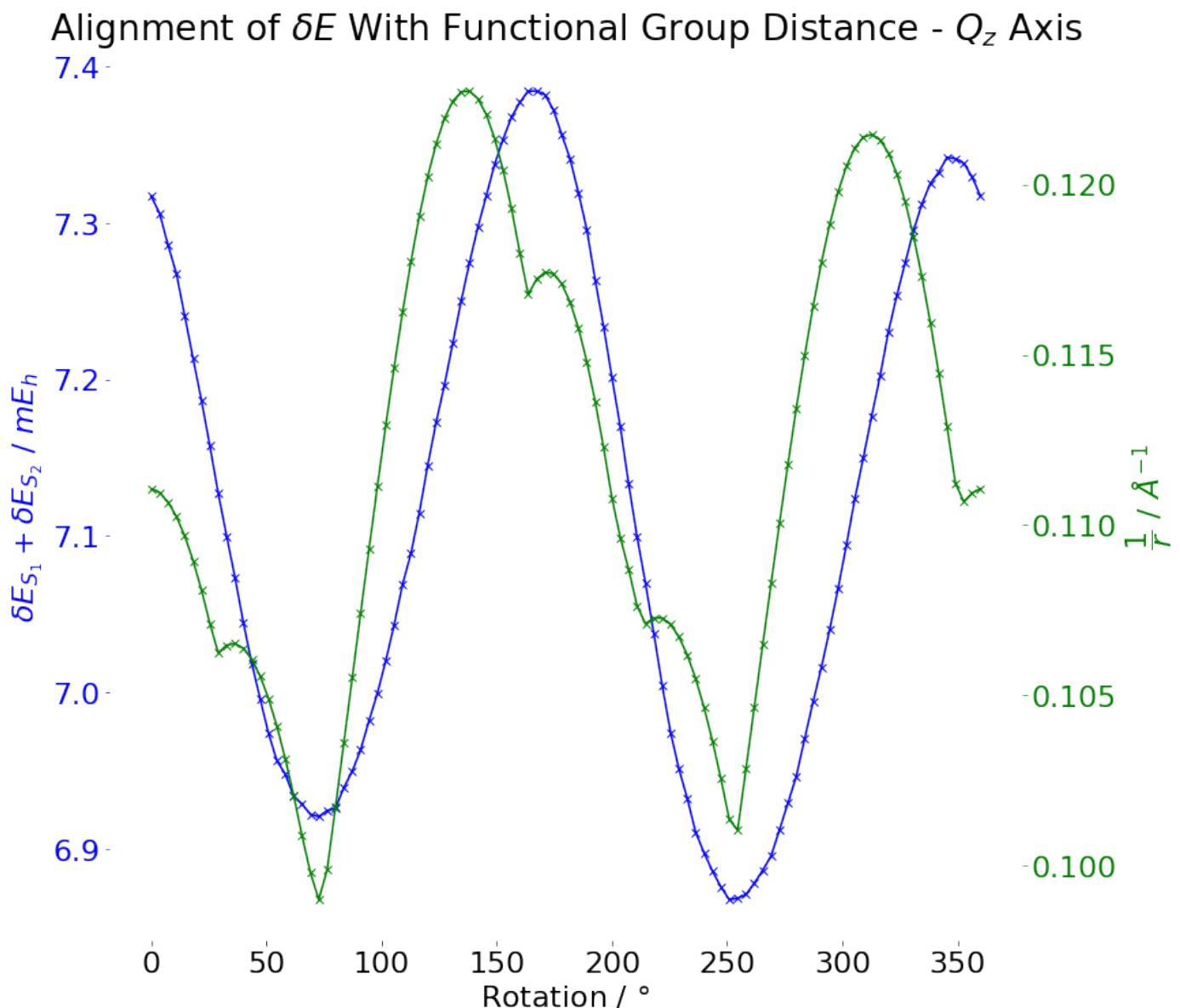
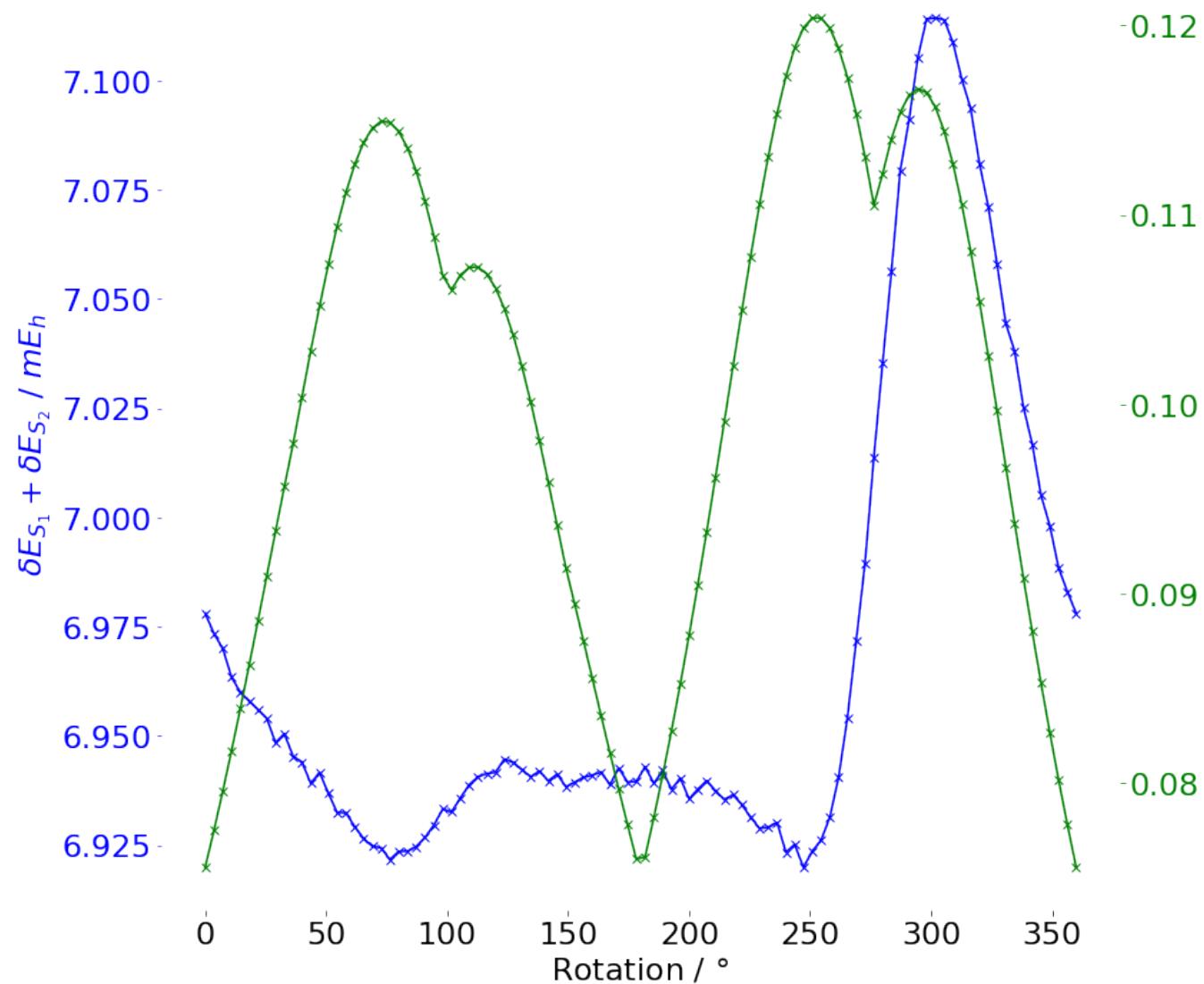
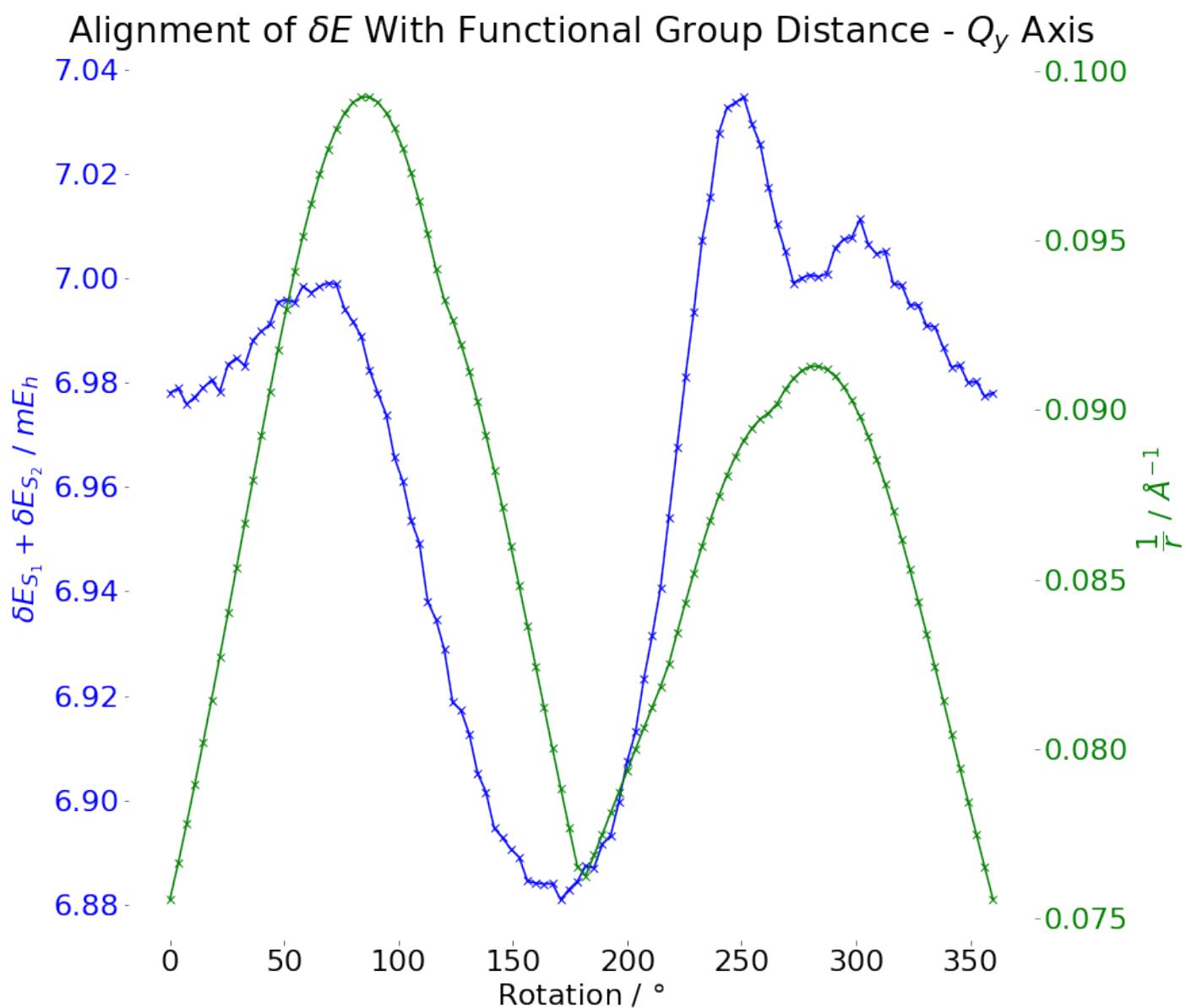


Figure 4.3: caption



Alignment of δE With Functional Group Distance - Q_x Axis



4.3 LHII Pairs

Whilst the rotations and separation scans cover a large range of the orientations between chlorophyll pairs, the best way to test orientations that would be found in LHII would be to take pairs from the protein system. This was done for a small set, taking every pair from the 27 chlorophylls from 3 frames of the earlier reported MD, giving 1053 pairs. Every dimer pair was included to scan over B800 and B850a/b interactions, although many of these after nearest-neighbours would have almost zero coupling. Similar to the coordinate scan tests above, both full dimer TD-DFT and exciton model transition energies were calculated.

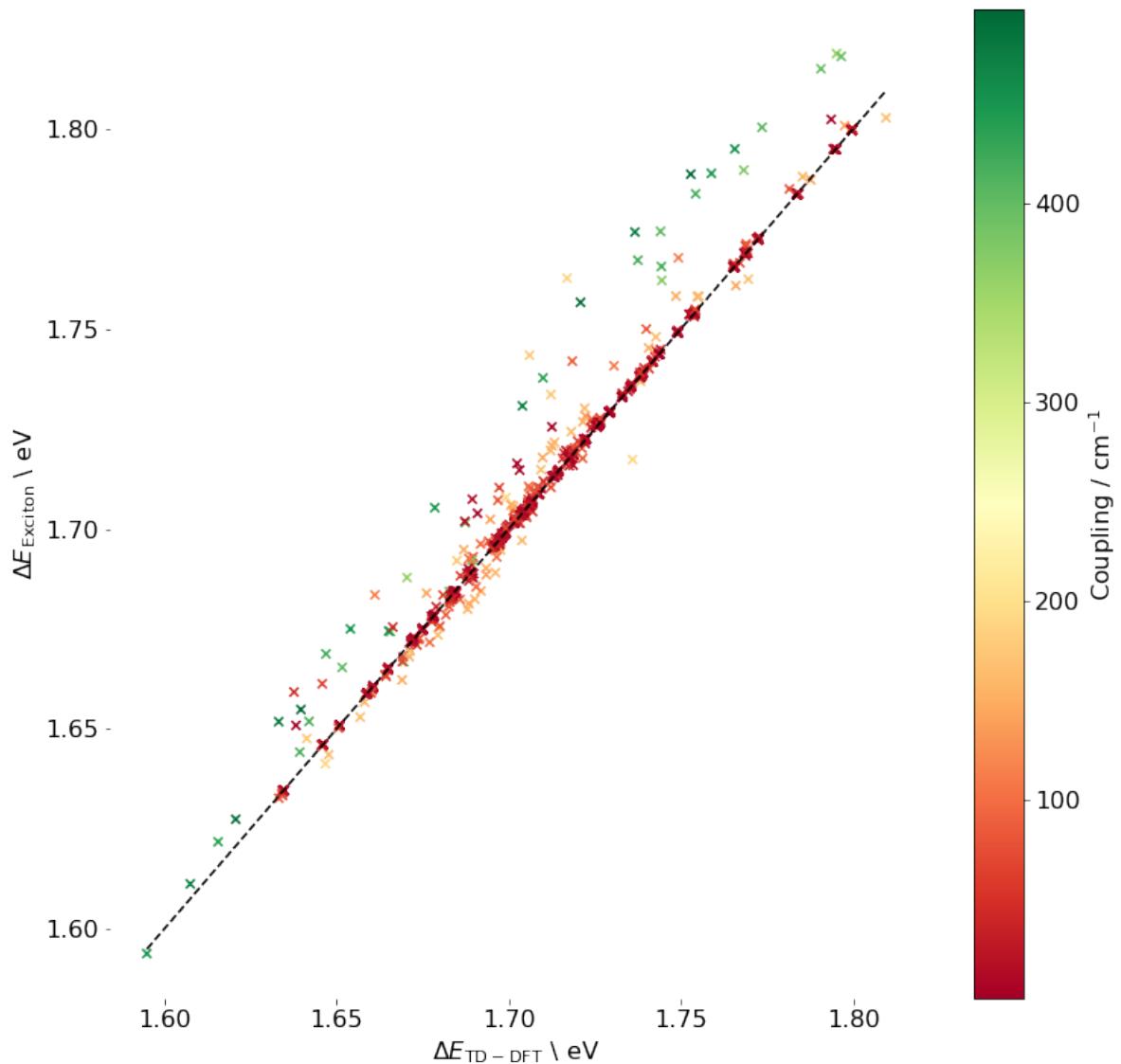
4.3.1 Assignment of States

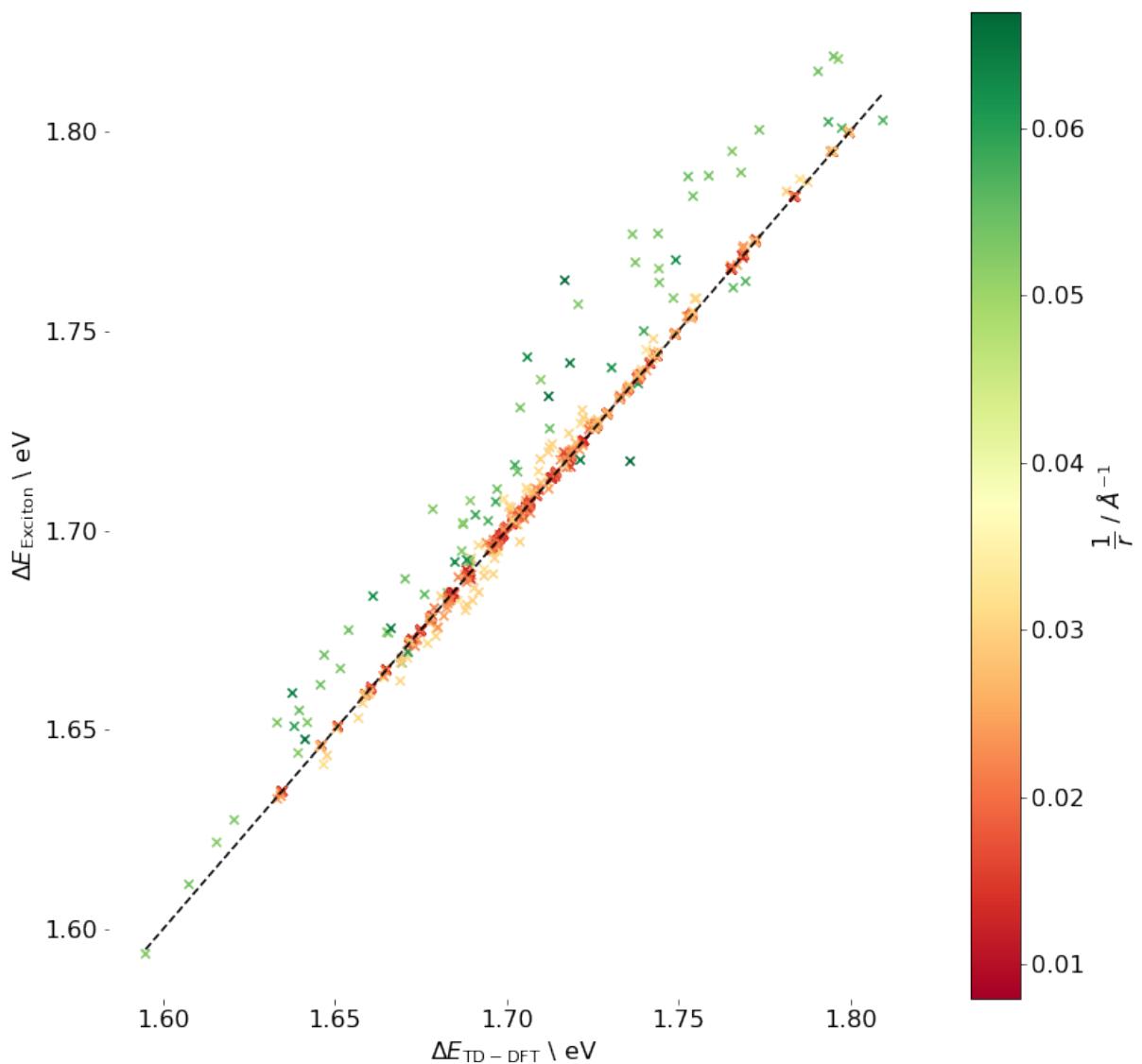
A more detailed view of each exciton state was needed to properly assign the two excited states from the full TD-DFT and exciton models. It was found that for some dimer pairs, the models would predict different energy ordering. More explicitly, for the A-B dimer system, one model might predict a lower energy for a state with the exciton localised on monomer A, whereas another might predict the other state with the exciton on B. It should be noted that the CAM-B3LYP exciton model and full dimer data were always consistent, and it was only when comparing to PBE0 or chl-xTB was this effect apparent. It was therefore necessary to find the location of the excitons in both dimer and exciton models. For the TD-DFT dimer result, the exciton location was taken as the molecule where the transition charge distribution centered around. This centre was calculated by the absolute charge weighted average of the atomic position. For the Frenkel exciton result, the location was taken as the monomer which had the most amount of character in the eigenvector solution.

4.3.2 Comparison

4.3.2.1 CAM-B3LYP

In the ideal case, the TD-DFT and Frenkel exciton framework should match transition energies very well, with small differences in the small distance limit. This can be seen in the CAM-B3LYP data in figures 4.3.2.1 and 4.3.2.1 where a scatter plot of the TD-DFT and exciton transition energies reveal a very strong correlation with little systematic error. The coupling energies between transitions are used to colour gradient the points in figure 4.3.2.1, with the distance being used to colour points in figure 4.3.2.1. The better correlation of distance rather than coupling energy to the error suggests that there are interactions present in the TD-DFT model that are missing in the exciton framework. However, this error is small. Using CAM-B3LYP transition properties for the exciton framework can therefore recover the TD-DFT properties very well.





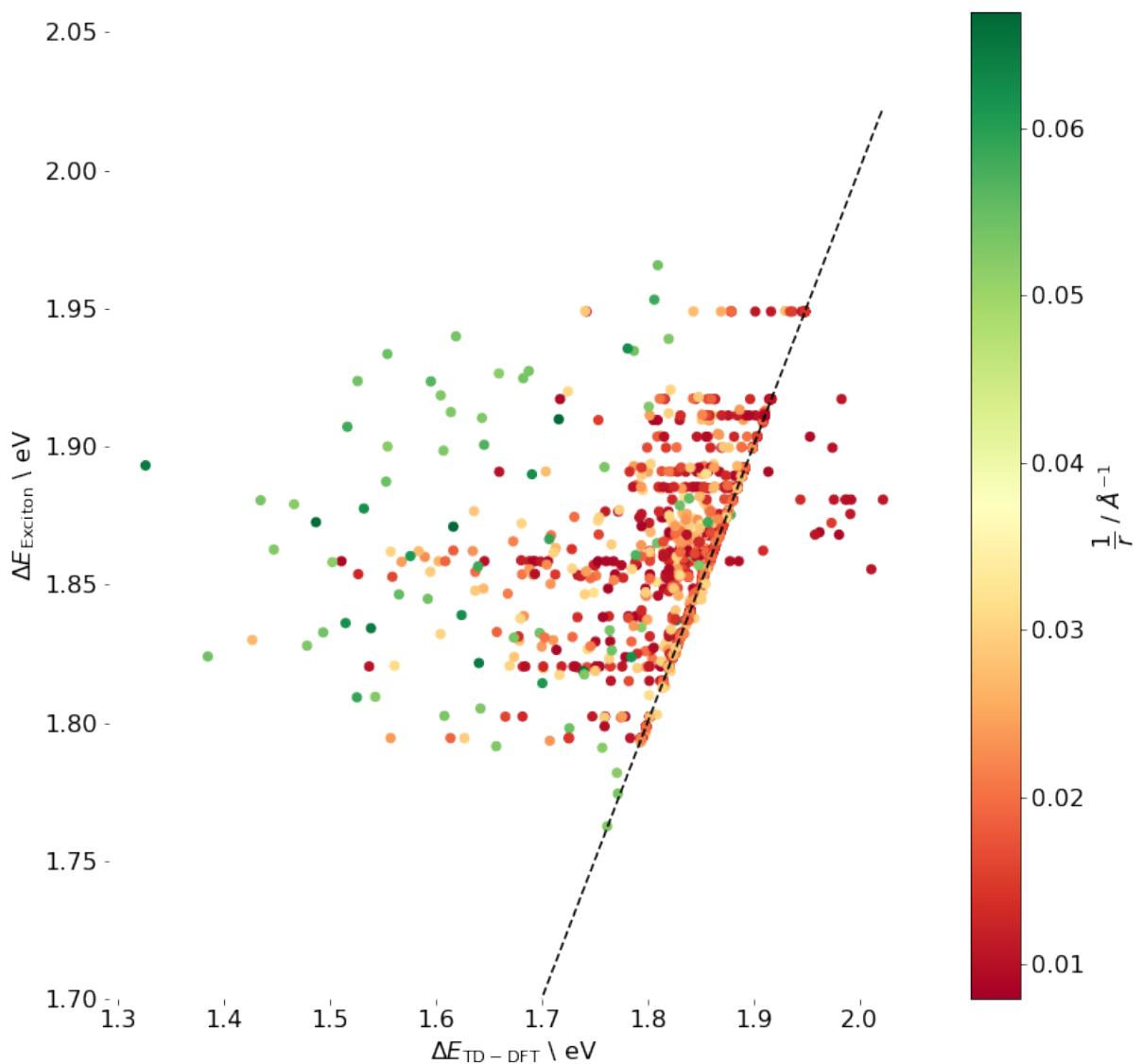
4.3.2.2 PBE0 and Charge Transfer

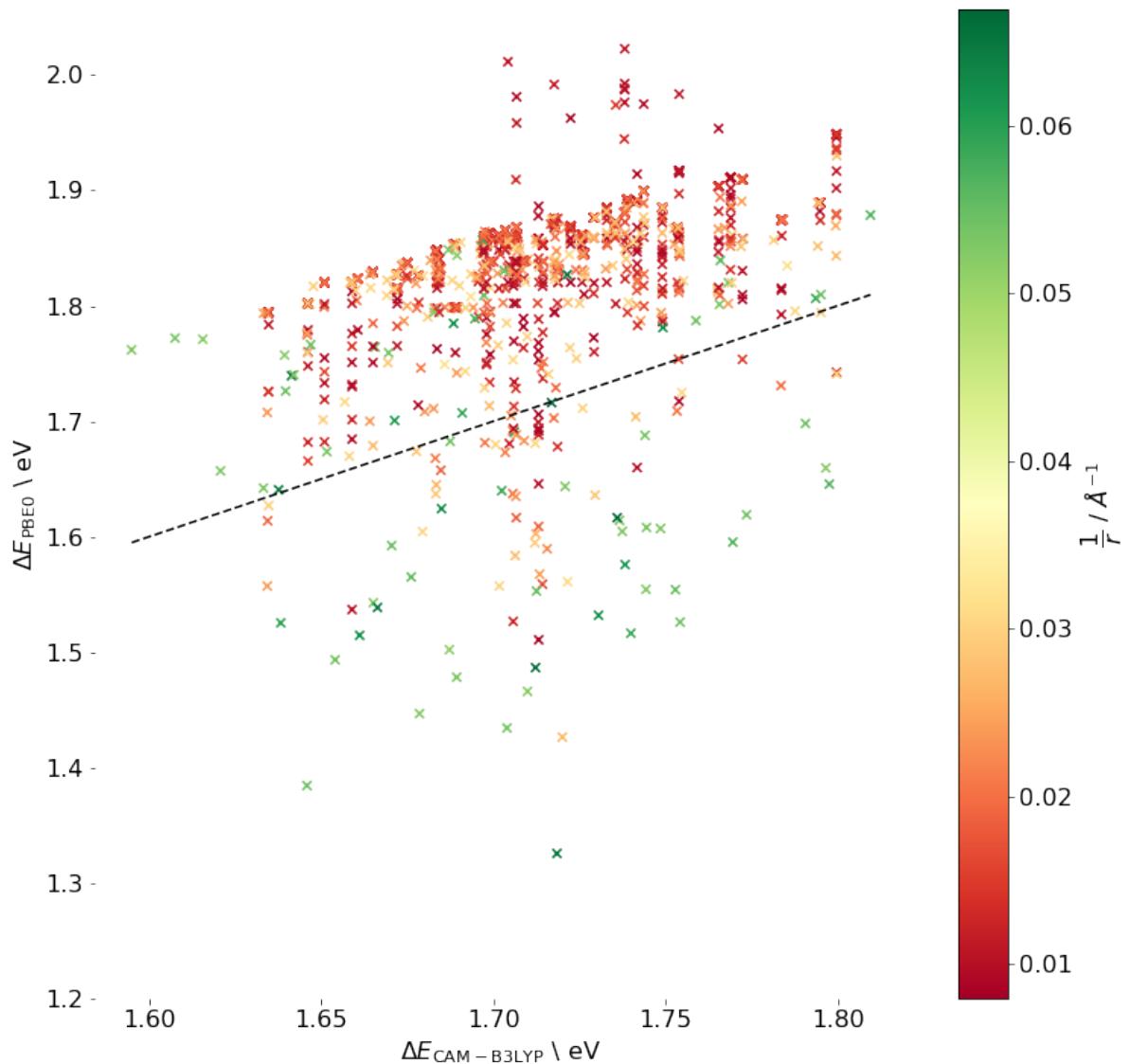
It would have been preferable to benchmark the chl-xTB against PBE0 due to this being used as to construct the training data. However it was found that many of the TD-DFT transitions had charge transfer character between the two dimers, which should not be present. This skewed many of the transitions to lower energy, as seen in figure 4.3.2.2. Here the probability distribution of transition energies from the chlorophyll monomers and dimers have been plotted. For CAM-B3LYP the dimer distribution matches the monomer distribution well with slight differences due to exciton coupling. For PBE0 however, a clear skew to lower transition energies can be seen in the dimer distribution, which from looking at the TD-DFT solution characters was due to charge transfer character. It was found that there were two effects on the PBE0 transitions. First was the closer proximity of charge transfer excitations to vertical excitations in the TD-DFT solutions, which was not present in the CAM-B3LYP data. These were easier to assign and remove, as although the transition energies were closer to the vertical excitations the characters were sufficiently different to allow clear assignment. The second was the mixing of charge transfer and vertical excitation into transitions, which made assignment more difficult. As the first effect could be removed due to their easier assignment, the second is the cause of the continuous skew seen in the distributions.

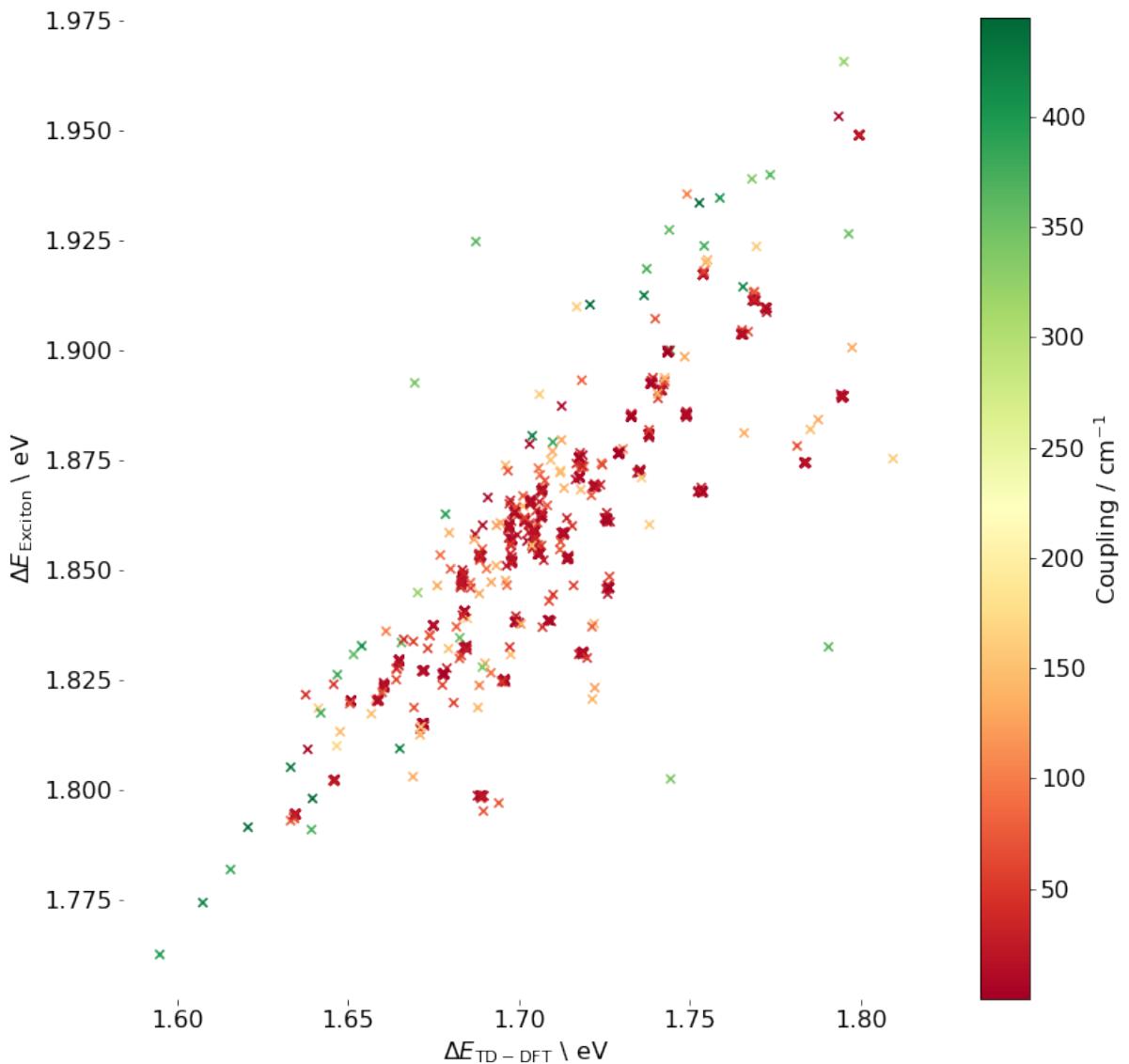


Due to this charge transfer character, the correlations of both PBE0 exciton to PBE0 TD-DFT transitions and PBE0 TD-DFT to CAM-B3LYP TD-DFT transitions were found to be very poor. This can be seen in figures 4.3.2.2 and 4.3.2.2. It can be seen that as the separation in dimers gets smaller (a larger reciprocal distance), the error to the reference data gets worse. This is attributed to the proximity of the monomers promoting the charge transfer effects. The plot of PBE0 transitions against CAM-B3LYP transitions in figure 4.3.2.2 show how the PBE0 TD-DFT transitions do lead to poor correlation between PBE0 exciton and TD-DFT data, and it is not due to any inaccuracy in using the PBE0 monomer data for the exciton framework.

This is more clearly shown in plotting the PBE0 exciton transitions against CAM-B3LYP TD-DFT data, as shown in figure 4.3.2.2. Here there is a clear correlation from the exciton model. The leading cause of error in this comparison is attributed to the difference in the two functionals rather than the exciton framework itself, due to the high correlation seen in figure 4.3.2.1 as well as the RMSE being comparable to that between PBE0 and CAM-B3LYP in the reference data of the previous chapter. Additionally, the lack of correlation between coupling energy and transition energy error also implies the exciton framework is not the leading cause of this error. The four outliers, which all do have a high coupling value, can be explained due to this effect, where the two leading causes of error have compounded.

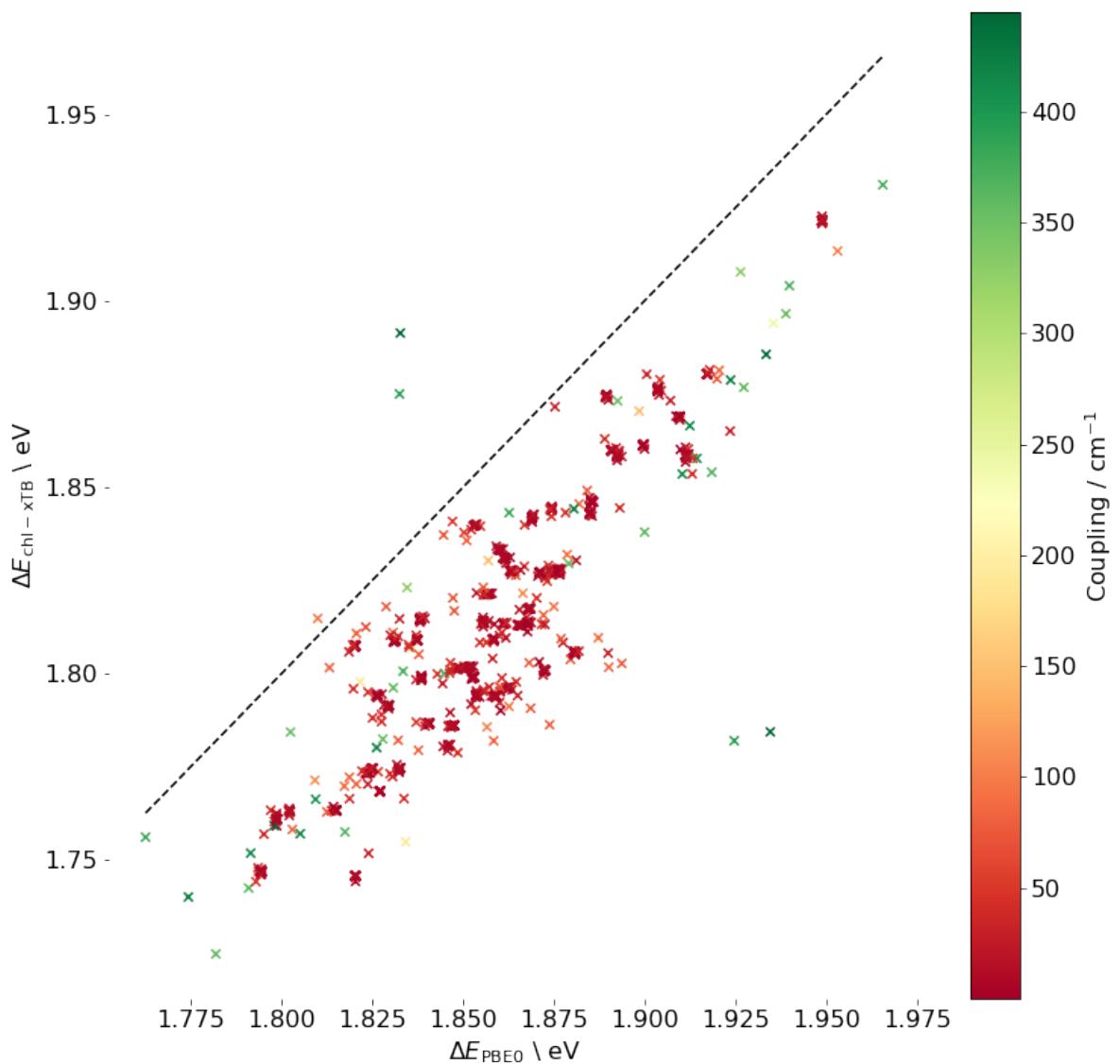


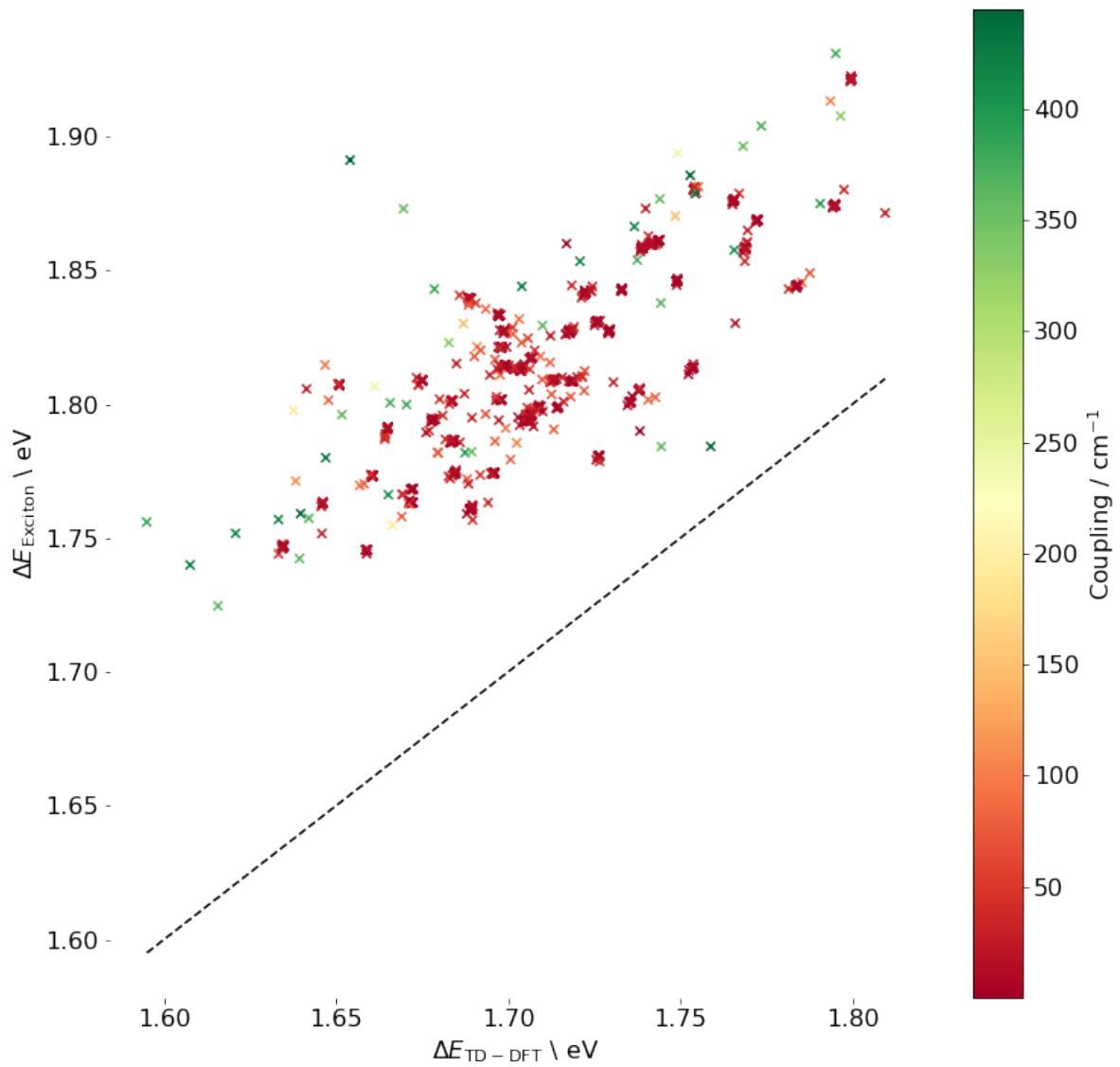




4.3.2.3 chl-xTB

With all of these benchmarks in mind, it can be seen that using the chl-xTB data to construct the Frenkel Hamiltonian performs about as well as can be expected. Scatter plots of the chl-xTB exciton transitions against PBE0 excitons and CAM-B3LYP TD-DFT transitions are shown in figures and respectively. Both show decent correlation from the exciton transitions, with the same 4 outlier transitions as seen in the previous scatter plot. The variance to the best fit is again similar to the RMSE from the parameter optimisation, and there is little correlation between coupling and error, suggesting that it is the chl-xTB response theory and not the exciton framework that is the leading cause of error.



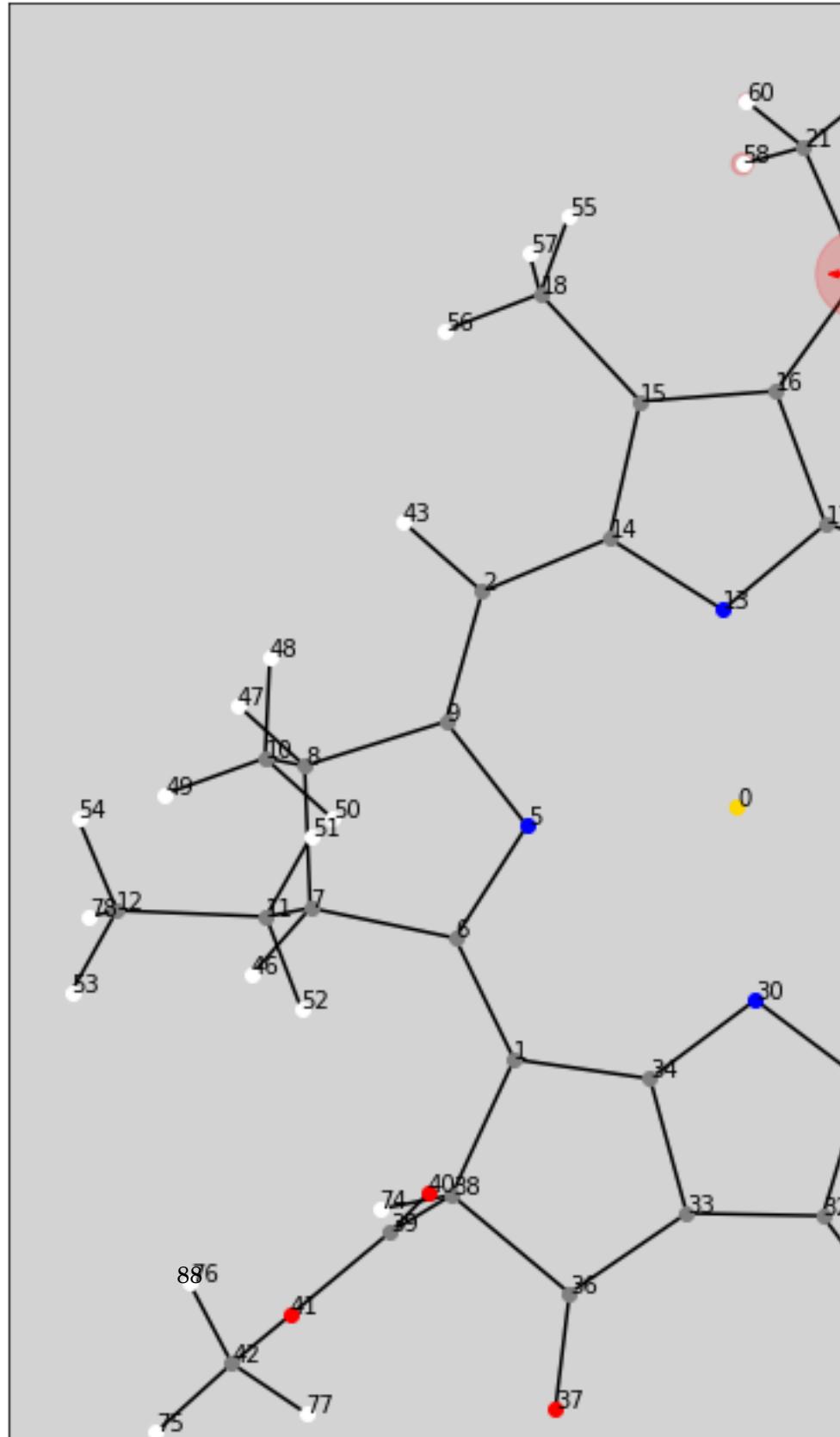


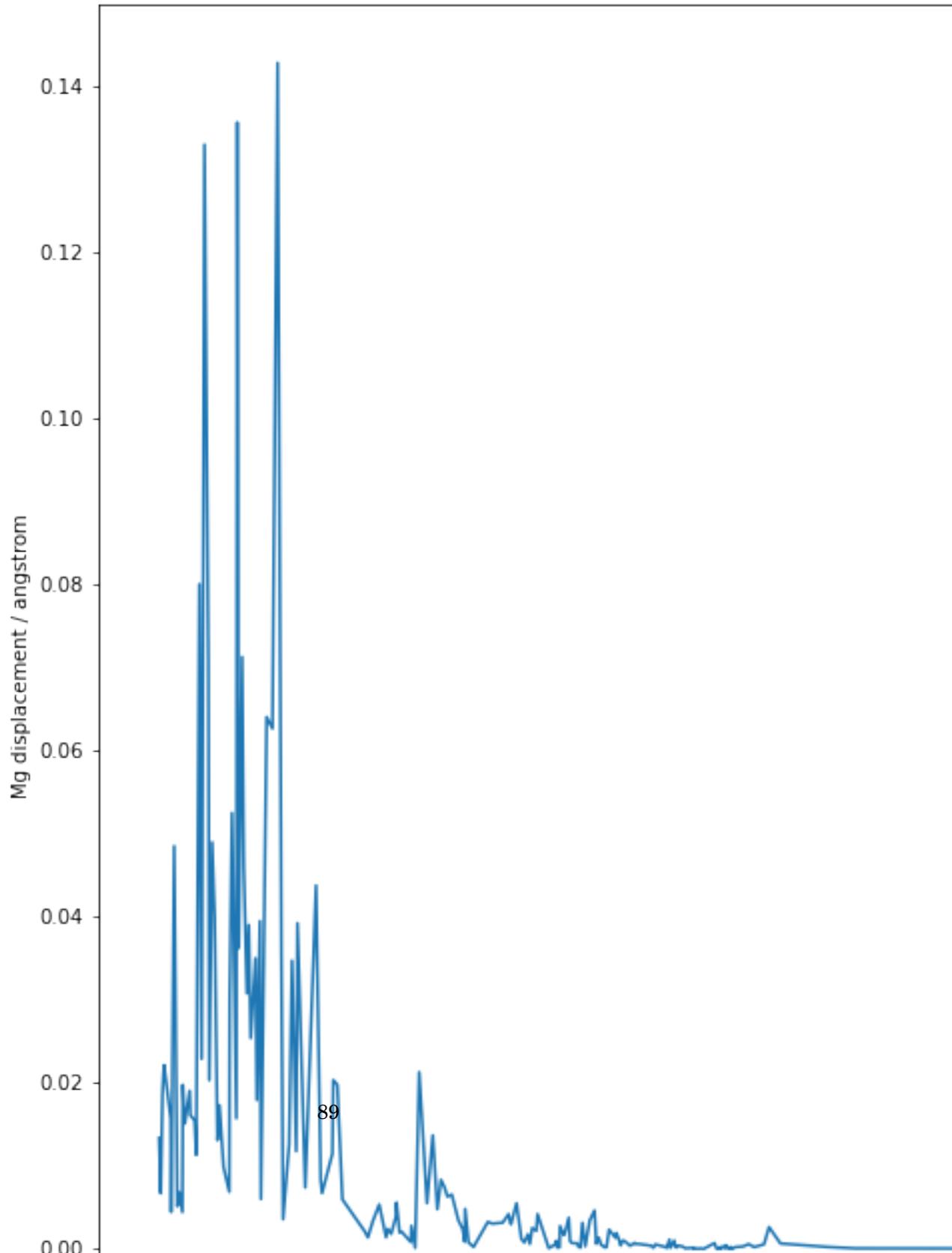
4.4 Conclusions

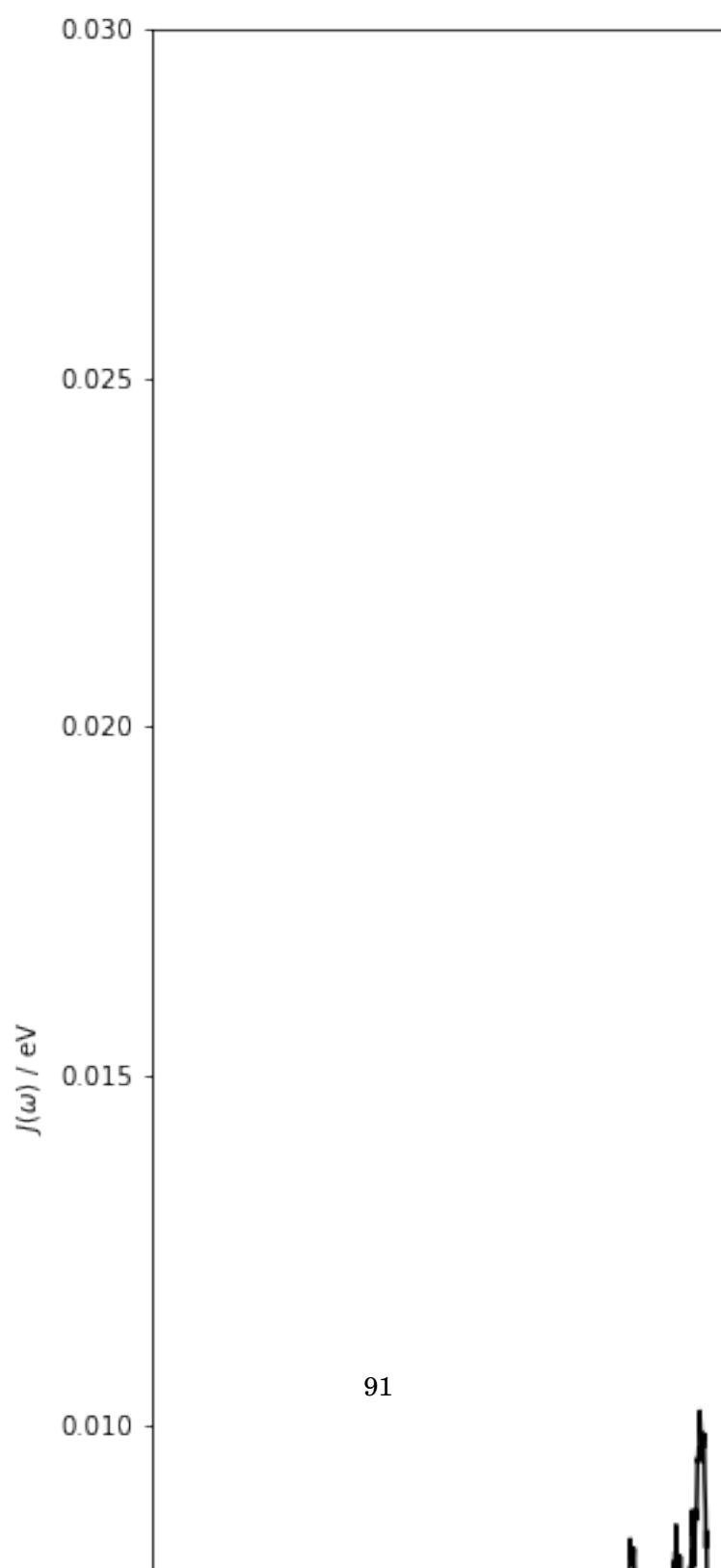
C H A P T E R



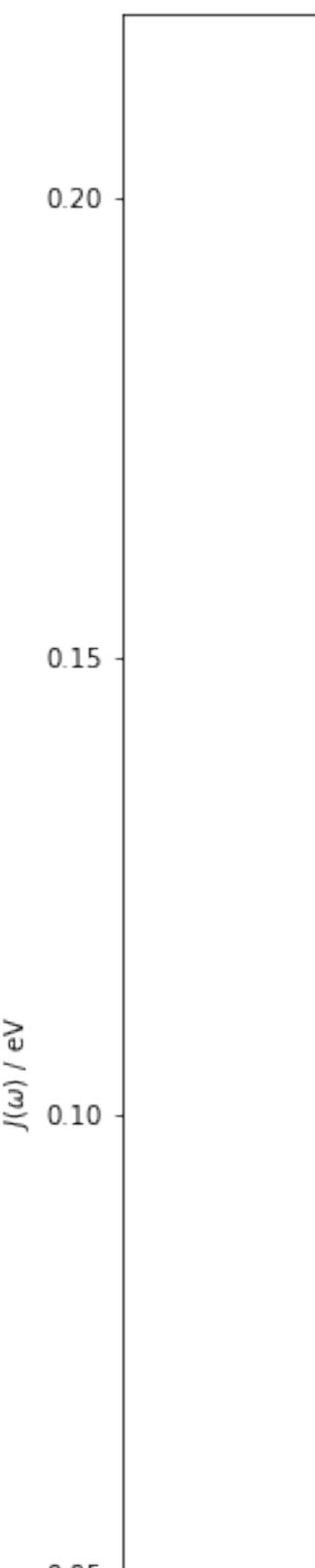
ATOMISTIC MODELLING OF LIGHT HARVESTING COMPLEXES

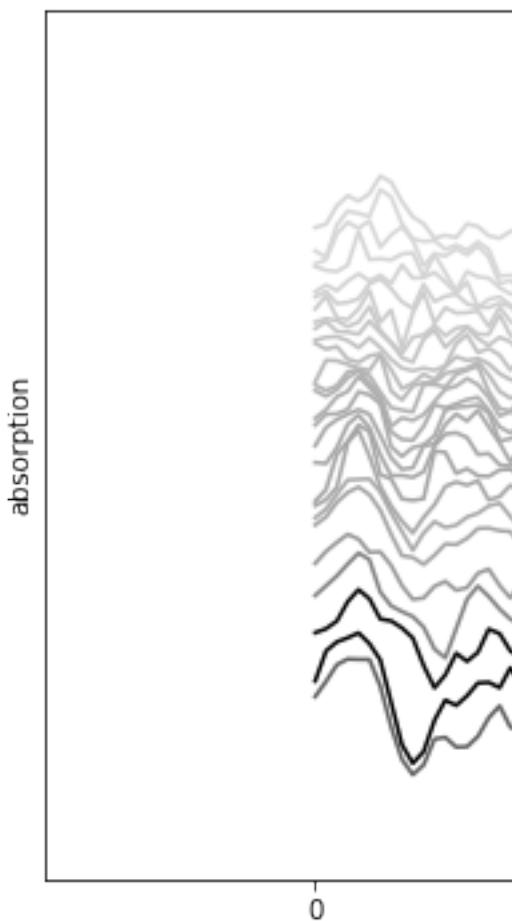


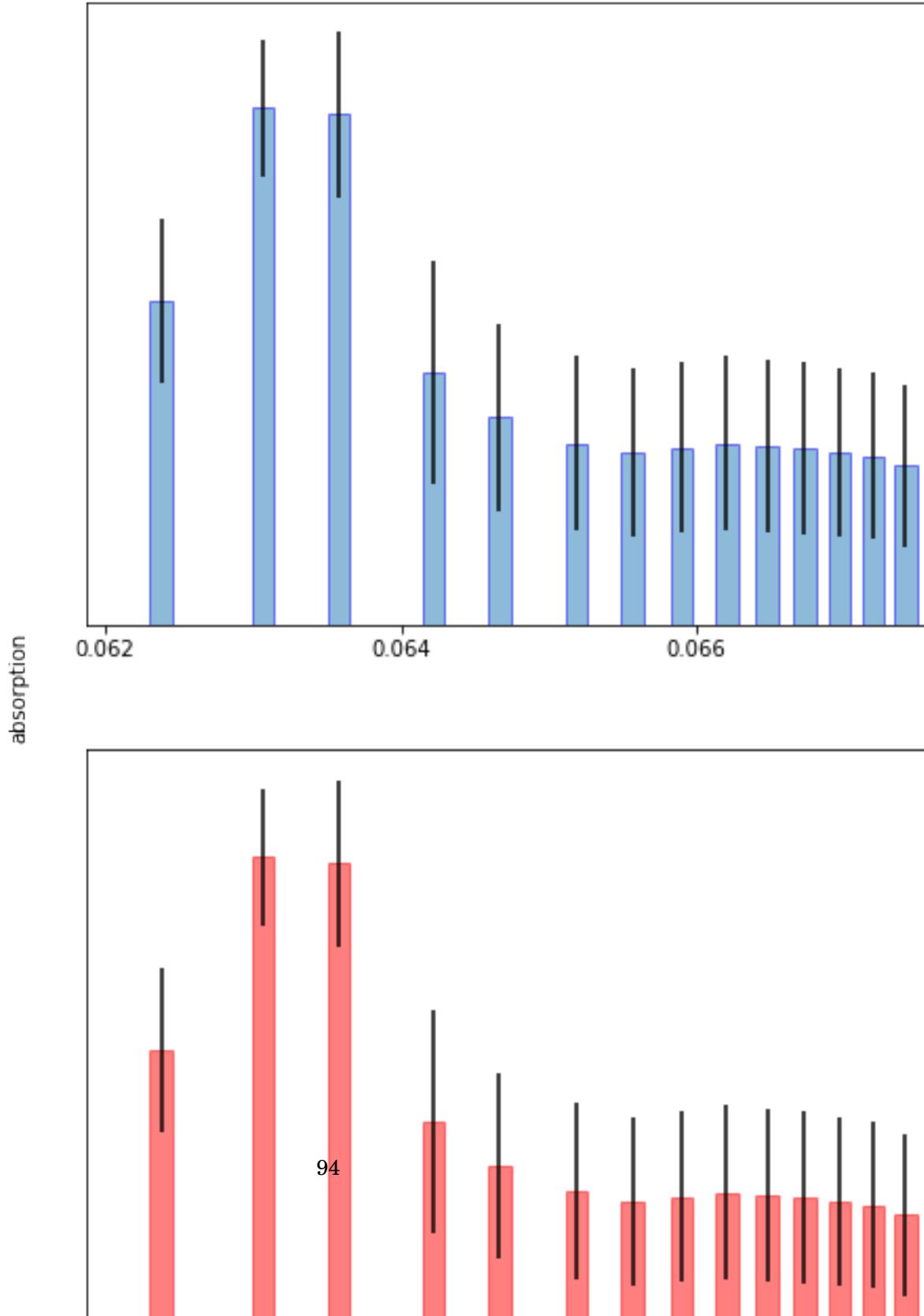




91







5.1 LHII

5.1.1 Spectral Density Method

5.1.2 Molecular Dynamics Method

5.2 Approximating Spectral Densities

5.2.1 Hessians

5.2.2 Huang Rhys Factors

5.2.3 Chlorophyll distances

5.3 Environmental Effects

5.3.1 Screening

5.3.2 Embedding

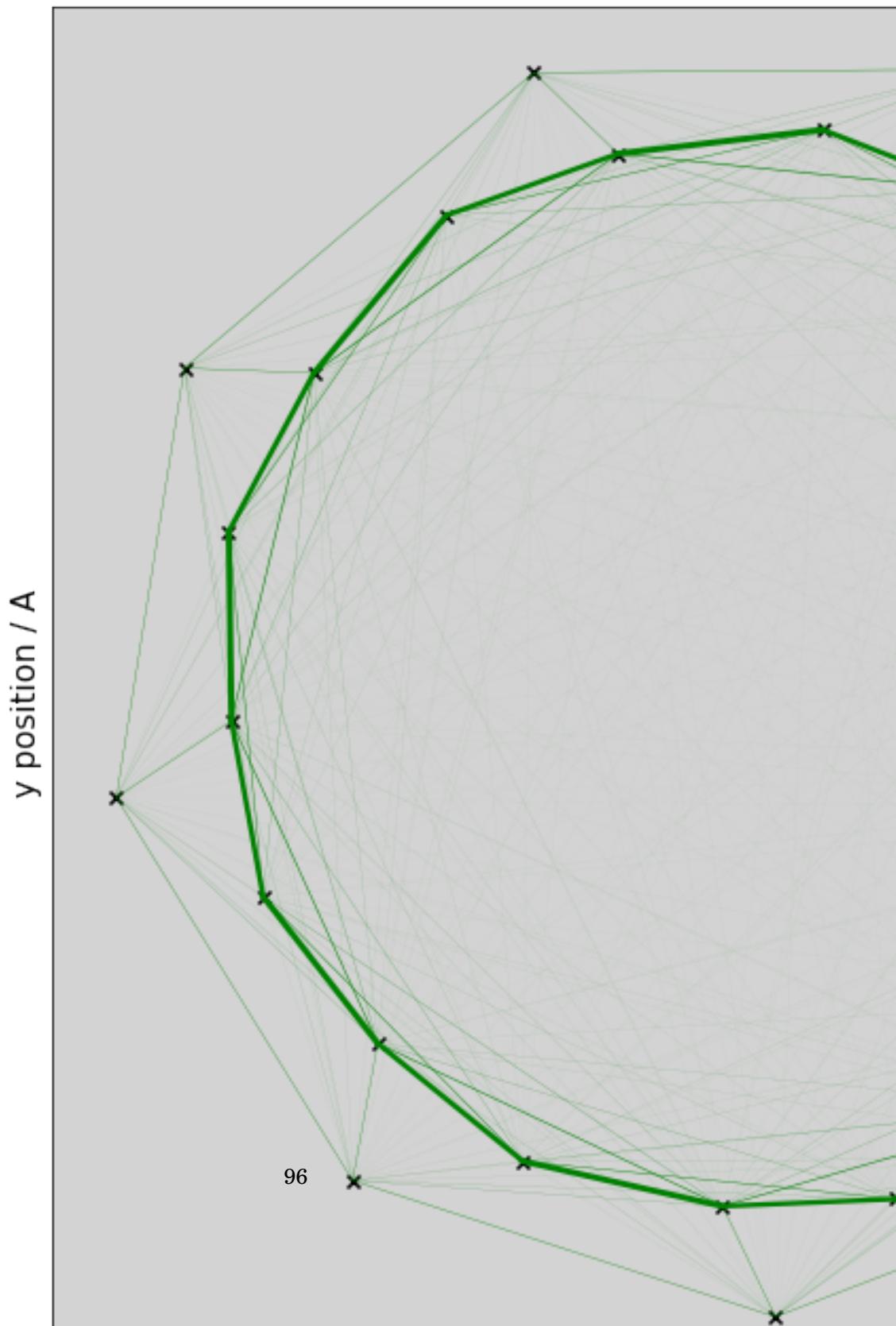
5.4 Sites, states and couplings

5.4.1 Sites

5.4.2 Exciton states

5.4.3 Coupling

5.5 Excitation Energies



DISCUSSION

Preamble

6.1 Transition Property Approximations

6.2 Further Investigations into LHII

6.3 Coherence



APPENDIX A

This appendix covers the common computational details of this work. Included are the software packages, hardware used. These are not exhaustive list, and additional details are provided in the main chapters. However, wherever implementations or methodology details are missing, the information will be found here.

A.1 Electronic Structure Codes

This project has primarily used the QCORE software that is found as part of the ENTOS project. This is a software package for DFT and DFTB electronic structure calculations that has been written as a joint venture between the Miller group in California Institute of Technology and the Manby group in the University of Bristol. It is now being hosted by Entos Inc. It is a novel C++ implementation, with a focus on modularity, functional code and modern development practices to enable easier, cleaner and more reuseable code. All novel methods discussed in the chapters have been implemented in the QCORE package.

A.2 Computational Hardware

BIBLIOGRAPHY

- [1] *mcodev31/libmsym: molecular point group symmetry lib.*
- [2] C. ADAMO AND V. BARONE, *Towards reliable density functional methods without adjustable parameters: The PBE0 model*, J. Chem. Phys1, 110 (1999), p. 6158.
- [3] C. BANNWARTH, C. EIKE, S. EHLERT, A. HANSEN, P. PRACHT, J. SEIBERT, S. SPICHER, AND S. GRIMME, *Extended tight-binding quantum chemistry methods*, WIREs Comput. Mol. Sci., 11 (2020), p. 1493.
- [4] N. A. BESLEY, A. T. B. GILBERT, AND P. M. W. GILL, *Self-consistent-field calculations of core excited states*, J. Chem. Phys, 130 (2009), p. 124308.
- [5] Y. CHO, S. J. BINTRIM, AND T. C. BERKELBACH, *A simplified GW/BSE approach for charged and neutral excitation energies of large molecules and nanomaterials*, (2021).
- [6] D. J. FRISCH, M. J.; TRUCKS, G. W.; SCHLEGEL, H. B.; SCUSERIA, G. E.; ROBB, M. A.; CHEESEMAN, J. R.; SCALMANI, G.; BARONE, V.; PETERSSON, G. A.; NAKATSUJI, H.; LI, X.; CARICATO, M.; MARENICH, A. V.; BLOINO, J.; JANESKO, B. G.; GOMPERTS, R.; MENNUCCI, B.; HRATCH, *Gaussian 16, Revision C.01*, 2016.
- [7] J. GASTEIGER AND M. MARSILI, *A new model for calculating atomic charges in molecules*, Tetrahedron Lett., 19 (1978), pp. 3181–3184.
- [8] J. GAVNHOLT, T. OLSEN, M. ENGELUND, AND J. SCHIØTZ, *self-consistent field method to obtain potential energy surfaces of excited molecules on surfaces*, Phys. Rev. B, 78 (2008), p. 075441.
- [9] A. T. B. GILBERT, N. A. BESLEY, AND P. M. W. GILL, *Self-Consistent Field Calculations of Excited States Using the Maximum Overlap Method (MOM) †*, J. Phys. Chem., 112 (2008), p. 13164.
- [10] T. GIMON, A. IPATOV, A. HESSELMANN, AND A. GÖRLING, *Qualitatively Correct Charge-Transfer Excitation Energies in HeH+ by Time-Dependent Density-Functional Theory Due to Exact Exchange Kohn-Sham Eigenvalue Differences*, J. Chem. Theory Comput, 5 (2009), p. 27.

BIBLIOGRAPHY

- [11] S. GRIMME, *A simplified Tamm-Dancoff density functional approach for the electronic excitation spectra of very large molecules*, J. Chem. Phys., 138 (2013), p. 244104.
- [12] S. GRIMME AND C. BANNWARTH, *Supporting information for: Ultra-fast computation of electronic spectra for large systems by tight-binding based simplified Tamm-Dancoff approximation (sTDA-xTB)*, tech. rep.
- [13] ———, *Ultra-fast computation of electronic spectra for large systems by tight-binding based simplified Tamm-Dancoff approximation (sTDA-xTB)*, J. Chem. Phys., 145 (2016), p. 54103.
- [14] S. GRIMME, C. BANNWARTH, AND P. SHUSHKOV, *A Robust and Accurate Tight-Binding Quantum Chemical Method for Structures, Vibrational Frequencies, and Noncovalent Interactions of Large Molecular Systems Parametrized for All spd-Block Elements (Z = 1-86)*, J. Chem. Theory Comput., 13 (2017), pp. 1989–2009.
- [15] C. HÄTTIG AND F. WEIGEND, *CC2 excitation energy calculations on large molecules using the resolution of the identity approximation*, J. Chem. Phys., 113 (2000), p. 5154.
- [16] A. HELLWEG, S. A. G. GRUÑN, AND C. H. HÄTTIG, *Benchmarking the performance of spin-component scaled CC2 in ground and electronically excited states*, Phys. Chem. Chem. Phys., 10 (2008), pp. 4119–4127.
- [17] S. W. J. HUNT AND W. A. GODDARD, *Excited States of H₂O using improved virtual orbitals*, Chem. Phys. Lett., 3 (1969), pp. 414–418.
- [18] J. KIM, J. JEON, T. HYUN YOON, AND M. CHO, *Two-dimensional electronic spectroscopy of bacteriochlorophyll a with synchronized dual mode-locked lasers*, Nat. Commun., 11 (2020), p. 6029.
- [19] G. KLOPMAN, V. 86, J. LINEVSKY, K. S. SESHADEVI, AND D. WHITE, *A Semiempirical Treatment of Molecular Structures. II. Molecular Terms and Application to Diatomic Molecules*, J. Am. Chem. Soc., 86 (1964), pp. 4550–4557.
- [20] T. KOWALCZYK, S. R. YOST, AND T. VAN VOORHIS, *Assessment of the D-SCF density functional theory approach for electronic excitations in organic dyes*, J. Chem. Phys., 134 (2011), p. 164101.
- [21] T. LIU, W.-G. HAN, F. HIMO, . G. M. ULLMANN, D. BASHFORD, A. TOUTCHKINE, K. M. HAHN, AND L. NOODLEMAN, *Density Functional Vertical Self-Consistent Reaction Field Theory for Solvatochromism Studies of Solvent-Sensitive Dyes*, J. Phys. Chem. A, 108 (2004), pp. 3545–3555.

- [22] P. O. LÖWDIN, *Quantum theory of many-particle systems. I. Physical interpretations by means of density matrices, natural spin-orbitals, and convergence problems in the method of configurational interaction*, Phys. Rev., 97 (1955), pp. 1474–1489.
- [23] A. V. MARENICH, S. V. JEROME, C. J. CRAMER, AND D. G. TRUHLAR, *Charge Model 5: An Extension of Hirshfeld Population Analysis for the Accurate Description of Molecular Interactions in Gaseous and Condensed Phases*, (2012).
- [24] K. NISHIMOTO AND N. MATAGA, *Electronic Structure and Spectra of Some Nitrogen Heterocycles*, Zeitshrift fur Phys. Chemie Neue Folge, 12 (1957), pp. 335–338.
- [25] K. OHNO, *Some Remarks on the Pariser-Parr-Pople Method*, Theor. chim. Acta, 2 (1964), pp. 219–227.
- [26] C. C. J. ROOTHAAN, *New Developments in Molecular Orbital Theory*, Rev. Mod. Phys., 23 (1951), p. 69.
- [27] A. SCHÄFER, H. HORN, AND R. AHLRICHS, *Fully optimized contracted Gaussian basis sets for atoms Li to Kr*, J. Chem. Phys, 97 (1992), p. 2571.
- [28] H. STRAIN, M. THOMAS, AND J. KATZ, *Spectral Absorption Properties of Ordinary and Fully Deuteriated Chlorophylls a and b*, Biochem. Biophys. Acta., 75 (1963), pp. 306–311.
- [29] C. STROSS, M. W. VAN DER KAMP, T. A. OLIVER, J. N. HARVEY, N. LINDEN, AND F. R. MANBY, *How static disorder mimics decoherence in anisotropy pump-probe experiments on purple-bacteria light harvesting complexes*, J. Phys. Chem. B, 120 (2016), pp. 11449–11463.
- [30] S. B. WORSTER, O. FEIGHAN, AND F. R. MANBY, *Reliable transition properties from excited-state mean-field calculations*, J. Chem. Phys, 154 (2021), p. 124106.
- [31] L. ZHANG, D.-A. SILVA, Y. YAN, AND X. HUANG, *Force Field Development for Cofactors in the Photosystem II*, J. Comput. Chem., 33 (2012), pp. 1969–1980.
- [32] T. ZIEGLER, A. RANK, AND E. J. BAERENDS, *On the Calculation of Multiplet Energies by the Hartree-Fock-Slater Method*, Acta, 43 (1977), pp. 261–271.

